
Unterschrift Betreuer



TECHNISCHE
UNIVERSITÄT
WIEN
Vienna University of Technology

DIPLOMARBEIT

Pilot Study for 3D/2D Printer Manufactured Foil Sensors for Magnetic Induction Tests

Ausgeführt am Institute of Electrodynamics, Microwave, and
Circuit Engineering
der Technischen Universität Wien

unter der Anleitung von
Univ.Prof. Dr. Helmut Pfützner,
Univ.Prof. Dr. Josef Fidler
und
Dipl.-Ing. Dr. Georgi Shilyashki

durch

Christian Huber

Obere Augartenstraße 46/15
1020 Wien

20. Oktober 2014

Acknowledgements

I would particularly like to thank **Univ.Prof. Dr. Helmut Pfützner** for suggesting the topic of this diploma thesis and for the supervision and assessment of this work.

Thanks also to **Univ.Prof. Dr. Josef Fidler** for the second assessment of this work.

Very special thanks to **Dipl.-Ing. Dr. Georgi Shilyashki** for his daily assistance, discussions and for the numerous corrections of this work.

I would like to thank all the staff of the Institute of Electrodynamics, Microwave, and Circuit Engineering who has assisted me in this work.

Thanks to the **Austrian Science Fund** (FWF) for the financial support as part of the research project P21546-N22 (Saturation Effects of Power Transformer Cores Caused by Geomagnetic Storms) of this work.

Thanks also to the **Austrian Research Promotion Agency** (FFG) for the appropriation of the three-phase model transformer core as part of the research project 834159 (BRIDGE Project 3-D Core Loss).

Last but not least, I would like to thank my family and all my friends for the great support they have given me anytime and anywhere.

Kurzfassung

Um die Eigenschaften von weichmagnetischen Materialien (z. B. in Transformator-kernen oder Generatoren) zu verbessern, werden weltweit intensive Forschungen betrieben. Die Ergebnisse von experimentellen Untersuchungen werden durch die relativen Abmessungen der Messanordnung beeinflusst.

Die vorliegende Arbeit dient als Pilotstudie für ein größeres Projekt, welches die vollautomatische Herstellung von Dünnschichtsensoren ermöglichen soll. Diese Sensoren sollen unterschiedliche physikalische Größen wie: Induktion, Temperatur oder Verformung detektieren. Die Idee hierbei ist, diese Sensoren auf einem dünnen Substratmaterial zu drucken und diese im inneren eines Transformator-kerns zu platzieren. Diese Arbeit beschreibt die Methodik der Sensorproduktion anhand einer Induktionsspule, welche den einfachsten Sensortyp darstellt. Für die Realisierung dieser Arbeit wird ein kombiniertes 3D-/2D-Druckverfahren angewendet.

3D-Druck ist ein schnell wachsender Markt für die Prototypherstellung. Seit dem 3D-Drucker für den Endkunden preislich erschwinglich sind, ergeben sich eine Vielzahl von neuen Anwendungsmöglichkeiten. Der Fokus dieser Arbeit liegt auf der Herstellung von Dünnschichtsensoren für die transversale magnetische Flussdichtemessung in Transformator-kernen. Kommerziell erhältliche Hall-Sensoren zur Flussdichtemessung haben eine Mindestdicke von 500 μm . Mit unserem neuen Herstellungsverfahren sind Sensordicken unter 50 μm möglich. Dieses neue Verfahren bietet neue Möglichkeiten für die Messung von Flussdichten und Streuflüssen in weichmagnetischen Kernen.

Für die Sensorproduktion wurde ein kommerziell erhältlicher 3D-Drucker verwendet. Dieser 3D-Drucker wurde mit einem selbst entwickelten Mikrodosiersystem erweitert. Für die Kontrolle des Systems wurde eigene Hard- und Software entwickelt. Die Mikrodosierung übernimmt ein hochpräziser Linearmotor. Für die leitfähigen Strukturen wurde eine silberhältige Tinte verwendet. Um die für unsere Zwecke am besten geeigneten Materialien zu finden, wurden unterschiedliche Tests durchgeführt. Es wurden auch leitfähige, druckbare Materialien entwickelt und hergestellt.

Für die Messungen wurde ein Sensor mit vier Induktionsspulen mit dem neuen System hergestellt. Die Messungen wurden in einem dreiphasen Modelltransformator - welcher aus kornorientierten Blechen geschichtet ist, ausgeführt. Der produzierte Sensor hat sich in der rauen Testumgebung bewährt und liefert reproduzierbare Ergebnisse.

Nichtsdestotrotz führt eine Sensordicke von 50 μm zu einer Beeinflussung der Messergebnisse. Ein Modell wurde entwickelt um diese Abweichungen über ein approximatives Extrapolationsverfahren zu berechnen.

Abstract

The improvement of the properties of soft magnetic cores (e.g. cores of transformers or generators) is a subject of worldwide research. Experimental analyses are affected by artifacts that result from interior sensors due to their relatively high size, and by extreme expenditure of work as resulting from sensor arrangement.

The current thesis concerns a major project on the development of a new technology for the fully automatic manufacturing of ultra-thin sensors for the interior, inter-laminar detection of different physical parameters like induction, temperature or strain. The basic idea is to print sensor sets on a thin substrate foil that is arranged within the core. The thesis represents a pilot study for the development of a methodology aimed on off-plane induction sensors, as the most simple planned sensor type. For realization, in the course of this thesis, a combined 3D/2D printer procedure was developed.

3D print technology is a fast growing field for single-unit production. Since 3D printers are priced affordable for end-users, a boom on new possibilities is triggered. The focus of this work is to use a low-budget 3D printer to manufacture magnetic thin film sensors for off-plane flux density measurements. Corresponding to commercial transverse Hall sensors show a minimum thickness of about 500 μm . With our new technology, it was possible to manufacture sensors with a thickness under 50 μm . This offers a range of new possibilities for measurements of off-plane and stray fluxes in soft magnetic machine cores.

For this reason, a commercially available 3D printer was purchased and modified with a 2D-printer setup. To control the self-made setup, own hardware, and software were developed. A self-manufactured micro dispensing system which is driven by a linear stepper motor was used. A further main topic of this work was to find a conductive 2D ink that has optimum conductive and printing characteristics. Different commercial materials were tested, and also self-made conductive materials were manufactured. These inks were tested on different substrates to find the best combination for our purpose.

A thin-film sensor with four pick-up sensor coils was manufactured with the new technique, and tested on a three-phase, three-limb model transformer core stacked from grain oriented material. The sensor was tested in most effective ways for measurements of the off-plane induction within the core.

However, even with a sensor thickness of about 50 μm , the corresponding inter-laminar air-gap yield considerable decreases of off-plane flux density. First tests indicate that deviations can be corrected by an approximate extrapolation procedure.

Contents

1. Introduction	1
1.1. Purpose	2
1.2. State of the Art of Thin-Film Sensors	4
1.3. 3D Print Technologies	6
1.4. 2D Print Technologies	8
1.5. Problems of the Combination of 3D/2D Print Technologies	10
2. Conductive Materials	13
2.1. Measurements of Thin-Film Resistance	13
2.2. Carbomorph	15
2.3. Silver Print	17
2.4. Circuit Works	19
2.5. Reactive Silver Ink	20
2.6. DuPont 5028	23
2.7. Comparison	23
3. Experimental Setup	25
3.1. 3D Printer	25
3.2. Modification for 2D Print	27
3.2.1. Hardware	27
3.2.2. Software	31
3.2.3. Calibration	33
3.3. Parameter Study	35
3.4. FEM Simulations	38
3.4.1. CFD Simulation	38
3.4.2. Mechanical Structure Simulation	40
3.5. Improvement Opportunities	42
4. Sensor Manufacturing	43
4.1. Combination of 3D/2D Print	43
4.2. Magnetic Flux Density Sensor	46
4.2.1. Sensor Design	46
4.2.2. Calibration of the Sensor	47
4.2.3. Sensor Version 1	48
4.2.4. Sensor Version 2	50
5. Applications of the Manufactured Sensors	53
5.1. Transformer Core	53

5.2. Results	56
5.2.1. Repeatability of the Sensor Search Coils	56
5.2.2. Comparison of Different Sensors	58
5.2.3. Influence of the Sensor Thickness	59
6. Summary & Outlook	61
A. Appendix	64

Symbols and Abbreviations

Symbols

A	area [m ²]	H	magnetic field intensity [A/m]
A_{arch}	theoretical area of the spiral search coil [m ²]	h	layer thickness [m]
A_{eff}	effective area of the search coil [m ²]	I	current [I]
A_{rect}	theoretical area of the rectangular search coil [m ²]	J	current density [A/m ²]
a	length of the square coil [m]	K_H	hall constant [m ³ /C]
B	magnetic flux density [T]	l	length [m]
B_S	magnetic stray flux density [T]	l_{meas}	length between probes [m]
\hat{B}	nominal magnetization [T]	l_{tot}	total length of a structure [m]
B_z	magnetic flux density in z-direction [T]	m	mass [kg]
d	diameter [m]	N	number of turns []
E	electric field [V/m], E-module [N/m ²]	P_S	specific total loss [W/kg]
F	force [N]	R	resistance [Ω]
F_f	friction force [N]	r	radius [m]
$F_{\Delta p}$	pressure drop force [N]	S	ability of wetting [N/m]
f	frequency [Hz], displacement [m], relative deviation []	s	pitch-width [m]
g	air-gap length [m]	T	temperature [°C], periodic time [s]
		t	time [s]
		t_{offset}	offset time of the microcontroller [s]
		U	electric voltage (RMS-value) [V]
		u	electric voltage (current value) [V]

U_H	hall voltage [V]	Δz	dispensing height [m]
U_{ind}	induced voltage [V]	ϵ	resolution per step [m]
V	dispensing volume [m ³]	κ	proportionality factor for the Archimedean spiral [m]
V_{step}	dispensing volume per step [m ³]		
\dot{V}	volume flow [m ³ /s]	μ	viscosity [Pa·s]
v	velocity [m/s]	μ_r	relative permeability []
w	width [m]	ξ	print efficiency []
γ	step mode []	ρ	density [kg/m ³]
γ_{SG}	surface tension between the solid and gas phase [N/m]	ϱ	resistivity [$\Omega \cdot m$]
γ_{SL}	surface tension between the solid and liquid phase [N/m]	ϱ_m	resistivity depended on mass [$\frac{kg}{m^2} \cdot \Omega$]
γ_{LG}	surface tension between the liquid and gas phase [N/m]	σ_v	von Mises stress [N/m ²]
		Φ	magnetic flux [Wb]
		Φ_S	magnetic stray flux [Wb]
Δp	pressure drop [Pa]	φ_{start}	start angle of the Archimedean spiral [rad]
Δs	step size [m]	φ_{end}	end angle of the Archimedean spiral [rad]
Δx	dispensing length [m]		

Abbreviations

ABS	acrylonitrile-butadiene-styrene	ND	normal direction
CAD	computer-aided design	NO	non-oriented
CCD	charge-coupled device	NTC	negative temperature coefficient
CFD	computational fluid dynamics	PCL	polycaprolactone
CGO	conventional grain-oriented	PET	polyethylene terephthalate
DAQ	data acquisition	PLA	polylactide
DIN	german institute for standardization	RD	rolling direction
FCC	fluid catalytic cracking	SEM	scanning electron microscope
FEM	finite element method	SDM	stick deposition moulding
HGO	highly grain-oriented	STL	stereolithography
IDE	integrated development environment	TD	transverse direction

1. Introduction

The present thesis represents a pilot study for a major project “*Magnetic Foil Sensors for Interior Transformer Core Analyses*” [1] that is planned to start in January 2015. The project is based on an earlier concept [2] for the detection of different physical parameters like local induction or energy losses in laminated soft magnetic machine cores. The basic idea is to arrange the needed extra-thin sensor elements directly on individual laminations that are arranged within the core during its assembling. To keep minimal inter-laminar air gaps, wiring contacts were positioned at “balconies” at the lamination edge, thus remaining outside (Fig.1.1).

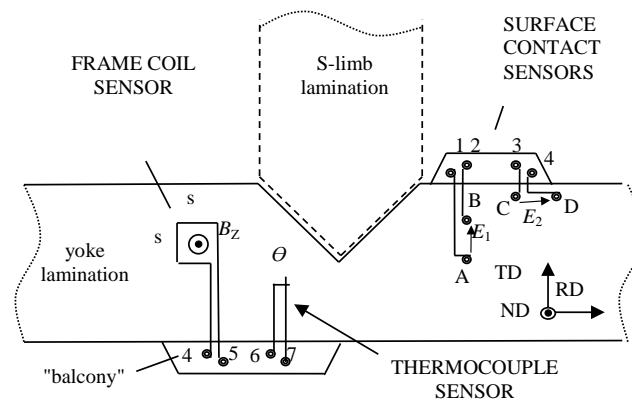


Figure 1.1.: Former concept of thin film sensors for analysis of three-phase transformer cores (from [2]).

The basic idea of the new-planned project [1] is to print the sensor elements on an extra-thin substrate foil that is placed between two core laminations. To restrict the inter-laminar gap, wiring is planned at foil ends remaining outside the core. The foil can also be used for the exact positioning of the sensor set.

The aim of the present thesis is the development of a printer methodology for the most simple planned sensor type that is given by off-plane search coil sensors. The latter should detect flux density components in off-plane direction that tend to arise in the course of three-dimensional, balancing flux density distributions. The thesis also includes the task to check the effectiveness of the manufactured sensors at a three-phase model transformer core.

The idea of the sensor development is the combination of two well-known technologies: 3D printing and printable electronics. The breakthrough of cheap and easy to get 3D printers allows users to print a wide range of mechanical structures with a minimum effort. The potential of polymeric thick-film conductors has already been recognized in the 80s where silver inks were used

mainly in membrane switch applications [3]. In the recent years, new silver inks have been developed and used in novel applications, for example antennas [4], solar cells [5], transistors [6], batteries [7], and chemical sensors [8]. Nevertheless this work is the first attempt to use these technologies to build magnetic thin-film sensors.

This chapter gives a general view of the purpose of thin-film magnetic sensors. The physical concept of magnetic sensors, and the state of the art of these sensors are described. Also the technology of 3D/2D print, and some problems which can appear by combination of these technologies for the manufacturing of thin-film magnetic sensors are discussed.

1.1. Purpose

Worldwide exist several millions transformers, and they are one of the important basic element for the electrical power infrastructure. The efficiency of these transformers reaches through incessantly research and development more than 99.5 %. Nevertheless, if the transformers are not fully utilized, the relative power loss is much higher. Therefore, efforts are still made to increase the power efficiency. Also the audible noise of the transformer cores is a huge field of research [9].

The impact of off-plane flux density on losses, magnetostriction, and therefore on the audible noise of transformer core is described in [10]. The transformer cores are assembled from several package of different width. Further, circular limbs tend to be combined with semi-circular yokes. These characteristics mean that the core represents a complex 3D system. As a consequence, the inhomogeneous distribution of induction in the plane of laminations is linked with balancing off-plane flux density perpendicular to it. The relevance of off-plane flux density can be assumed to increase with increasing nominal induction. The final conclusion of this publication is that the off-plane flux density is an important impact factor for losses and magnetostriction of transformer cores.

To measure the off-plane flux density B_z inside the transformer core, magnetic thin-film sensors are necessary. Several publications exist that describe such sensors (see section 1.2). In [11] the importance of the thickness of these sensors is investigated. In Fig.1.2, the normal flux density of a sputtered coil and a 50 μm wire coil are presented. Coil A is located close to the overlap of two joints. Coil B is in the bridging region. Fig.1.2 (a) shows the B_z of the sputtered coil and Fig.1.2 (b) shows B_z of the 50 μm wire coil. It is obvious that the off-plane flux density B_z with the 50 μm wire coil before the overlap is much smaller than that with the sputtered flat frame coil. This can be explained by the high magnetic resistance of the inter-laminar gap leading to error in measurements. The result of these measurements was the motivation to manufacture a thin-film magnetic sensor. The sensor should be in comparison to the sputtered coils movable, easy to handle, and cheap in manufacturing. Furthermore, the thickness should be as low as possible in order to get well accurate measurements of B_z .

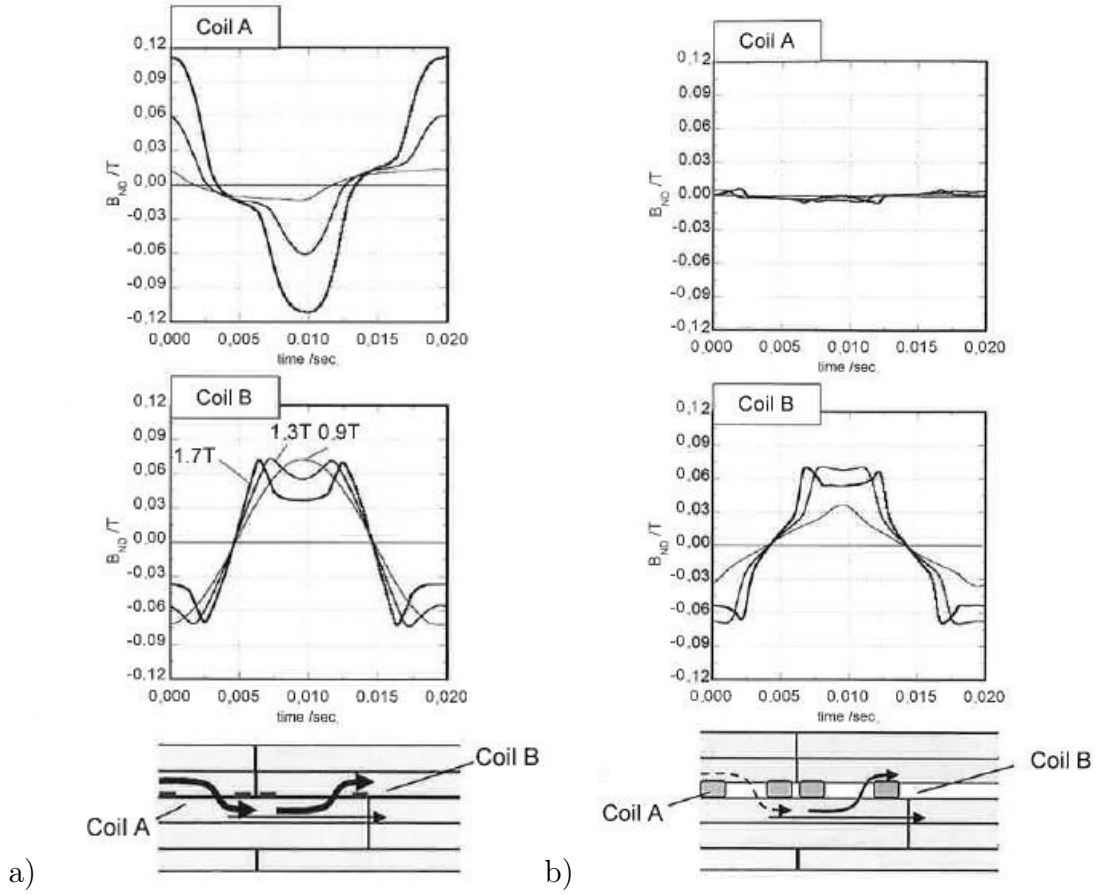


Figure 1.2.: Normal flux density B_z as detected by a flat frame coil and a 50 μm thick wire coil. Coil A is located close to the overlap and coil B is in the bridging region. a) Flat frame coils. b) Frame coils with 50 μm thick wire (from [11]).

1.2. State of the Art of Thin-Film Sensors

This section describes the different kinds of thin-film magnetic sensors for off-plane induction measurements. In general, just two kinds of sensors have become important for measurements in magnetic cores of transformers and rotating machines.

The Hall sensor uses the Hall-effect to measure the magnetic flux density B_z [12]. Fig.1.3 shows the principle of a Hall-sensor. The Lorenz force affects the charge carrier perpendicular to the magnetic field and the current direction. This deflection leads to a charge separation, and this generates also an electrical field E_H . With this effect, it is possible to measure a Hall-voltage U_H which depends only on the thickness h , the magnetic flux density B_z , and a constant K_H depending on the sensor material and temperature, according to

$$U_H = K_H \cdot \frac{IB_z}{h} \quad . \quad (1.1)$$

The Hall sensor is cheap in manufacturing, and immune to other environmental influences. A big disadvantage of this sensor is the minimum thickness. The smallest commercial sensor (e.g. Lakeshore HGT1010) shows a thickness of about $500 \mu\text{m}$. Therefore, the influences of interior measurements in transformer cores are too high for our purpose.

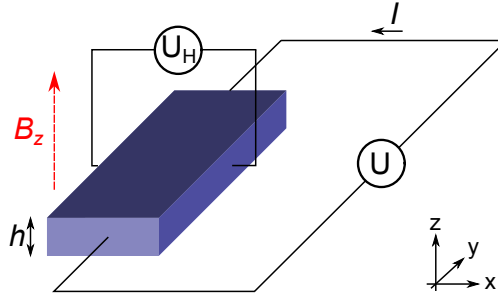


Figure 1.3.: Principle of the Hall sensor.

The second type is the search coil sensor [12]. This is one of the oldest and well-known types of magnetic sensors. Fig.1.4 shows the principle of the search coil. The sensor is based on the fundamental Faraday's law of induction

$$U_{ind} = \frac{d\Phi_z}{dt} = A \cdot \frac{dB_z}{dt} \quad . \quad (1.2)$$

The magnetic flux density B_z through the coil sensor follow as

$$B_z = \frac{1}{A} \cdot \int U_{ind} dt \quad , \quad (1.3)$$

and the magnetic flux Φ_z as

$$\Phi_z = A \cdot B_z \quad , \quad (1.4)$$

assuming homogeneous conditions. A is the enclosed area by the coil sensor. This sensor is easy to build, and the signal depends only on the cross-sectional area A of the sensor. The search coil sensor is practically the only magnetic sensor which can be built by a user. The heeded material is just a conductive winding wire. Therefore, this low-cost, well-accurate sensor is the first choice for a off-plane flux density measurement sensor.

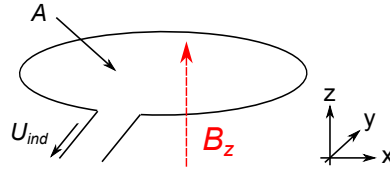


Figure 1.4.: Principle of the search coil.

As described in section 1.1, the thickness of the sensor is the most important variable for accurate measurements of the off-plane flux density B_z in the core interior. There are a couple of scientific publications available which describe thin magnetic coil sensors for measurements of B_z . Three different coil-manufacturing methods are described in the following.

The simplest and oldest one is a thin single-turn, ring-shaped copper frame coil. This sensors has a thickness of $250\text{ }\mu\text{m}$ [10], $150\text{ }\mu\text{m}$ [13], and down to $20\text{ }\mu\text{m}$ [14]. The advantage of this sensor type is that a copper wire is easy accessible and no special building knowledge is necessary. The disadvantage of this type is that with decreasing thickness the handling of the sensor becomes more difficult. Also the effective area A , and therefore, the signal quality of the sensor, is low in comparison with a multi-turn coil.

To decrease the sensor thickness, it is possible to deposit the sensor directly on the laminated transformer sheet. Several methods are well-known to deposit thin films on metallic, or non-metallic surfaces. These include: sputtering, electrodeposition, chemical vapor deposition, and vacuum evaporation. In [15] vacuum evaporation is chosen to deposit search coils onto the surface of grain-oriented silicon-iron laminations. Aluminum with a trace width of 0.5 mm to 1 mm , and a thickness of $0.012\text{ }\mu\text{m}$ to $0.05\text{ }\mu\text{m}$ are deposited on the surface. This paper also describes thermocouple sensors placed on the surface with two different conductive metals. In [16] the sputtering method is chosen. There $1\text{ }\mu\text{m}$ thick copper search coils are sputtered on the surface of the lamination. To prevent problems of galvanic contacts between the search coil and the SiFe material, a $0.25\text{ }\mu\text{m}$ thin dielectric SiO_2 layer is deposited. This is necessary, because when sputtering is employed, a significant rise of the surface temperature is possible that can destroy the coating of the sheet. With these deposition methods the manufacturing of thinnest search coils is possible. The disadvantage of this method is the special and expensive deposition systems. It is only applicable for dimensions of even smallest model transformer cores.

The last and newest method is a manually printed thin-film search coil [2]. There conductive silver ink is painted manually on the surface of the lamination. With this technique, a thickness of the traces of about $10\text{ }\mu\text{m}$ is

reached. This is a cheap and easy-method to make a search coil sensor. The disadvantage is the manual deposition on the surface. The present work should overcome this disadvantage, and therefore, it should be possible to make a best option of a magnetic search coil sensor.

1.3. 3D Print Technologies

It is possible to divide 3D print technologies roughly in three different groups [17]: 1) the sintering or powder printing process, 2) printing with extruded construction materials, and 3) stereolithography, in which the component is manufactured in a vat of liquid ultraviolet curable photopolymer. An ultraviolet laser builds the part by one layer at a time.

The price for a modern 3D printer systems ranges from 1,000 € for a low cost fused deposition modeling printer until 1,000,000 € for a high-tech rapid prototyping system. As described previously, the aim of this work is to manufacture, well accurate magnetic sensors, with a minimum effort, and cost. Therefore, a personal fused deposition modeling printer is the first choice for this work.

The American company Stratasys developed the Fused Deposition Modeling process in the late 1980s. This system creates the object layer by layer by a meltable thermoplastic. The wire-shaped plastic is first heated to just above its softening point. With the aid of an extruder, and a movable, heated nozzle the object is built up in layers on the already solidified material on the building platform. Fig.1.5 shows the most important parts of a personal 3D printer.

As building materials ABS (acrylonitrile-butadiene-styrene) and PLA (polylactide) can be used. As described in section 2.2, also conductive materials are printable. The printed components are generally stable. Nevertheless, they are not as strong as an injection-molded part made of the same material. Visually the construction materials ABS and PLA, of the printed objects, are barely distinguishable. However, PLA has a lower temperature resistance than ABS.

To print an object with a 3D printer is not that simple like printing a document on a commercial office printer. The workflow from a 3D model to a printed object is more difficult. A lot of different settings are available to optimize the printing result. The 3D model is the starting point for a good 3D print result. The model is stored in a STL (STereoLithography) file format. For the print it is necessary to have a model with a single seamless mesh. If the model is good, the model has to be sliced in different layers with a slicer program. This program (e.g. Skeinforce) makes the commandos (G-code) for the printer control. It translates the position of the extruder, the extruder speed, and temperature to get the desired printing result. All these settings are adjustable to fit for the best result. The printer control translates the G-code from the slicing program and, communicates with the electronic of the printer. A micro-controller controls all the stepper motor, extruder motor, temperature, and end-stops of the 3D printer. Fig.1.6 shows the toolchain of a 3D printer.

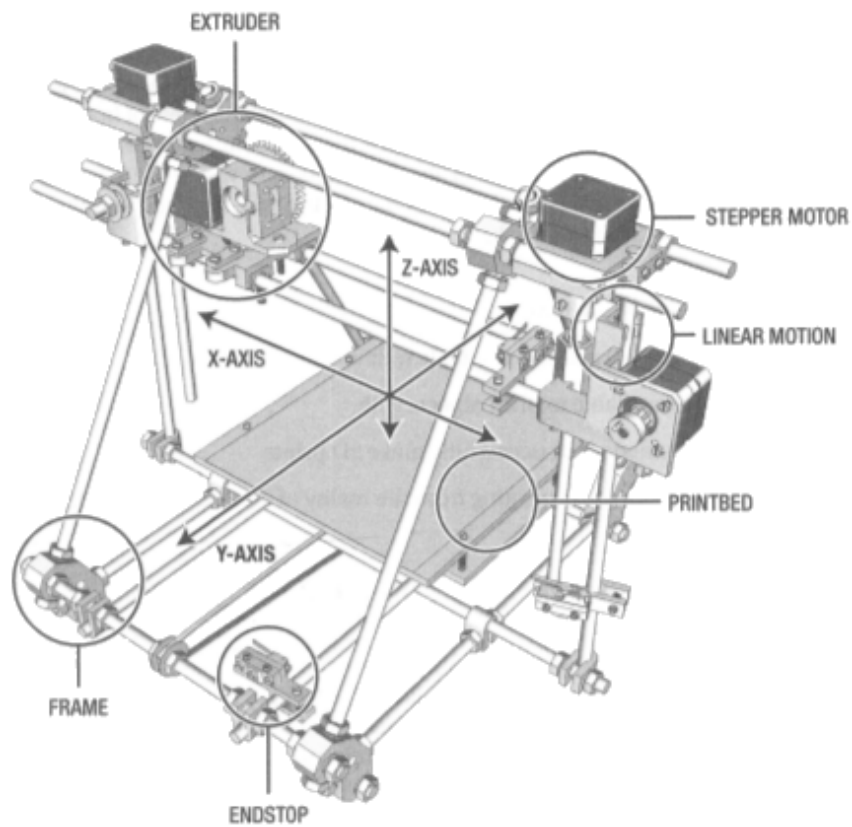


Figure 1.5.: Principe of a modern low-cost personal 3D printer (from [18]).

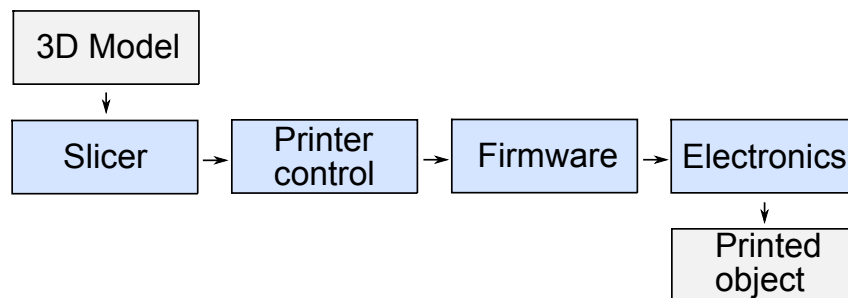


Figure 1.6.: Toolchain of a 3D printer.

1.4. 2D Print Technologies

2D prints or direct-write, micro-dispensing technologies allow the selective deposition and patterning of conductive, or non-conductive materials, e.g. traditional inks for a ink-jet printer work also with one of these systems. The categorization of the non-contact dispensing method based in volume displacement and pressure waves, is plausible in view of the underlying principles of action.

Volume displacement method is based on the jet valve principle. It uses the change in geometry of the storage chamber, generated by a force effect for droplet detachment at the end of the nozzle. The expelled volume from the dispenser is proportional to the generated volume reduction of the ink reservoir. The wave propagation by the pressure-waves based ink-jet method is utilized in the medium. On the other hand, the volume-displacing dispensing process utilizes the reduction of the reservoir volume. If the repulsive forces in the ink exceed a threshold, a drop at the nozzle will detach.

Fig.1.7 shows a typical ink-jet deposition system where a piezocrystal displaces the ink storage chamber to expel the ink droplet. Ink-jet deposition systems can dispense inks with a viscosity up to 0.1 Pa·s, and create feature sizes as small as 25 μm . The thickness of the features is less than 5 μm . The dispensing volume rate through the nozzle is only 0.3 mm³/s [19].

The group of contact dispensing methods uses to provide a certain amount of ink, either by the time-pressure, or the piston-dosing principle. The time-pressure dosing principle, is characterized by the fact that after turn on a pneumatic valve, a pressure pulse of defined duration time and height acts on the ink cartridge, and determines the flow rate through the nozzle. Piston dispensing methods use the motion of an electrically driven piston for the dosage. The distance covered in the direction of the piston path and the geometric conditions of the reservoir determine the metered volume. This makes the method almost independent from the ink rheology, and therefore, it is classified as a volumetrically method. Fig.1.8 shows the schematic principle of piston dispensing systems.

With this system, inks or pastes with viscosities up to 5000 Pa·s are possible to be printed. The feature width is lower than 1 mm with a thickness under 50 μm . The speed of the nozzle can reach up to 300 mm/s [19]. The volume flow depends on the piston pressure and the nozzle diameter. As shown in section 3.4, also the distance between the substrate and the nozzle has an important impact on the volume flow.

technology	resolution	thickness	write speed	viscosity
ink-Jet	> 10 μm	> 1 μm	< 0.3 mm ³ /s	< 0.1 Pa·s
pressure-dispensing	> 25 μm	> 10 μm	< 300 mm/s	< 5000 Pa·s

Table 1.1.: Comparison of 2D dispensing techniques (from [19]).

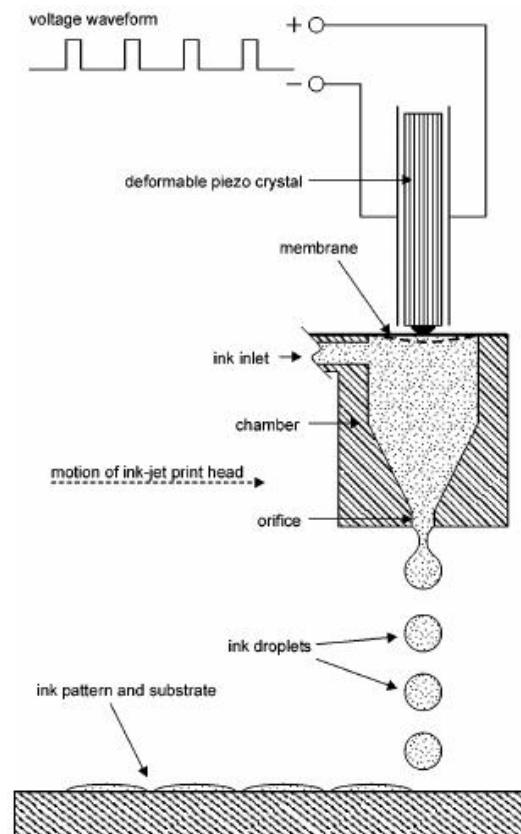


Figure 1.7.: Diagram of the piezo drop-on-demand ink-jet printing system. In the print head, a piezocrystal expands in response to an electrical driving signal, deforming a membrane, causing a pressure impulse within the ink chamber, expelling a single droplet from the orifice. The chamber is refilled through the inlet by capillary action at the orifice. Multiple droplets deposited onto the substrate leave the printed pattern (from [20]).

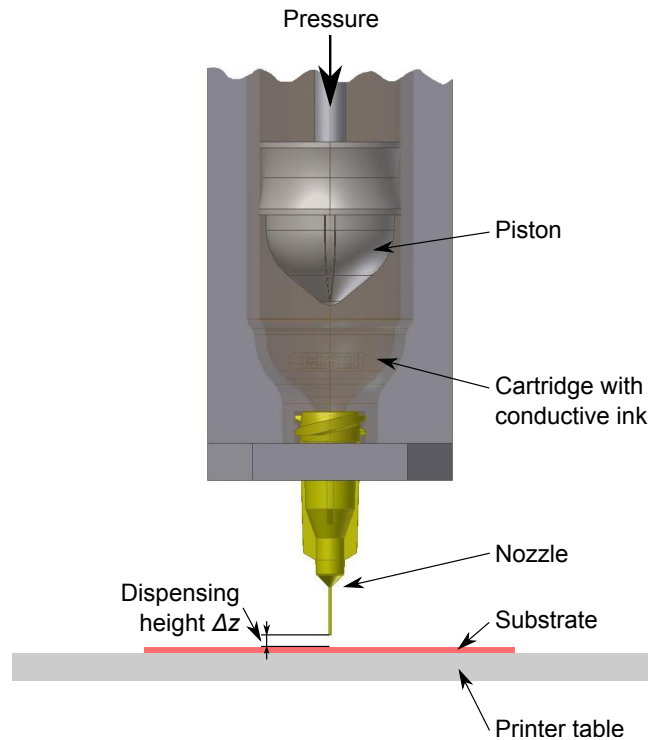


Figure 1.8.: Schematic of a piston dispensing system.

Tab.1.1 shows a comparison between these two different technologies. It shows that the ink-jet system has a higher resolution and a lower feature thickness. The writing speed can be increased by using an array of nozzles. A big disadvantage of this system is that a low viscosity of the ink is necessary. For normal home office printing, this is not a problem, but for conductive inks the viscosity of the ink is proportional to the conductive particle loading. Higher concentrations imply higher conductivities. Also conductive pastes with a high viscosity are easier to handle and cheaper. For this reason a pressure dispensing system is chosen for this work.

1.5. Problems of the Combination of 3D/2D Print Technologies

At first, it seems easy to combine these two technologies, but in detail it is a non-trivial challenge. In this section some of these challenges are discussed.

For the combination it is necessary to mount a pressure or ink-jet dispensing system on the extruder of the 3D printer. If the 3D printer is an open-source system, it is possible to rewrite the firmware to control the 2D printer setup. With this self-written software, the substrate can be printed by the 3D printer setup, and afterwards the conductive traces can be printed by the 2D printer setup. With this method an arbitrary designed 3D printed object with conductive traces, as search coils for magnetic measurements tasks, for example, can be created.

Subsequently, some well-known problems of the combination of these two systems are listened. As described in chapter 2, it is necessary to cure the conductive silver inks to reach the maximum of conductivity. The curing temperature (more than 100 °C), is higher than the temperature resistance of ABS plastic (~ 80 °C [21]). Therefore, new 3D printing materials have been found to withstand this curing temperatures. Some of these materials include Duraform HST, Prototherm, or ULTERM. To use the standard building materials, like ABS for the 3D printer, other curing techniques are available [22]. They are based on the idea that conductive silver inks can be sintered using laser or microwave radiation. Laser based sintering still poses the risk of damaging the polymer substrate. Another method is the curing with pulsed photonic radiation. This method shows good polymer compatibility. The disadvantage for these alternative curing techniques is that the layer thickness is limited to 3 μm . Therefore, it is only applicable for ink-jet printed conductive lines.

Another important aspect of printed 2D structures on a 3D printed object is the adhesion of the materials. Poor adhesion between the materials results in peeling off of the conductive layer, and therefore, to an failure of the sensor. There are some factors which influence the adhesion between the two materials:

- the roughness of the substrate (3D printed) object,
- surface treatment of the substrate,
- surface energy of the substrate and the conductive ink.

The layer by layer deposition in a 3D printer results in a very nonuniform surface on the macro scale corresponding to a high roughness. In chapter 2, we observe some microscope images that show the roughness of the surface caused by the layers. This roughness caused a wicking of the conductive ink in the grooves of the surface. It is also obvious that inks or pastes, with a low viscosity tend more to wicking, as those with a high viscosity. To prevent this problem, in [23] a dielectric layer between the substrate and the conductive ink is deposited. This dielectric material fills the voids, and it leads a planar surface behind. On this surface the conductive silver ink can be deposit without any difficulties. In [24] the problem was solved by mill channels into the substrate where the silver ink will be dispensed. For this solution, a high substrate thickness is necessary, and therefore, it is not possible for our purpose.

The surface energy of the substrate and the conductive ink determine the contact angle between the materials. To guarantee a good adhesion of the conductive ink, the surface energy of the substrate must be higher as the surface energy of the ink. With surface treatment such as etching, plasma treatment, or UV/ozone treatment the surface energy of the substrate raises. In section 2.5, a plasma treatment will be used to make a substrate printable.

Another critical problem of the combination of 3D and 2D print is the minimum thickness of a single printed layer. Good personal 3D printers show a resolution in the z-axis of about 3 μm [25]. However, this is just a theoretical value. Our measurements show a much higher thickness of a layer of about

100 μm . This is not acceptable for a thin film magnetic sensor. Also the mechanical properties of the printed layers, such as bending, are insufficient. It is fragile and breaks on the conjunction of two fused lines. For this reason, other substrate materials are investigated.

At first, a simple PET (polyethylene terephthalate) foil with a thickness about 150 μm is tested. The surface conditions of the substrate are good, but the thickness of the material is too high, and also the temperature resistance is not good enough for our purpose. Next a polyamide film (Kapton, DuPont) with a thickness of 25 μm is tested. This foil has a high temperature resistance from about 400 $^{\circ}\text{C}$, and it shows also excellent mechanical properties. For that reason, we decided to use this foil as a substrate for the sensor.

2. Conductive Materials

This chapter describes the different conductive materials used for this work. First, the characterization of conductors for printed electronics is described. Some special arrangements are necessary to measure the resistivity of a thin-film structure. Also a self-made conductive polymer for the 3D printer is presented. Different commercial and self-made silver conductive inks for the 2D print setup are described, and tested to find the best ink for our purpose. Only silver based inks are tested, because this type shows the best conductivity. Other kinds of conductive inks contain gold, copper, carbon nanotubes, graphene oxide, or conductive polymers [26].

The price for 100 ml of these conductive silver inks range from 100 €, for a colloidal suspension with powder or flakes in the size of 1 μm to 50 μm , or a self-made reactive silver ink, up to 1.000 € for high-tech nanoparticle suspensions with good dispensing conditions.

2.1. Measurements of Thin-Film Resistance

For the characterization of thin-film conductors some special properties have been considered. The resistance R of a thin-film trace depends on the material, length, width, and thickness of the line. Therefore, the resistance R is an extensive variable. In contrast to the resistivity, ϱ which is an intensive parameter, independent from size or shape of the printed conductive trace. The resistivity ϱ with the dimension $\Omega\cdot\text{m}$ is defined as

$$\varrho = \frac{A}{l} \cdot R \quad , \quad (2.1)$$

where A is the cross-sectional area and l is the length of the measured trace. The resistivity for bulk silver is $\varrho=1.59 \mu\Omega\cdot\text{cm}$. Silver is the best native available conductor (graphene is with a resistivity of $\varrho=1.00 \mu\Omega\cdot\text{cm}$ even a better one) [27].

Another common way to express the resistivity in thin-film applications is by

$$\varrho_m = \frac{m}{l_{meas} \cdot l_{tot}} \cdot R \quad . \quad (2.2)$$

Here, m is the mass of the structure (i.e. the conductor being measured, minus any substrate), l_{meas} is the length between the probes, and l_{tot} is the total length of the structure.

These two formulas are related by the density ρ of the conductive material according to

$$\varrho_m = \rho \cdot \varrho \quad . \quad (2.3)$$

The following describes, why it can be more accurate to measure the resistivity over the mass m of the structure, than the cross-sectional area A . A dimensionless variable ξ for the print efficiency is introduced

$$\xi = \frac{\varrho_{min}}{\varrho_{meas}} \quad . \quad (2.4)$$

It is the ratio of the resistivity performance of the printed ink, and the theoretical resistivity of the ink in a perfectly prepared sample. Fig.2.1 shows the principle of the print efficiency ξ .

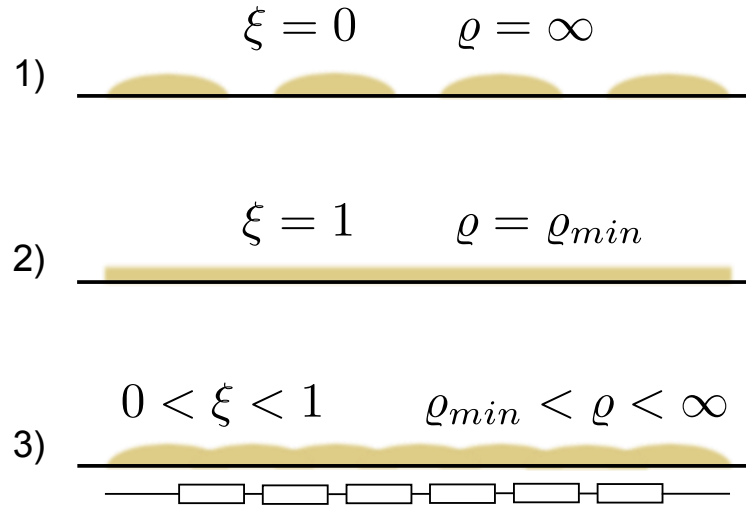


Figure 2.1.: Principle of the print efficiency.

In case 1, the print efficiency is $\xi = 0$. Conductive ink is deposited on the substrate, but no conductivity can be measured because the ink is deposited only in drops and no bridges between these drops are available. Case 2, shows the perfect smooth, and flat conductive film on the substrate with a print efficiency $\xi = 1$. Case 3, describes a real deposition. During the printing process thicker and thinner areas are left. They can be modeled as resistors in series. These resistors affect the measured resistance ϱ of the sample.

With a theoretical area A , the print efficiency ξ can be also measured. For this work measurements for the volume-resistivity ϱ , and the mass-resistivity ϱ_m are made. The density ρ of the conductive ink can be found in the data-sheets of the manufacturer. The mass m of the structure can be measured accurately with a high precision balance (A200S, Sartorius, readability: 0.0001 g). To measure the cross-sectional area A a reflected-light microscope (Zeiss-Axioplan, 6.25x magnification) is used.

R is measured with a self-made four-point probe. The advantage of the four-point probe is the separation of voltage and current detection that eliminates

the resistance of the wiring and the contact resistances. Fig.2.2 shows the four-point probe measurement with a multimeter (HP34401A, Hewlett-Packard).

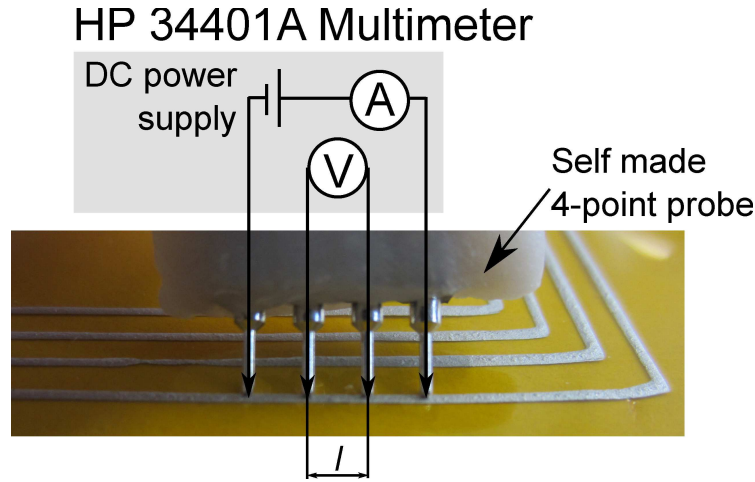


Figure 2.2.: Four-point probe measurement on a printed silver trace.

A probe for thin-film measurements was manufactured by ourself. With this probe, the measurement length l is defined as 2.54 mm.

2.2. Carbomorph

In [28] a low-cost conductive composite material for 3D printing of electronic sensors is presented. In this section the capability of this material is investigated. For that reason, the conductive composite material (carbomorph) is made by ourself, and the properties of the material are studied.

Carbomorph is a composite material, it is composed of a printable thermoplastic matrix of PCL (polycaprolactone), and a conductive form of carbon black. PCL is a biodegradable polyester with a low melting point of around 60 °C. This low melting point offers advantages for the manufacturing process of carbomorph, and for the deposition with a 3D printer. The conductive carbon black (Black Pearls 2000, Cabot) is an amorphous form of carbon, produced from incomplete combustion of heavy petroleum products such as FCC (fluid catalytic cracking). A transition from insulating to non-insulation behavior for composites with a conductive filler, is generally observed when the volume concentration of filler reaches a threshold of about 25 % [29].

To manufacture about 3 g of carbomorph filaments, we process following formulation:

1. Add 3 g of PCL thermoplastic to a stirred suspension of Black Pearls 2000 in 40 ml dichloromethane. Dichloromethane acts as a solvent for the PCL. The weight of Black Pearls 2000 is a function of the desired ratio between the thermoplastic matrix and the conductive filler.

2. Stir the suspension for one hour.
3. After stirring the suspension is poured onto a watch glass to allow evaporation of the dichloromethane under a fume hood for one hour.
4. The resultant composite material is placed in a water bath at 80 °C for one minute.
5. Remove the melting material and roll it under two glass plates to form a 3 mm wide filament of carbomorph.

Fig.2.3 shows the components of carbomorph. Also a 125x magnification of the Black Pearls 2000 is pictured. This picture is made with a Zeiss-Axioplan reflected-light microscope. The carbon black nanoparticles are detectable under this magnification. For a better resolution of the nanoparticles a SEM (scanning electron microscope) would be necessary. However, the aim of this work is to manufacture thin-film magnetic sensors and the inner structure of the materials is not that important.

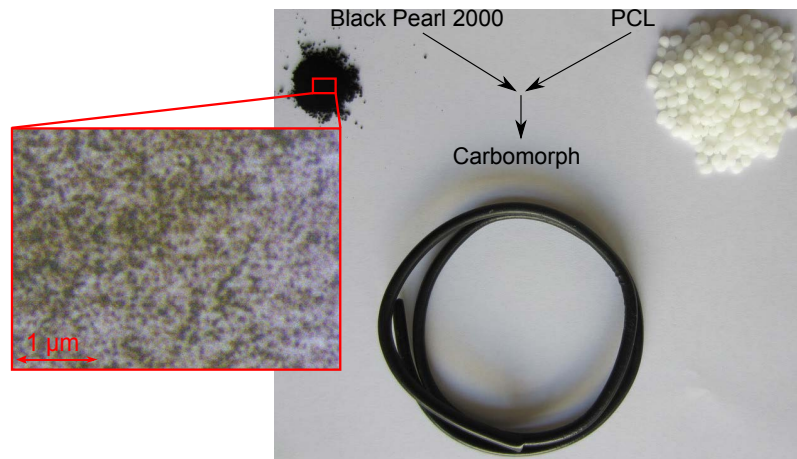


Figure 2.3.: Components of carbomorph. 125x magnification of the conductive carbon black makes the nanoparticles visible.

With this method, carbomorph with different ratios between the thermoplastic matrix and the conductive filler is manufactured. In this case the resistivity ϱ is measured of the round $d=3$ mm wide filaments instead of a thin-film layer. To calculate the resistivity ϱ , Eq.2.1 with a cross-sectional area $A = d^2 \cdot \pi/4$ is used. The resistance R of the material is measured with a multimeter (HP34401A, Hewlett-Packard). For the elimination of contact resistivity the four-point measurement was used. Fig.2.4 shows the measurements of the resistivity ϱ at different wt% of Black Pearls 2000.

It is obvious that the contact resistance of the material decreases with the load of carbon black. Also the resistivity of the material decreases, but not in the same order as the contact resistivity. At carbon black load of 30 wt% the contact resistance disappears, but at this ratio the filaments are really frangible, and not printable with a 3D printer. Nevertheless, ϱ is too high to

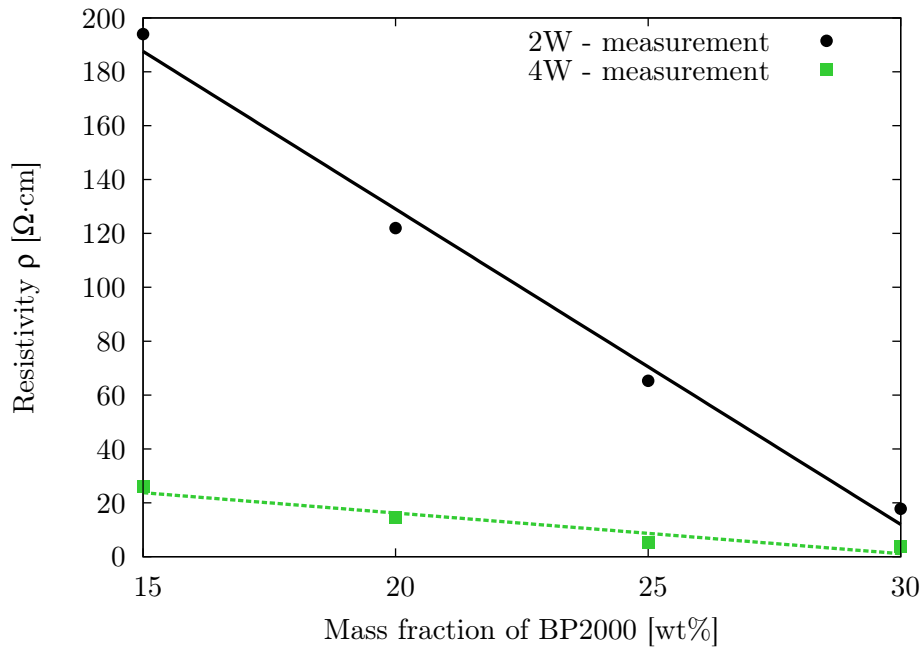


Figure 2.4.: Resistivity measurements with carbomorph at different wt% of Black Pearls 2000.

manufacture well-accurate magnetic sensors. Another problem is the design of the filaments, as described in section 3.1. Our 3D printer needs special notched filaments which cannot be produced in our laboratory.

This was the first attempt to manufacture conductive plastic. With a 3D printer which uses round filaments, it would be possible to print conductive 3D objects. This could be an interesting topic for a future work.

2.3. Silver Print

In this section, the first conductive silver based ink is presented. This ink is one of the cheapest available silver inks. It is manufactured by MG-Chemicals as Silver Print 842. The viscosity of the ink is about $\mu=8$ Pa·s, and it has a theoretical resistivity $\varrho = 5.08 \cdot 10^{-5}$, $\Omega\cdot\text{cm}$ and a density of $\rho=2.15$ g/ml. This is the only tested ink that reaches the maximum conductivity without curring. The silver content of the ink is 40 wt% to 70 wt%, and as solvent serves toluene. In Fig.2.5, it is visible that the silver is formed as flakes, and it has a typical size of about $1\text{ }\mu\text{m}$ to $20\text{ }\mu\text{m}$. A problem of all these suspensions is that they tend to form clusters. This leads to clogging inside the nozzle. Another upcoming disadvantage of this ink is that it dries out very fast. This clogs the nozzle during the printing process.

In this section, the resistivity ϱ is measured using two different methods. At first, the measurement are performed with the self-made four-point probe (Fig.2.2). The other method is to measure the resistivity ϱ over the mass m of the structure, as described in section 2.1.

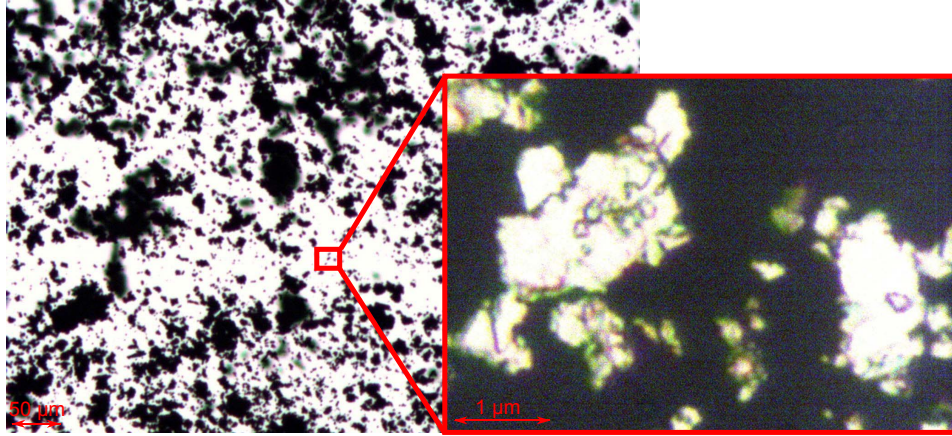


Figure 2.5.: Microscope image of the conductive silver ink Silver Print. Left 6.25x magnification, right 125x magnification

A test pattern from section 3.3 is investigated for this purpose. The test pattern and a cross-sectional microscope image are pictured in Fig.2.6. As substrate a PET foil is used.

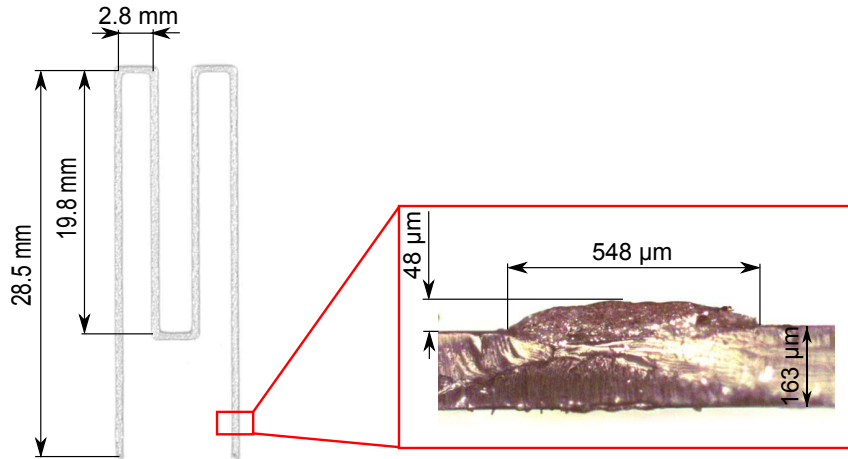


Figure 2.6.: Test pattern to calculate the resistivity ρ of the conductive silver ink. Microscope image of the cross-sectional area A with 6.25x magnification.

The mass of the test pattern is measured, it is $m=0.0121$ g. The total length of the trace is $l_{tot}=105$ mm. To calculate a print efficiency ξ , a theoretical cross-sectional area A have to be defined. This theoretical cross-sectional area A is calculated from the microscope image (see Fig.2.2). The cross-sectional area A has the shape of a circular segment, but it can be approximated by a rectangle with $2/3$ of the total height. The failure for this approximation is less than 0.2 %. Than one has: $A = 2/3 \cdot w \cdot h$, where w is the width and h is the height of the trace. The resistance of the printed trace with the four-point probe is $R=0.70 \Omega$. In Tab.2.1 the results of the measurements are summarized.

	fixed area A	fixed weight m	theoretical
resistivity ϱ [$\Omega\cdot\text{cm}$]	$5.50\cdot 10^{-4}$	$5.30\cdot 10^{-4}$	$5.08\cdot 10^{-4}$

Table 2.1.: Comparison of the different measurements methods of resistivity ϱ .

Using these values, a the print efficiency can be calculated to $\xi=1.03$. It means, that the cross-sectional area A is in some regions bigger than the measured area. However, both results are well-accurate. For the further resistivity measurements only the simpler measurement with the fixed cross-sectional area A is used.

The printing result with this ink is good, and it shows good adhesive properties on the PET substrate. However, on the Kapton substrate the printed traces peel away really quick. Also the solvent evaporation is too fast. Therefore, the nozzle clogs during the printing process.

2.4. Circuit Works

The next ink is CW2200 from Chemtronics. This ink is used for a conductive pen. With this pen, silver traces can be printed manually. It is the same ink as described in [2]. The ink is based on a silver flakes filled polymer with a silver amount of about 35 wt% to 65 wt%. The silver flakes have the same size and shape as pictured in Fig.2.5. As a solvent different kinds of acetate solutions are used. No viscosity value is available for this ink, but according to our tests, it is in the same range as the Silver Print ink. The density is $\rho=1.8\text{ g/ml}$, and therefore, lower as the density of Silver Print. The theoretical resistivity is $\varrho=5.0\cdot 10^{-5}\ \Omega\cdot\text{cm}$, and is one decimal power better than the Silver Print ink. For the maximum conductivity a curing temperature of $T=120^\circ\text{C}$ to $T=150^\circ\text{C}$ is necessary. Fig.2.7 shows the resistivity ϱ of the ink as a function of the curing temperature T . The temperature was controlled in a laboratory oven (Heraeus). The fit of the measured resistivity shows an exponential decay.

This ink shows good conductive, printable, and adhesion properties. For that reason, this ink is the preferred ink for the magnetic sensor manufacturing.

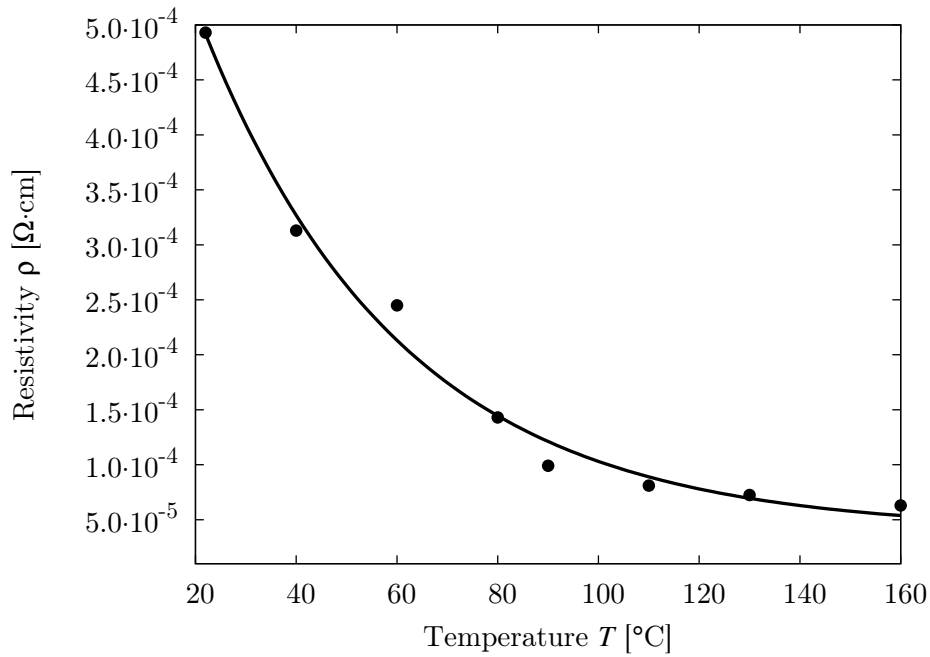


Figure 2.7.: Resistivity ρ of the Circuit Work CW2200 ink as a function of the curing temperature T .

2.5. Reactive Silver Ink

A new way to manufacture a highly conductive silver ink is presented in [30]. The production method is based on a modified Tollens' process. First, silver acetate is dissolved in aqueous ammonium hydroxide. Formic acid is then titrated into the solution, which is mixed thoroughly. Fig.2.8 shows the key constituents presented in the initial solution (left), the reactive silver ink (middle), and the printed silver features (right).

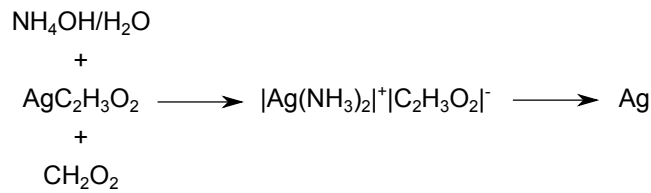


Figure 2.8.: Key constituents in the initial solution, ink, and printed features (from [30]).

For the manufacturing of about 3 ml of reactive silver ink, following formulation is used:

1. Vortex mixing of 1 g silver acetate ($\text{AgC}_2\text{H}_3\text{O}_2$, 99 %) into 2.5 ml aqueous ammonium hydroxide (NH_4OH , 28-30 %) at room temperature for 15 s.
2. 0.2 ml of formic acid (CH_2O_2 , ≥ 88 %) is titrated into the solution drop-wise for 60 s - vortex mixing after each drop.

3. The solution changes the color from light orange to grayish black. It is an indication for rapid reduction of silver ions to large silver particle.
4. The solution remains undisturbed for 12 h to allow the large particles to settle out.
5. Filtered the solution through a 200 nm syringe filter.

The resulting suspension is a stable particle-free ink. The clear solution contains 22 wt% of silver. After curing at about $T=90\text{ }^{\circ}\text{C}$ elemental silver is the only phase that remains due the rapid evaporation of ammonia, and low boiling points reactants. The resistivity after curing is equivalent to that of bulk silver. The viscosity is rather low $\mu=0.2\text{ Pa}\cdot\text{s}$, but 2,3-butanediol (10 % by volume) can be served as a humectant and viscosifying aid. Fig.2.9 shows the resistivity ρ of the reactive silver ink as a function of the curing temperature T . Differently than claimed in the publication, the resistivity ρ at room temperature is very high, but decreases exponentially down to a curing temperature from about $T=90\text{ }^{\circ}\text{C}$.

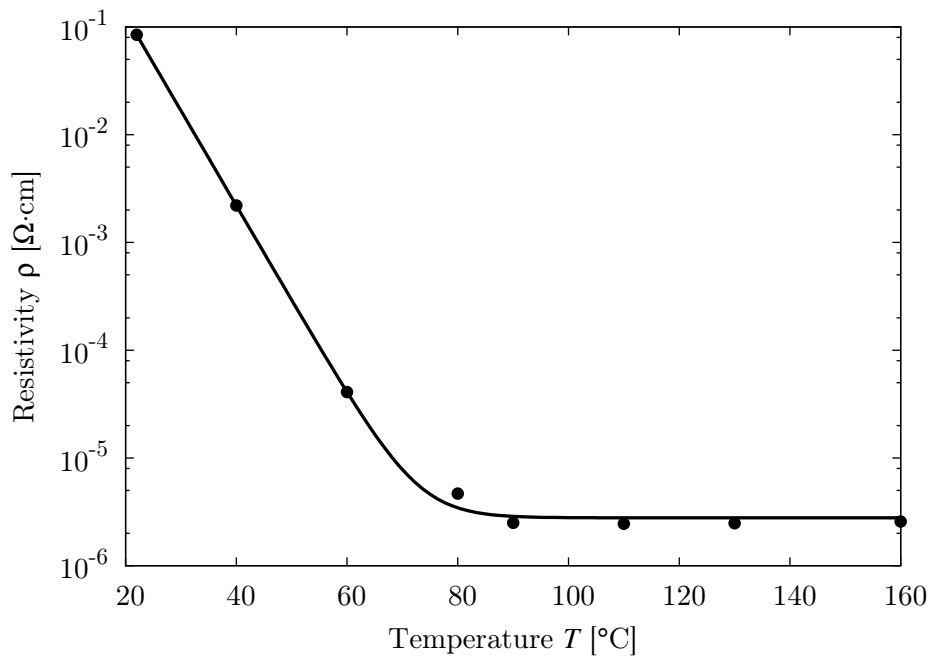


Figure 2.9.: Resistivity ρ of the self-made reactive silver ink as a function of the curing temperature T .

The measured resistivity ρ after the low temperature curing process is really good. Since it is a particle free ink no clogging of the nozzle can occur. Also the cheap price for the ingredients is a big advantage from this ink. However, the ink has one big disadvantage. The surface tension of the ink is extremely high. This prevents a good printing result, because the surface tension of the ink should be smaller than that of the substrate material. In the following subsection the opportunity of surface treatment, for increasing the surface tension, of the substrate material is discussed.

Surface Treatment

Several technologies are well-known for improving the adhesion capabilities of inks on metallic or non-metallic substrates. The ability of wetting depends on the surface tension γ of the fluid and the substrate. The spreading parameter S defines the ability of wetting. It is defined as

$$S = \gamma_{SG} - (\gamma_{SL} + \gamma_{LG}) \quad , \quad (2.5)$$

where γ_{SG} is the surface tension between the solid and gas phase, γ_{SL} between the solid and liquid phase, and γ_{LG} between liquid and gas phase. When $S > 0$, the liquid wets the surface completely. When $S < 0$, there is partial wetting. To obtain $S > 0$, it is possible to increase the surface tension of the substrate, or decrease the surface tension of the ink.

The first try to decrease the surface tension of the ink was with a nonionic surfactant like polysorbate. However, the surfactant destroyed the reactive silver ink and it was useless. Furthermore, several publications are available which describe the surface treatment by plasma [31] or UV/ozone [32], in order to increase the surface tension γ_{SG} .

The plasma treatment can remove the hydrogen contamination on the substrate surface. Since hydrocarbons have a low surface energy, the removal of these contamination leads to an increase of the surface tension γ_{SG} . During the process, also oxide is formed on the surface of the substrate. This makes the surface more hydrophilic, and therefore, the surface tension γ_{SG} increases.

At the institute for Solid State Electronics at the TU-Vienna, a plasma cleaning device (100E, Plasma System) is available. The Kapton substrate was treated with different resisting times. The plasma system is filled with O_2 -gas and partially evacuated at a pressure of 0.7 Torr. The system has a power of 300 W. Fig.2.10 shows the impact of the ability of wetting on the Kapton substrate. A resisting time of 5 min is enough to make the reactive silver ink printable. An interesting observation is that the effect is gone after curing temperatures above $T=90^\circ\text{C}$.

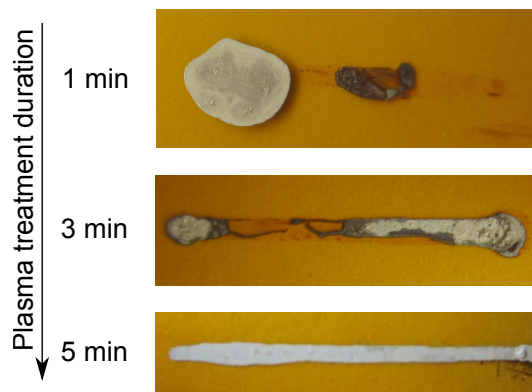


Figure 2.10.: Property of the Kapton foil under plasma treatment at different resisting times.

2.6. DuPont 5028

The last investigated conductive silver ink is a test sample from DuPont (Product name: 5028). This ink contains nanoparticles of silver. The concentration is about 60 wt% to 70 wt%. As solvent serves propanol. Under the microscope no flakes are visible. The theoretical resistivity is $\rho=3.0 \cdot 10^{-5} \Omega \cdot \text{cm}$. The viscosity is about $\mu=15 \text{ Pa} \cdot \text{s}$ to $\mu=30 \text{ Pa} \cdot \text{s}$, and it has a density of $\rho=2.64 \text{ g/ml}$. As typical cure temperature $T=120^\circ\text{C}$ to $T=160^\circ\text{C}$ are listed. Fig.2.11 shows the resistivity ρ of the ink as a function of the curing temperature T . The resistivity ρ indicates an exponential decay.

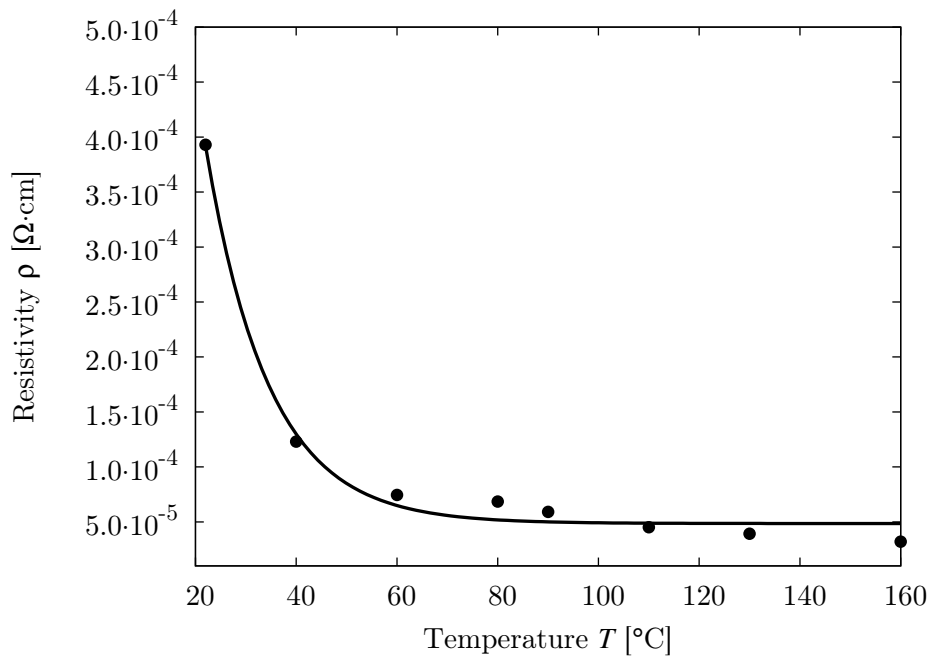


Figure 2.11.: Resistivity ρ of the DuPont 5028 ink as a function of the curing temperature T .

The ink has very good printing and resistivity properties. A disadvantage of the ink is the high price and it is not easily available.

2.7. Comparison

For this work five different conductive materials were tested. A self-made conductive thermoplastic with a high resistivity was manufactured. Also a reactive silver ink with a low resistivity was made. These two self-made solutions have some disadvantages. The silver inks showed similar curing conditions with the exception of Silver Print from MG Chemicals, where no curing was necessary, but the resistance was higher than of that other inks. The self-made reactive silver ink has a big potential, if the problem of the high surface tension can be solved in the future. The plasma treatment is too costly, since it should be done before each print. DuPont 5028 silver ink showed the best printing

results, but it is not easy available, and also the price is too high. In Fig.2.12 a comparison between the resistance ρ of the tested inks is shown.

The best balance between resistivity, price, availability, and printing result shows the ink CW2200 from Circuit Work. For that reason, this is the choice for all other experiments, and it is performed in the current work.

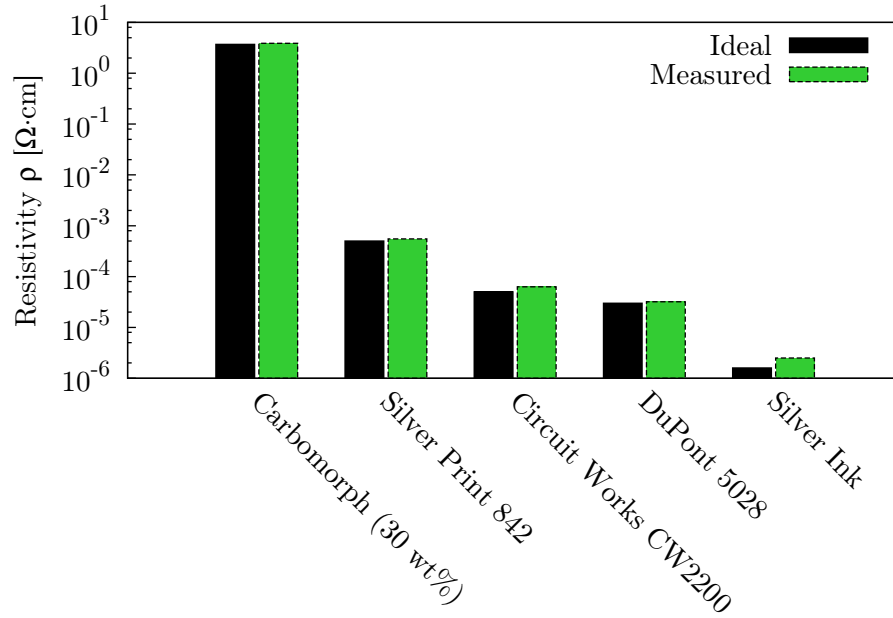


Figure 2.12.: Comparison of the resistivity ρ of all tested conductive materials.

3. Experimental Setup

This chapter describes the setup which is used for the sensor manufacture. A piston dispensing system for printing silver ink is combined with a modern low cost 3D printer (FabbsterG, Sintermask). For the new purpose of the 3D printer, new hardware and software have been developed. Also a calibration of the new printing parameters is performed. With parameter studies the best printing result are found. To detect error sources of the dispensing system and the 3D printer, FEM (finite element method) simulations were performed. For a new generation of combined 3D/2D printer improvement opportunities are listened to enhance the printing result in the future.

3.1. 3D Printer

FabbsterG from Sintermask is a 3D printer for home use [25]. The dimensions of the device are 590 mm width 470 mm long and 540 mm high. It builds objects up to a size of 225 x 225 x 210 mm. It processes ABS and PLA plastic. The extruder temperature ranges from 25 °C to 290 °C and it heats up to 290 °C, in just 30 s. The layer thickness is 88 µm in the default mode, but it can be refined down to 44 µm. The accuracy of the structures is 0.1 mm, or 0.4 % of the nominal size. The printing speed is up to 400 mm/s. With the standard nozzle ($d=0.4$ mm, stainless steel), a minimum wall thickness of about 0.7 mm is possible. To move the extruder four Nema 17 stepper motors are fitted. A planetary transmission arranges a better accuracy of the positioning. The repeatability of an extruder position in the printing chamber is <20 µm for the X/Y-axis, and <14 µm for the Z-axis. The print head itself moves sideways and upwards. For the third axis, the work platform is slidable, which moves forwards and backwards. A heated printer platform can be retrofitted. The heated plate ensures that the workpiece cools slowly. This should prevent the printed object from warping or cracking during the cooling process.

The printer uses a proprietary extrusion mechanism, called SDM (stick deposition moulding). Instead of a drum from which the round filaments is unwound, the FabbsterG has a magazine, in which the almost 25 cm long Like-sticks are inserted. The sticks are serrated on two sides. In the extruder, there are two gears that push the stick forward. The advantage of this system is a precise dosage of the melt. This allows us to print objects with optimal material properties. It is also possible to print objects with different colors. The disadvantages of the system is the higher price of the filaments, and it is not possible to use the self-made conductive material, as described in section 2.2. In Fig.3.1, the printer and the material deposition mechanism are shown in detail. The software, which prepares a 3D model for the printer, is devel-

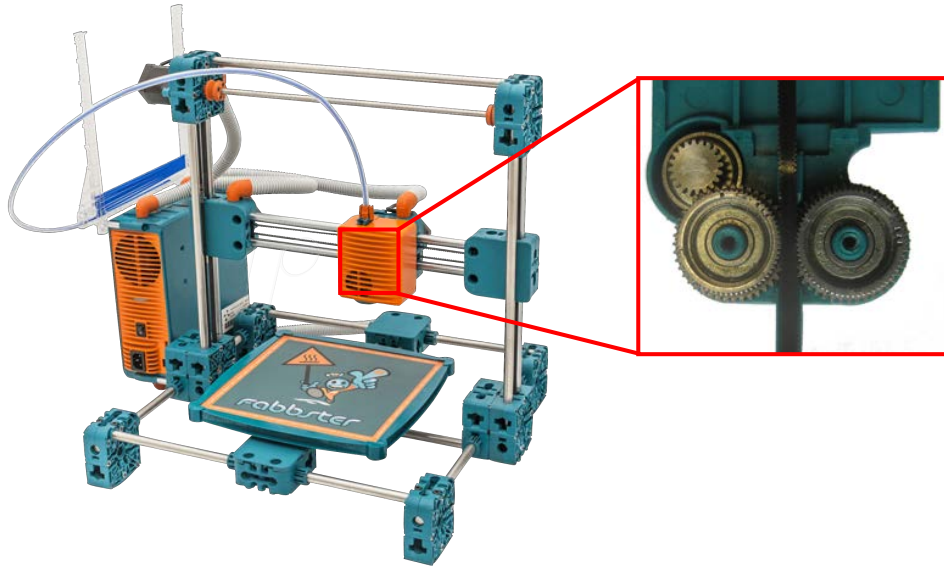


Figure 3.1.: FabbsterG 3D printer. The detail shows the material deposition mechanism for the proprietary filaments (from [25]).

oped from Netfabb. The STL print file can be transferred to the FabbsterG via USB-cable or stored on a SD-card.

Fig.3.2 shows an example of the printed object which was manufactured with the FabbsterG. For the print with ABS, the standard printing parameters are used. The result has a rough surface with a layer thickness of about $90\text{ }\mu\text{m}$. It was the first test with the 3D printer, and it led to a better understanding of all the printing parameters and how the 3D printer works in general.

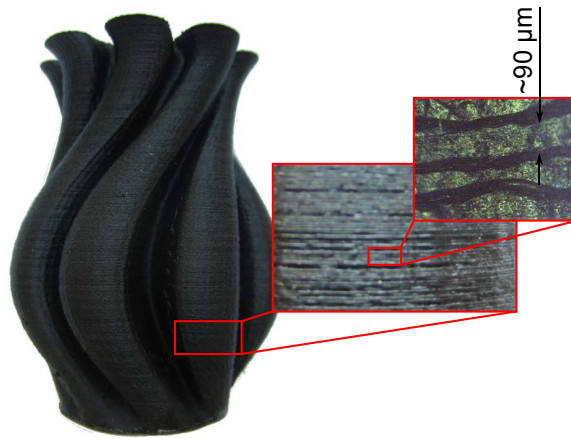


Figure 3.2.: Example of a printed vase, printed with the FabbsterG 3D printer and ABS filaments. A microscope image with 6.25x magnification shows the layer thickness.

A huge disadvantage of this printer is that it is a proprietary closed system. From the software, which creates from a STL file G-code commands, to the deposition mechanism, everything is proprietary. Also the mechanical

construction is not really torsion-resistant, this leads to printing errors in the 2D printing mode. The price for the stick filaments is around five times higher than that for standard round filaments. The mechanical connection between the sticks is also an error source.

3.2. Modification for 2D Print

In this section, the necessary modifications to manufacture 2D printed structures are described, as already mentioned. The main problem was the proprietary 3D printer and the software. This means that a lot of reverse engineering is necessary to use the FabbsterG 3D printer for our purpose. This work can be divided into a mechanical and electrical hardware part, the software manufacturing to create your own G-code, and a calibration of the new setting options. Fig.3.3 shows the reconstructed extruder unit with the self-developed piston dispensing system, and a laser thickness measurement system. The layer thickness measurement is described in section 4.1.

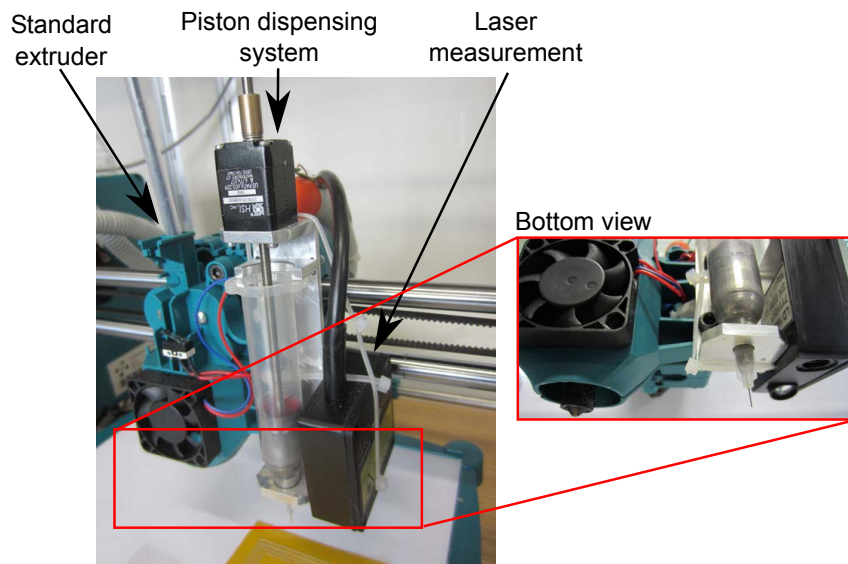


Figure 3.3.: Modifications of FabbsterG 3D printer to manufacture thin-film magnetic sensors. The standard extruder is adapted with the piston dispensing system and a laser measurement system.

3.2.1. Hardware

The developed hardware can be divided into a mechanical and electrical part. The electrical part is the more difficult one, because the FabbsterG printer has no communication interface to control third-part software. This part would be easier with an open-source 3D printer. For example, with the open-source 3D printer RepRap (replicating rapid prototyper), it is possible to control other hardware parts with the original software.

Mechanical Part

To use the 3D printer as a 2D printer, a new piston dispensing system was developed. The dispensing unit was mounted directly on the existing extruder. The bracket for the 10 ml cartridges (No.7012114, Optimum, Nordson EFD) was designed with Inventor 2014 a CAD (computer-aided design) program. The mechanical construction was carried out by our own metalworking department at our institute. To save weight of the system aluminum was chosen for the bracket. The bracket is shown in Fig.A.1 and the assembly drawing in Fig.A.2 and Fig.3.3.

For the high-viscosity conductive silver inks, the “white” (No.7012178) piston is used. For the reactive silver ink, as described in section 2.5, the “red” one (No.7012180) is used. This piston prevents the leakage of the low viscous reactive silver ink through the piston. All these pistons have a diameter of $d=18$ mm.

The stainless steel dosage nozzle (No.7018395) has a diameter of about 0.2 mm, and it is fixed on the cartridge with a Luer-Lock fitting. This nozzle shows the best compromise of print quality, nozzle clogging, and printing speed. For further investigation of the printing parameter, see section 3.3. The end of the nozzle is at the same height as the 3D printer extruder. Therefore, it is possible to print 2D structures also on 3D printed objects at the same level.

The mechanical construction limits the printable structures on the printer table. The nozzle of the piston dispensing system has an offset of 58 mm in the X-axis and -22 mm in the Y-axis. This limits the size of the printable structures to 167 x 203 mm.

To build up a pressure inside the cartridge, a linear stepper motor (21F4U-05-152, Hydronkerk) presses a spindle on the cartridge. It is a bipolar linear stepper motor with 5 V operating voltage. The motor can build up a force of about 100 N, and the linear resolution per step is just $\varepsilon=1.5$ $\mu\text{m}/\text{step}$ in full-step mode. Theoretically, it is possible to operate the motor in a sixteenth-step mode, and therefore, the linear resolution per step is just $\varepsilon=0.09$ $\mu\text{m}/\text{step}$, but this resolution is lower than the backlash of the nut. However, this linear stepper motor shows a really good resolution, and it is easy to control it with a micro-stepper driver. The motor is flange-mounted on the outside of the bracket as seen in Fig.A.2 and Fig.3.3.

The volume V_{step} dispensed per each step of the motor can be calculated according to

$$V_{step} = \frac{d^2 \pi}{4} \cdot \varepsilon \quad , \quad (3.1)$$

where d is the diameter of the cartridge and ε is the linear resolution per step. Therefore, the theoretical dispensing volume V_{step} in full-step mode with this system ($d=18$ mm, $\varepsilon=1.5$ $\mu\text{m}/\text{step}$) is $V_{step}=389$ nl/step. As discussed in section 3.4, the volume per step depends on more variables, but it is sufficient to use this calculation for our purpose. The volume flow \dot{V} through the nozzle is determined by the time t between the steps, but it also depends on the

electronic components of the system. The relation between the volume flow \dot{V} and the time t between the steps will be shown in section 3.2.3.

Electrical Part

As seen in section 3.2.2, it is possible to control the FabbsterG 3D printer with G-code commands. The problem was here, to find a interface to control the linear stepper motor with G-codes. This problem was solved by reverse engineering. With a trial-and-error method, the G-code command to turn the extruder on, was found. With an oscilloscope (TDS 1002, Tektronix) the voltage signals of the two coils of the extruder stepper motor were recorded and evaluated. In Fig.3.4, the voltage signals of the two coils with and without an extruder signal are shown.

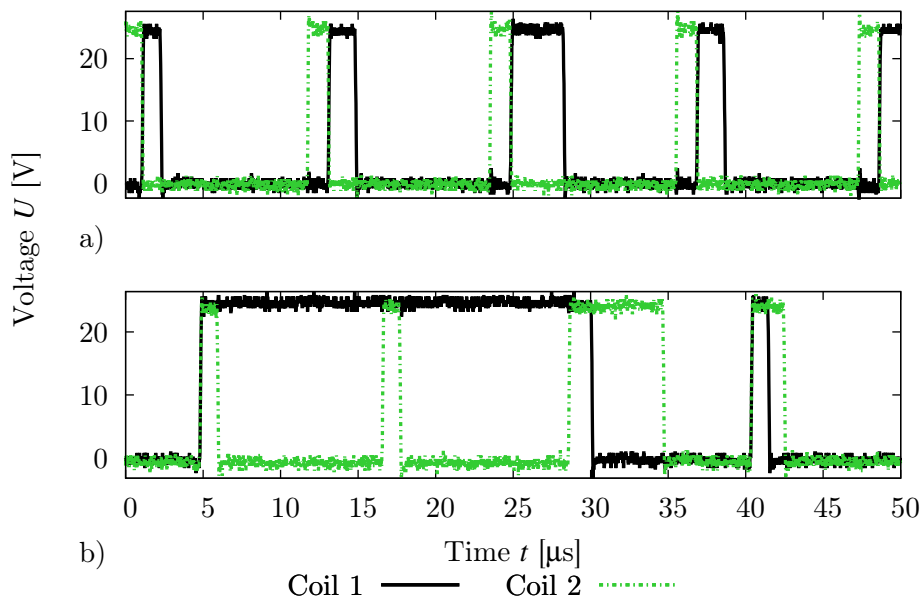


Figure 3.4.: Measurement of the extruder motor signal. When the extruder motor is on, one of the coil changes the length of the cycle duration of the voltage U . a) Without an extruder signal. b) With an extruder signal.

It is visible that the duration time of the rectangle signal changes the length when the extruder is running. This condition can be used to program a microcontroller, which turns the linear stepper motor for the piston dispensing system on.

In the current thesis, a microcontroller Arduino UNO [33] is used. Arduino UNO is a single-board microcontroller. The hardware consists of an open-source hardware board, designed around an 8-bit Atmel AVR microcontroller. It has a USB interface, 6 analog input pins, and 14 digital I/O pins. The Arduino has its own IDE (integrated development environment) and it is programmable in C or C++. It is easy programmable and cheap in acquisition.

A motor driver with built-in translator is necessary to control the bipolar stepper motor. For our purpose, a microstepping driver with translator, and overcurrent protection (A4988, Allegro) [34] is used. It is designed to operate bipolar stepper motors in full, half, quarter, eighth, and sixteenth-step modes, with an output drive capacity of up to 35 V and 2 A.

A key advantage of these two components is that the same components are used in all open-source 3D printers (e.g. RepRap). Therefore, it is possible to transfer the piston dispensing system to another 3D printer without adaptations.

Fig.3.5 shows the hardware board with Arduino UNO microcontroller and the A4988 stepper driver. Fig.A.3 shows the wiring diagram of the board. The board is power supplied by the 3D printer power unit. To supply the microcontroller and the stepper driver with 5 V logic voltages, a voltage divider is implemented. The linear stepper motor is supplied by 24 V, because the stepper motor regulates the current for the motor. Listening A.1 shows the complete Arduino UNO program to control the stepper motor.

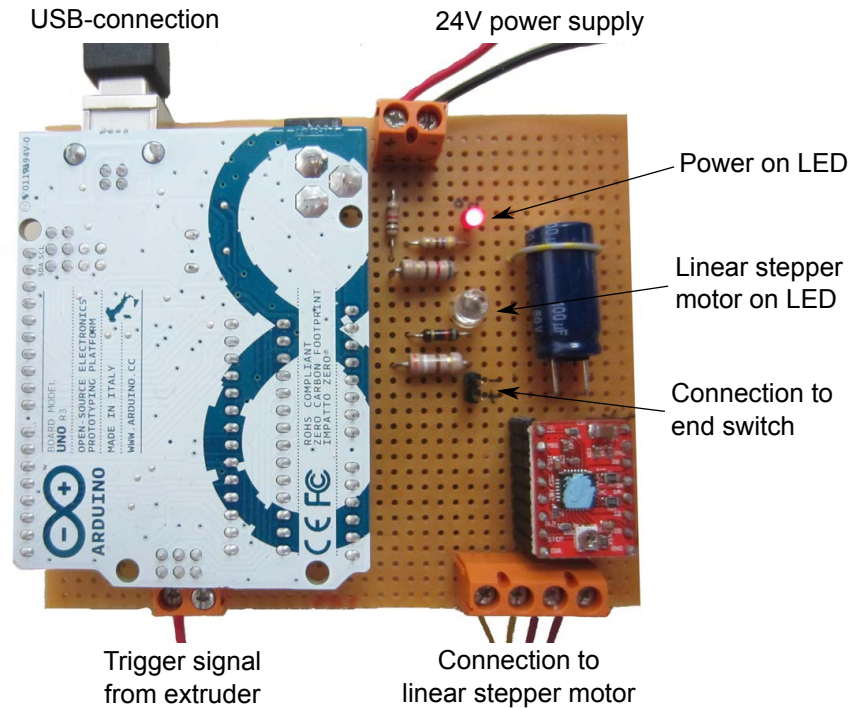


Figure 3.5.: Self-made hardware board for the 2D print setup.

The microcontroller can communicate with a PC over a simulated serial interface. With this interface it is possible to change the time between the steps, and therefore, the volume flow \dot{V} of the dispensing system. Line 20 until 185 in listening A.1 define the different I/O-ports as input or output functions for the step-mode and communication with the PC. The main loop of the program works in the following way:

1. The number when the trigger signal (signal from the extruder motor) is high is counted (variable i).

2. This counting process is iterated for 20 times and the maximum of i is the result of the process.
3. If i is higher than a threshold value the extruder motor is on.
4. The linear stepper motor is turned on and moved ten steps forward instantly.
5. The time t between the steps (volume flow \dot{V}) is determined by a variable which can change it by the serial interface.
6. If i is lower than the threshold value the extruder motor is off.
7. The linear stepper motor is turned off and moved ten steps backwards instantly.
8. Information about the print parameters is displayed on the PC.

It should be noted that for every loop the microcontroller needs 68 ms. This means, the maximum volume flow \dot{V} is restricted by the performance of the microcontroller and the algorithm. In section 3.2.3, the correlation of the volume flow \dot{V} and the time t between the steps is described. An extruder speed of 50 rpm shows the highest stability of the system, because it leads to a high count of the variable i .

With this algorithm and hardware it is possible to use the proprietary FabbsterG 3D printer for our purpose to print magnetic thin-film sensors. The following section describes the program to create the G-code commands, and an explanation is given, how to use this software for the production of patterns for magnetic sensors.

3.2.2. Software

To manufacture pattern with the 2D dispensing system, it is necessary to draw or program the pattern, and transfer it to the printer control. As described in section 1.3, for the 3D printer slicer programs are available to create the G-code commands for the printer control from a STL file. Unfortunately, these slicer programs are only for 3D print applicable. To create 2D pattern, like a square coil, for example, it is necessary to program an own software. For this task the proprietary of the FabbsterG printer is still the main problem. Open-source printers (i.e. RepRap) use standardized G-code commands [35]. For our printer, the required G-code commands have to be guessed by trial-and-error method. Tab.3.1 listed the investigated G-code commands.

It was not possible to find G-codes for the extruder speed control, or for an interruption of the print. The dispensing speed v is one of the most important setting parameter for a good print result. Therefore, it is necessary to find a way to control the speed v of the printer head. The idea is here, to move the extruder one step forward and a smaller step backwards. The step size Δs controls the speed v of the extruder. Fig.3.6 shows the schematic principle of

G-code	description
G 90	set to absolute positioning
G 21	set units to millimeters
M104 S0	extruder temperature (0°C)
G1 X10 Y10 Z0.1	controlled move, go in a straight line from the current (X, Y, Z) point to the point (10, 10, 0.1)
M108 S50	set extruder speed (50 rpm)
M18	disable all stepper motors

Table 3.1.: Investigated G-code commands for the FabbsterG 3D printer. Found by trial-and-error method.

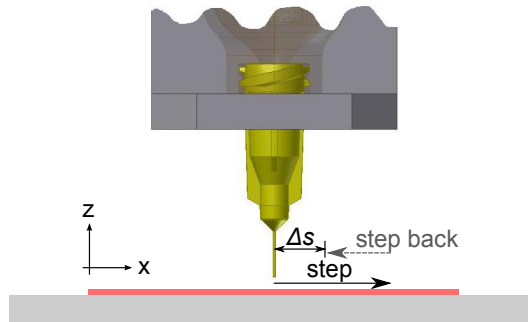


Figure 3.6.: Principle of the speed control for the 2D print setup.

the idea. In section 3.2.3 a calibration of the step size Δs and the speed v of the extruder is presented.

The G-code commands can be transferred to the printer control with the Netfabb software. To create the file with the G-code commands a self-written Python script is programmed. In A.2, the Python script for manufacturing of different pattern is listened. In the current version 1.0, it is possible to produce structures with following functions:

- **Line:** Create a straight line from the current point $(x_{start}, y_{start}, z_{start})$ to the end point (x_{end}, y_{end}) . The z-axis is fixed during the printing process.
- **Circle:** Create a circle with the radius r . It is necessary for the manufacturing a juncture with the printed pattern and a continuing wire for example.
- **Square:** Create a square search coil sensor for the measurement of the magnetic flux density B_z . The length a , number of turns N and the pitch-width s are modifiable.
- **ArchSpiral:** Create an Archimedean spiral for the magnetic flux density B_z measurement. The start angle φ_{start} , end angle φ_{end} and κ sets the size of spiral. The characterization of the function in Cartesian coordinates is: $f: \varphi \mapsto (r \cos \varphi, r \sin \varphi) = (\kappa \varphi \cos \varphi, \kappa \varphi \sin \varphi)$.

In Fig.3.7, an example of manufactured patterns is shown. The green area represents the printable size of the 2D print system. The border marks the edge of the printer table. A square search coil sensor with a length of $a=40$ mm, number of turns $N=4$, and a pitch-width $s=2$ mm is pictured. Also an Archimedian spiral sensor with a start angle $\varphi_{start}=0$, an end angle $\varphi_{end}=13\pi$, and a size parameter $\kappa=0.5$ mm is printed.

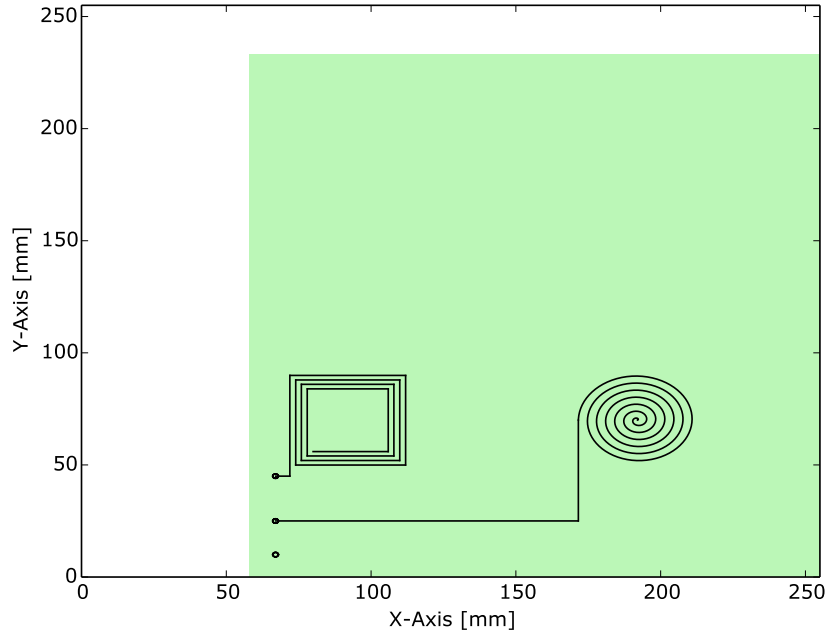


Figure 3.7.: Example of the Python script to create G-code commands for FabbsterG 3D printer. The green area represents the printable size of the 2D print system.

This self-programmed Python script enables to “drawing” (program) of diverse pattern with the piston dispensing system. The challenge was here the proprietary system of the FabbsterG 3D printer. The following section describes the calibration of the new available setting parameters of the 2D print setup.

3.2.3. Calibration

In the last section new setting parameters are defined. For a good printing result the velocity v of the nozzle and the volume flow \dot{V} are the most important parameters. This section describes the calibration of these variables by parameters of the system.

At first, the velocity v of the nozzle is calibrated. As described in the last section, it is not possible to define the speed with a G-code command. The idea is to move the extruder one step forward and a smaller step backwards (Fig.3.6). The step size Δs controls the speed v of the extruder. For the

calibration a line with $\Delta x = 200$ mm is printed with different step sizes Δs and the dispensing time Δt is measured. The velocity of the nozzle is $v = \Delta x / \Delta t$. Fig.3.8 shows the relation between the nozzle speed v and the step size Δs . The velocity v is linearly dependent from the step size Δs .

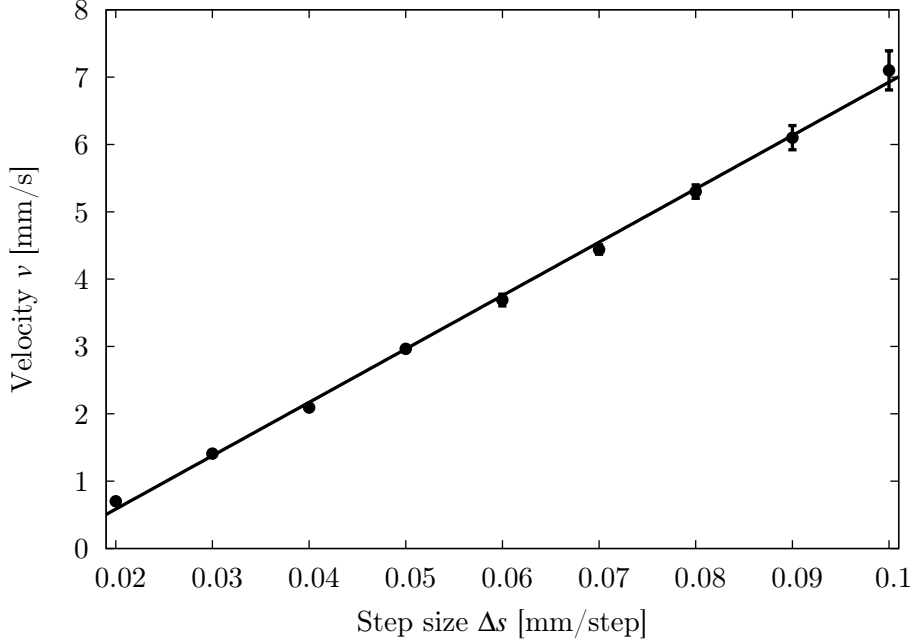


Figure 3.8.: Extruder velocity v as a function of the step size Δs .

The next important parameter is the volume flow \dot{V} . The volume flow \dot{V} depends on the time t between two steps and the step mode γ of the stepper driver. As described before, the time t has an offset t_{offset} , which depends on the performance of the microcontroller and the algorithm. In the current system the offset time is $t_{offset} = 68$ ms. The volume per step in the full step mode is $V_{step} = 389$ nl/s (see Eq.3.1). With this values it is possible to calculate the volume flow $\dot{V}(t)$ of the system, accordingly to

$$\dot{V}(t) = \frac{V_{step}}{(t + t_{offset}) \cdot \gamma} \quad . \quad (3.2)$$

Fig.3.9 shows the relation between the volume flow $\dot{V}(t)$ and the time t between the steps. It is obvious that in the eight $\gamma=8$, or sixteenth $\gamma=16$ step mode it is not possible to reach a volume flow higher than $\dot{V}=356$ nl/s and $\dot{V}=712$ nl/s, respectively. This is a result of the time offset t_{offset} of the microcontroller.

On the assumption of a constant cross-sectional area A of the printed pattern, the volume flow $\dot{V} = V / \Delta t$ is linearly dependent from the printing speed $v = \Delta x / \Delta t$. Therefore, these two parameters correspond with each other, according to

$$\dot{V}(t) = A \cdot v(t) \quad . \quad (3.3)$$

These new printing parameters can be used to find the best printing result, as performed in the next section.

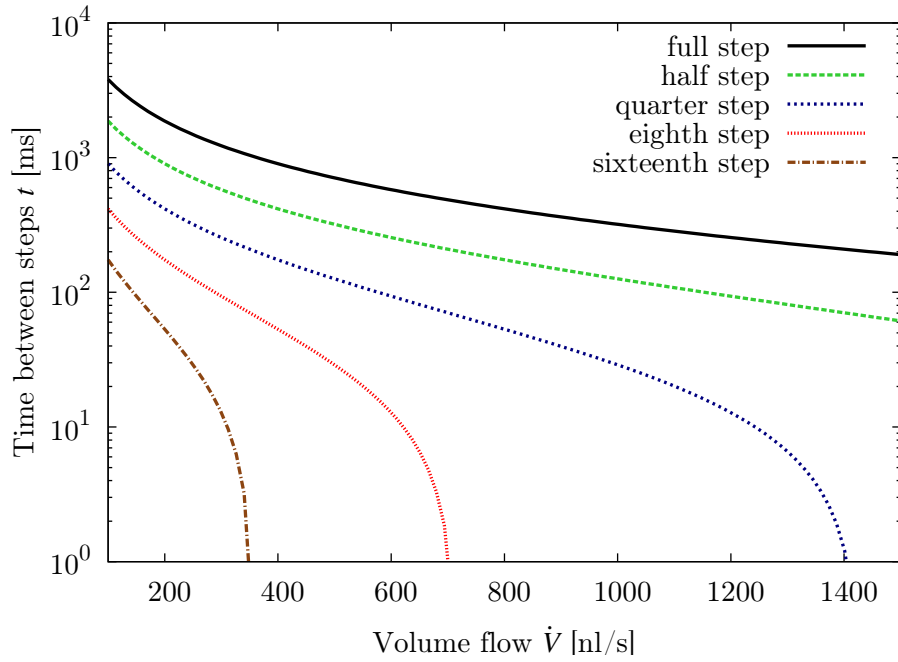


Figure 3.9.: Volume flow \dot{V} as a function of the time t between two steps.

3.3. Parameter Study

In order to find the best printing parameters, a parameter study is performed. In theory the volume flow \dot{V} is linearly dependent from the printing speed v (see Eq.3.3). In practice more unknown variables affect the printing result.

Experiments show that the nozzle speed v affects the result even more than volume flow \dot{V} . For that reason, some test patterns at different print head speed v are printed. The volume flow \dot{V} is constant with $\dot{V}=200$ nl/s. It can be seen in Fig.3.9, that it is possible to operate the linear stepper motor in sixteenth-mode. Nevertheless, also with this small resolution per step ε , the dosing of the silver ink is not uniformly distributed. This can result in some errors in the print quality. In section 3.5, a dispensing system is described which guarantees a continuously dispensing of the ink. Fig.3.10 shows the test pattern at different speeds v of the printer nozzle. As silver ink, Circuit Works CW2200 is used. For this study, the patterns are printed on a $150\text{ }\mu\text{m}$ thick PET foil. In several tries a printer speed of $v=5$ mm/s shows the best printing result.

To verify the theoretical relation (Eq.3.3), the thickness h of the printed structure is measured. As described in section 2.3, the cross-sectional area A has the shape of a circular segment, but it can be approximated by a rectangle with $2/3$ of the total height. Than one has: $A = 2/3 \cdot w \cdot h$, where w is the width and h is the height of the trace. Fig.3.11 shows the thickness h of the printed pattern as a function of the printer speed v .

The thickness h is not in the same range as the theoretical value, due to some unknown variables. Also a change in the volume flow \dot{V} has not the same impact as in the model. On the other hand, in Fig.3.11 the width w of

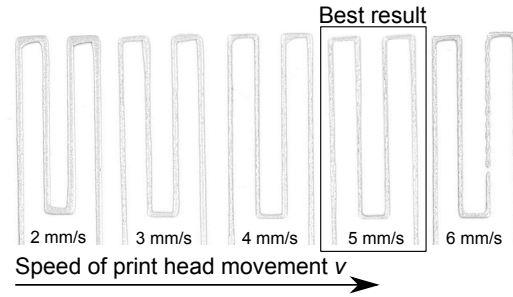


Figure 3.10.: Parameter study of the printer speed v . A speed of $v=5$ mm/s shows the best printing results. The volume flow for this experiment was $\dot{V}=200$ nl/s. Silver ink: CW2200 on PET substrate.

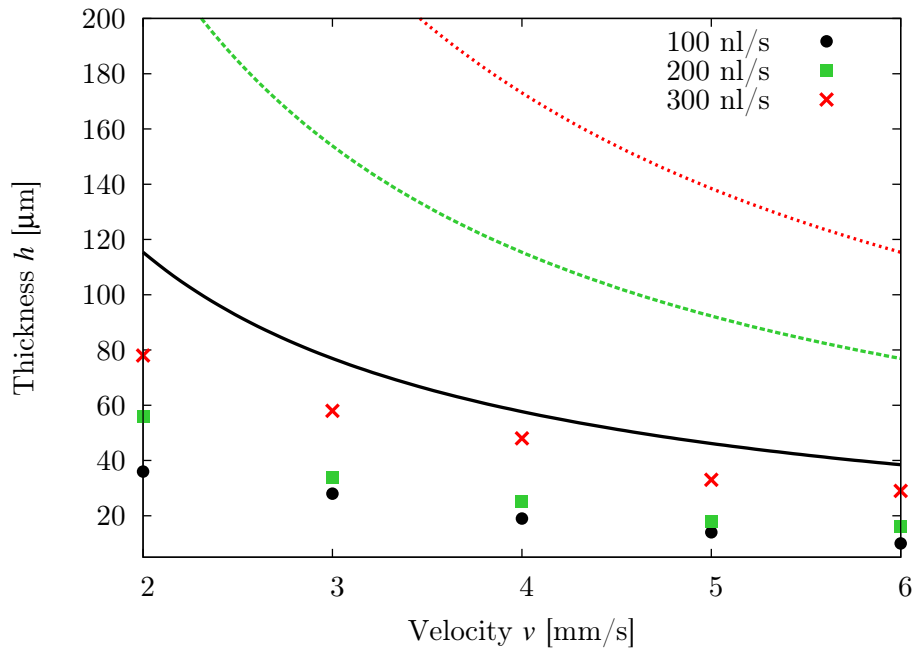


Figure 3.11.: Thickness h of the printed pattern as a function of the printer speed v . The solid lines represent the theoretical relation according to Eq.3.3. The average width of the structure is $w=0.65$ mm. Silver ink: CW2200 on PET substrate.

the structure is fixed. This is also not correct, because the width w changes also with the nozzle speed v . However, it can be seen that the thickness h of the structures decreases with the printer speed v and the volume flow \dot{V} . In the next section, some of these unknown variables are investigated by using FEM simulations.

At next, the different inks and substrates are tested. In Fig.3.12 a comparison between the different inks and the PET, Kapton substrate is shown. As printing parameters a printing speed of $v=5$ mm/s, and a volume flow $\dot{V}=200$ nl/s are chosen. This parameters show the best printing results.

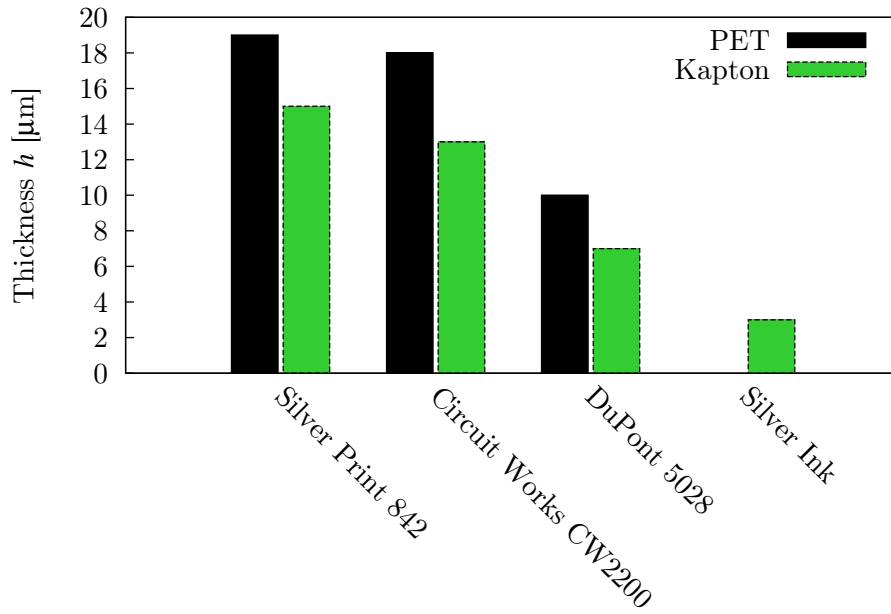


Figure 3.12.: Comparison of the thickness h at different inks and substrates. Printing speed $v=5$ mm/s, volume flow $\dot{V}=200$ nl/s. No data for silver ink on PET is available.

It can be seen that the thickness h of the printed pattern depends also on the chosen ink and the used substrate. The self-made reactive silver ink shows the thinnest printing result, but as described in section 2.5, it is not easy to print it without substrate preparation. From the high viscosity inks, the ink from DuPont shows the best result. The substrate influences the result as well. Kapton is therefore, the thinnest, and best printable substrate for magnetic thin-film sensors. As described above, silver ink Circuit Works CW2200 is the best choice for our purpose.

In summary it can be said that with a $d=0.2$ mm nozzle, structures with an average width of $w=0.65$ mm can be manufactured. The thickness h depends on the printing velocity v , but it is mostly independent from the volume flow \dot{V} . The experiments show the best printing result for a printing speed of $v=5$ mm/s and a volume flow of $\dot{V}=200$ nl/s on Kapton substrate.

3.4. FEM Simulations

This section describes the possibility of FEM (finite element method) simulations to find the mismatch of the experimental values and the theoretical model, according to Eq.3.3. Finite element methods are powerful simulation tools of continuum physics for the study of static and dynamic mechanical problems as well as transport processes e.g. for heat and fluids [36]. In contrast to analytical calculation methods where the real stress state in a component is idealized by a usually highly simplified model, with FEM simulations even complicated geometries, and for analytical considerations relatively difficult properties can be accurately considered. The FEM principle is based on a division of the general problem into a large number of small particular problems. The component is divided into individual, discrete elements. For the determination of a variable of a single element (e.g. stress, shift), a system of differential equation is set up. In contrast to analytical methods, the approach function is therefore, established only for parts (individual elements), not for the entire component. The boundary conditions for the calculation of an element are obtained by external influences to the node (corner point of a single element) local, or by the load state of the adjacent elements, because they are continuously connected through the node to the considered element. The coefficients of the initial function are derived from the degrees of freedom of the nodes. These are for strength calculations, three translational (x, y, z) and three rotational (f_1, f_2, f_3) degrees of freedom per node. Even more coefficients appear from the material data, for example such as the stiffness matrix. The resulting equations are calculated by FEM programs with numerical methods. Finite difference methods, approaches or series variation method are used for example.

For our purpose, two different simulation techniques are used. To simulate the volume flow \dot{V} as a function of the dispensing height Δz a CFD (computational fluid dynamics) simulation is used. This type of FEM simulation solves the problem by calculating the fundamental Navier–Stokes equations [37]. On the other hand, mechanical structure simulations of the bracket are carried out. This type of simulation are based on the “minimum total potential energy principle” [36].

The simulations are implemented in COMSOL Multiphysics 4.4 [38]. It is a finite element analysis, solver, and simulation software for various physics and engineering applications, especially coupled phenomena.

3.4.1. CFD Simulation

It is obvious that the volume flow \dot{V} depends on the pressure p inside the cartridge and the nozzle diameter. However, it was suspected that also the dispensing height Δz (Fig.1.8) plays a crucial role in the dispensing. The problem of our setup is that it is not easy to control the dispensing height Δz accurately. Also the stability of the mechanical structure of the FabbsterG 3D printer is not sufficient. To verify the theory, a 2D axialsymmetric laminar

flow COMSOL CFD simulation is figured out.

This study is more qualitative, because the pressure drop Δp inside the nozzle is not well known. It can be approximated by the Hagen–Poiseuille equation [39], according to

$$\Delta p = \frac{8\mu l \dot{V}}{\pi r^4} \quad , \quad (3.4)$$

where μ is the dynamic viscosity, l is the length, and r is the radius of the nozzle. The length of the nozzle is approximately $l=30$ mm. For the dynamic viscosity μ , the values from the Circuit Works CW2200 and from the reactive silver ink are used. The volume flow is assumed with $\dot{V}=200$ nl/s. With these approximations a pressure inside the cartridge of $p=500$ Pa is applied.

With a parametric sweep the different dispensing heights Δz are simulated. Fig.3.13 shows the pressure drop Δp at three different dispensing heights Δz . At a small dispensing heights Δz , the pressure drop Δp is dominated by the substrate. At large dispensing heights Δz , the pressure drop Δp is mainly determined by the nozzle. Between these two extremes, a transient region is visible, where the pressure drop Δp is effected by both of them.

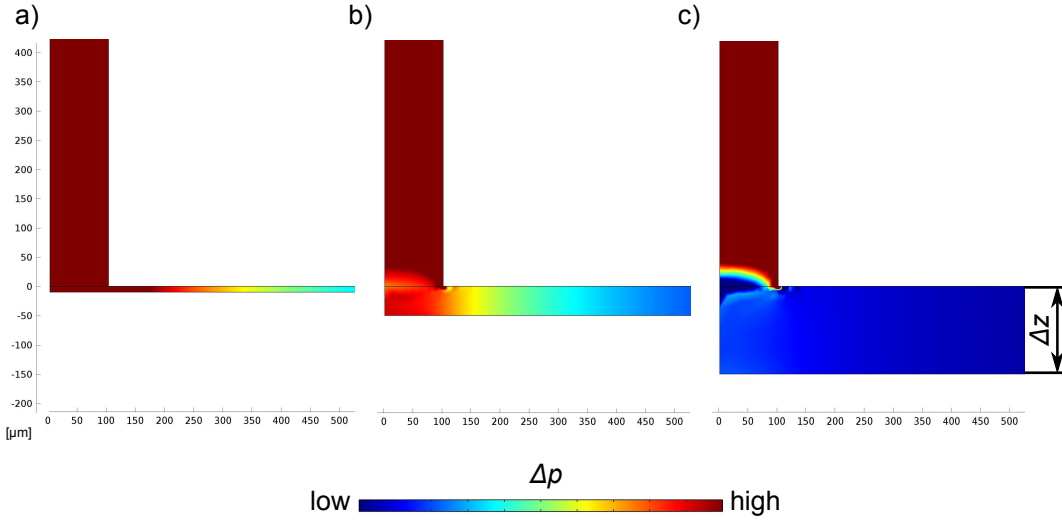


Figure 3.13.: FEM simulation of the pressure drop Δp at different dispensing heights Δz between the 0.2 mm nozzle and the substrate. a) Dispensing height $\Delta z=10$ μm . b) $\Delta z=50$ μm , $\Delta z=150$ μm .

The volume flow \dot{V} as a function of the dispensing height Δz is shown in Fig.3.14. The dispensing height Δz , and the viscosity μ of the ink change the dispensing property. The volume flow \dot{V} decreases, if the dispensing height Δz is smaller than a certain value.

The analysis shows that the dispensing height Δz is an important parameter for good printing results. The problem with our setup is that no possibility to control this parameter is available.

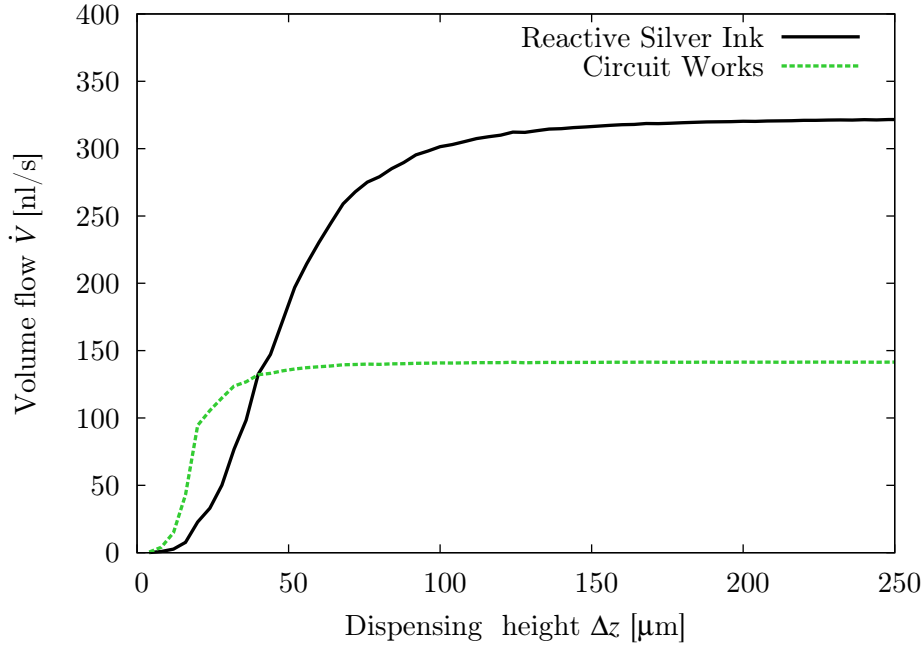


Figure 3.14.: Volume flow \dot{V} as a function of the dispensing height Δz . The viscosity of the ink influences the volume flow \dot{V} .

3.4.2. Mechanical Structure Simulation

The mechanical structure of the self-made aluminum bracket is also simulated. The problem is here, that the aluminum bracket is not really torsion-resistant. If the spindle of the linear stepper motor presses on the piston, the bracket is deformed. The force F is applied on the upper and bottom side of the bracket. The force F which is necessary for the dispensing can be divided into two parts. The pressure drop Δp from the ink and the friction force F_f which originates from the friction between the piston and the cartridge. The force from the pressure drop $F_{\Delta p} = \Delta p \cdot r^2 \pi$ can be neglected, because the friction force F_f is some decades higher than the force from the pressure drop $F_{\Delta p}$. A force $F=20$ N is assumed for this simulation.

Fig.3.15 shows the mechanical structure simulations of the self-made aluminum bracket. Fig.3.15 (a) shows the displacement of the bracket as a result of the external force. Fig.3.15 (b) shows the von Mises stress σ_v . Von Mises stress is defined as a fictitious uniaxial stress, which is the same material stress as a real, multi-axial stress state.

A maximum displacement of $f=0.15$ mm is found. This means that the dispensing volume V_{step} of one step can vary by some decades. The maximum von Mises stress is about $\sigma_v=21$ N/mm². The maximum of σ_v is located at the connection between the bracket and the 3Dprinter extruder.

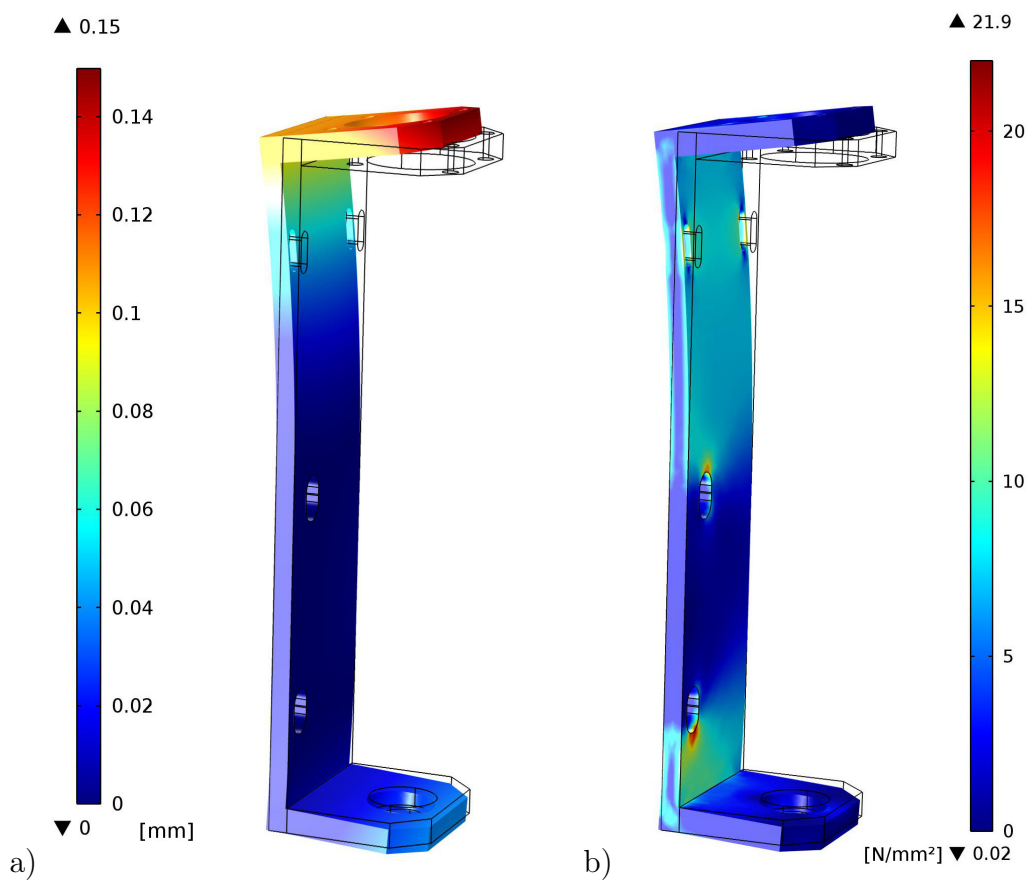


Figure 3.15.: Mechanical structure simulations of the self-made aluminum bracket. a) Displacement f . b) Von Mises stress σ_v .

3.5. Improvement Opportunities

This section should describe measures to improve the printing result and usability for the next generation of combined 3D/2D printer. The used 3D printer FabbsterG from Sintermask is proprietary. Therefore it is not possible to change the system in decent way. An open-source 3D printer would be a better basic system, for example the 3D printer from RepRap. With this printer it would be possible to control also third part systems with the original components and software. Another idea is to use an existing XYZ scanning chamber of the institute [40]. With this system it would be possible to create our own 3D/2D printer. No commercial components would be necessary. This opens up new possibilities in sensor manufacturing. The maximum size of the sensors could be a problem in the future. The size is restricted by the size of the printer table. With the XYZ scanning chamber sensors with a size up to 1500 x 1400 mm would be possible.

With a new non-proprietary system better opportunities to control the printer parameters are available. The printer speed v can be controlled exactly. Nevertheless also improvement opportunities on the self-made dispensing system are available. With the linear stepper motor it is not possible to control the volume flow \dot{V} continuously. A better and easier system would be an air-pressure based system. With such a system the pressure inside the cartridge can be controlled continuously and more accurate.

As described in section 3.4 the dispensing height Δz plays a crucial role for a good print quality. The current system is too unstable and it is not possible to calibrate the right dispensing height Δz accurately enough. This problem can be only solved with a new system. For example with the existing XYZ scanning chamber the dispensing height Δz can be controlled very accurate. The displacement of the bracket is in the current version also too high. As it is well known the displacement f depends on the E-module E of the material [41]. The displacement f is inversely proportional to the E-module E , ($f \sim 1/E$). The E-module of aluminum is rather low with $E=70 \text{ kN/mm}^2$. Steel has an E-module of $E=210 \text{ kN/mm}^2$. This results in a lower displacement f of the bracket. However, the best solution would be an air-pressure based dispensing system. With such a system no displacement of the bracket would exist.

This work represents a pilot study to find the best setup and printing parameters for a further project. With these improvement opportunities it is possible to create better printing results in the future.

4. Sensor Manufacturing

The last section described the experimental setup, and the printing parameters to manufacture thin-film magnetic sensors. This section describes the manufacturing of the sensors. The sensors are manufactured by means of the new developed 3D/2D printer. In this pilot study magnetic thin-film sensors for the measurements of the off-plane flux density B_z should be manufactured. For that reason, the best design for such sensors is investigated. As a first test a search coil is printed on PET. The second sensor is an array of four search coils printed on Kapton foil of reduced thickness.

4.1. Combination of 3D/2D Print

The first idea was to manufacture magnetic thin-film sensor without a substrate foil. As a substrate material a thin film of 3D printed ABS substrate should be applied. This section describes the impracticality of this idea.

For that reason, a thin layer of ABS was printed directly on the printing table. The STL-file was created in Inventor 2014, and the file was imported in the Netfabb software. The printed layer should have dimensions of 40 x 40 x 0.05 mm. We choose “fine” as a printing style in the Netfabb software. With this style it should be possible to print structures with a layer thickness $<44\text{ }\mu\text{m}$. During the print, the table was heated up to 80 °C, and the extruder temperature was 280 °C. After the first layer, a relatively wide line with the self-made reactive silver ink was printed, by using the standard 2D printing parameters. As an advantageous effect, the ink is cured directly on the printer bed. For that reason the bed was heated up to 90 °C for 10 min. The reactive silver ink showed a good conductivity on the ABS substrate. As third step, a second layer (20 x 40 x 0.05 mm) of ABS material, with the same printing parameters, was printed over the silver ink. This film served as a dielectric and protection layer. Fig.4.1 shows a picture of the printed structures on the printing table.

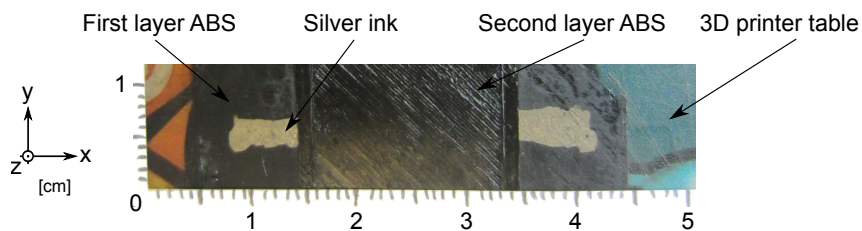


Figure 4.1.: Test of a combined 3D/2D printer printed structure.

It was really difficult to peel off the structure from the printing table, due to the high temperature of the printer bed during the print prevents this. On the other hand, if the printer bed temperature is lower, it is not possible to print a solid layer. A lot of errors occur with a low printer bed temperature. Another problem is that the deposit silver ink line loses its conductivity after the second layer of ABS is printed over the conductive line. The melted plastic from the second layer compounded with the plastic from the first layer, and therefore, it destroyed the solid line of silver ink. No solution has been found yet to prevent this, and retains the conductive properties of the line. Finally, the layer thickness tends to be rather high. To examine the thickness, a contact-free laser thickness measurement system was installed. This system was directly mounted on the extruder unit of FabbsterG 3D printer. Fig.3.3 shows the laser measurement system.

The laser distance measurement is based on the triangulation principle. A laser beam is focused on the measurement film, and the reflection is detected by a CCD (charge-coupled device) array which is located next to the laser. If the distance between the measured film and the sensor changes, also the angle, at which the light spot is observed, changes. With trigonometric functions it is possible to calculate the distance Δz of the change of position.

To measure the thickness h of the printed structures a contact-free laser thickness measurement system (optoNCDT1605-20, Micro-Epsilon) is used. This sensor has a measurement range from ± 10 mm, and the resolution is $6 \mu\text{m}$. The problem of laser based measurement systems is that errors can occur, if transparent materials are measured. For that reason, it is not possible to measure PET or Kapton with this system. The sensor controller returns a voltage value proportional to the thickness of the object. These values are recorded with a DAQ (data acquisition) card (NI USB-4431, National Instruments). Fig.4.2 shows the schematic principle of the measurement setup. To improve the accuracy of the measurement a high integration time of $20 \mu\text{s}$ is chosen. The calculation of the layer thickness h is carried out in LabView 2012.

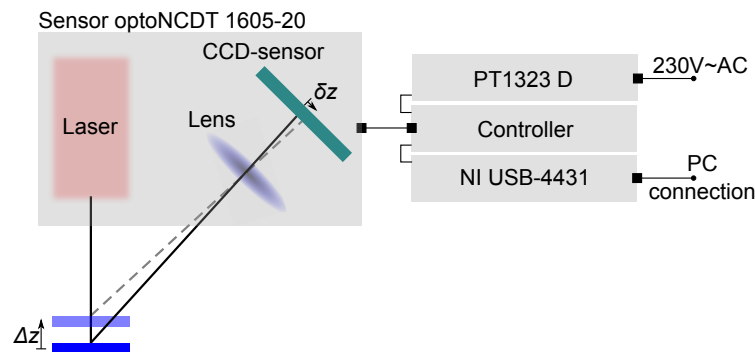


Figure 4.2.: Schematic diagram of the laser measurement setup to measure the layer thickness h .

Before the measurement of the layer thickness h can start, the distance between sensor and printer bed has to be calibrated. This is necessary because

the bed and the extruder are asymmetrically mounted. To correct this error the distance on four points are measured and a tangent plane, which corrects the error is calculated. The vectors of these four measured points are [mm]

$$\begin{aligned}\vec{P}_1 &= \begin{pmatrix} 0 \\ 0 \\ 0 \end{pmatrix}, & \vec{P}_2 &= \begin{pmatrix} 0 \\ 10 \\ -0.161 \end{pmatrix}, \\ \vec{P}_3 &= \begin{pmatrix} 50 \\ 10 \\ 0.412 \end{pmatrix}, & \vec{P}_4 &= \begin{pmatrix} 50 \\ 0 \\ 0.573 \end{pmatrix}.\end{aligned}$$

With these points it is possible to calculate a tangent plane, according to

$$z(x, y) = 0.0115x - 0.0161y \quad . \quad (4.1)$$

The error correction method is implemented in the self-written LabView program. To measure the height profile of the printed structure a resolution of 1 mm was chosen. This results in 500 measuring points. With these data, a topographical map of the printed structure can be prepared. Fig.4.3 shows the height profile of the structure.

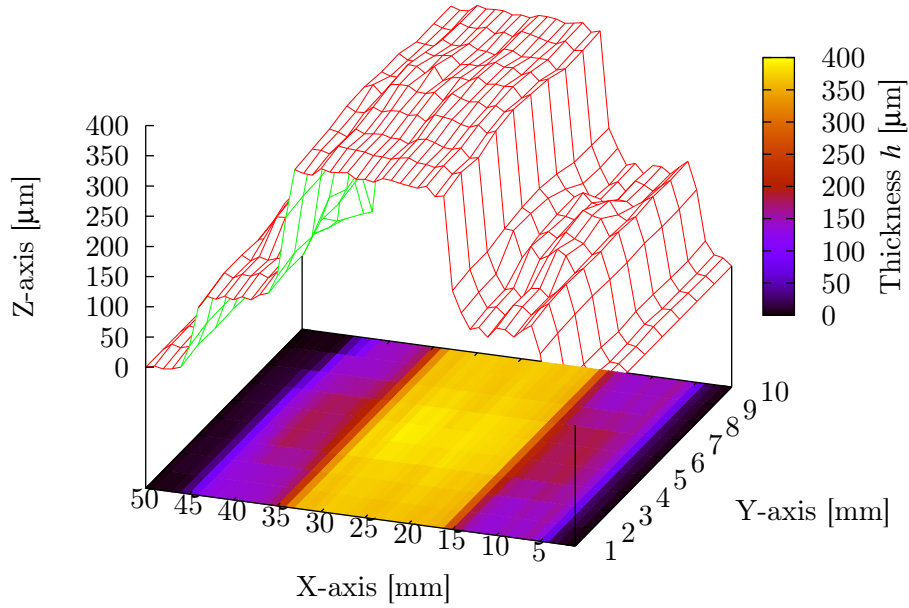


Figure 4.3.: Topographical map of the printed structure, measured with the laser measure system.

Unfortunately, the resolution of the sensor is not high enough to detect the thickness of the silver ink layer. However, it can be seen that the first layer of the ABS material has a thickness of about $h=150\text{ }\mu\text{m}$. The second layer has even a higher thickness of about $h=200\text{ }\mu\text{m}$.

This section shows that it is impossible to combine 3D/2D printed structures at least for thin-film applications. For sizable solid object it could be initialized

a new range of applications. For this work, only thin-film magnetic sensors are of interest. Therefore, the sensors will be printed on an existing thin-film substrate like PET or Kapton.

4.2. Magnetic Flux Density Sensor

This section describes the manufactured magnetic flux density sensors for the off-plane flux density B_z measurements. At first, the sensor design is discussed. Different shapes are possible for the sensor. Also the size is an important parameter of the sensor. As described in section 1.2, the sensitivity of the sensor depends only on the cross-sectional area A of the sensor. For that reason, a calibration of this parameter is necessary. At last, two magnetic flux density sensors are presented. Version 1 is printed on PET, and shows a relatively high thickness h . Version 2 is printed on Kapton. This version is manufactured as an array of four sensors to measure B_z inside a transformer core at different positions at the same time.

4.2.1. Sensor Design

At first, the question about the best sensor shape has to be answered. No publications were found which describe the best shape of a magnetic flux density sensor. With our setup it would be possible to create any kind of 2D structures. However, only two shapes seem reasonable, an Archimedean spiral ($f: \varphi \mapsto (r \cos \varphi, r \sin \varphi) = (\kappa \varphi \cos \varphi, \kappa \varphi \sin \varphi)$) and a rectangular search coil. From printing usability point of view, no preferred shape is obvious. Both shapes are easy to program in the self-made Python script to create G-code commands (Fig.3.7). Therefore, the best shape for the sensor depends only on the sensitivity, and as a consequence on the cross-sectional area A .

The effective area A_{arch} of the Archimedean spiral is

$$A_{arch} = \frac{1}{2} \int_{\varphi_{start}}^{\varphi_{end}} r^2 d\varphi = \frac{1}{2} \int_{\varphi_{start}}^{\varphi_{end}} (\kappa \varphi)^2 d\varphi = \frac{\kappa^2}{6} \cdot (\varphi_{end}^3 - \varphi_{start}^3) \quad (4.2)$$

with the inner radius $r_1 = \kappa \varphi_{start}$, outer radius $r_2 = \kappa \varphi_{end}$, and $\varphi_{end} - \varphi_{start} = 2\pi \cdot N$ follows: $r_2 - r_1 = \kappa \cdot (\varphi_{end} - \varphi_{start}) = 2\pi \cdot \kappa N$ and $\kappa = \frac{r_2 - r_1}{2\pi N}$. With these definitions the effective area A_{arch} can be calculated as

$$A_{arch} = \frac{\kappa^2}{6} \cdot (\varphi_{end}^3 - \varphi_{start}^3) = \frac{\pi N}{3} \cdot (r_1^2 + r_1 r_2 + r_2^2) \quad . \quad (4.3)$$

The calculation of the effective area A_{rect} of a rectangular square sensor is much simpler. The area is just the summation of each rectangular with the length a , according to

$$A_{rect} = \sum_{i=0}^{N-1} (a - 2is)^2 \quad , \quad (4.4)$$

where s is the pitch of the N turns.

To find the sensor shape with the highest sensitivity, the ratio A_{rect}/A_{arch} is numerically calculated. The ratio is given by

$$\frac{A_{rect}}{A_{arch}} \approx 1.27 \quad . \quad (4.5)$$

This means that by the same outer diameter r_2 and length a , respectively, and the same number of turns N the rectangular square sensor with the effective area A_{rect} shows a higher sensitivity. For that reason, we decided to use magnetic flux density sensors of rectangular shape.

The next important parameter is the length a of the rectangular square sensor. To obtain an average value of the magnetic flux density B_z it is necessary to average over several grains of the material. The sensor should be applicable for several transformer core materials. The most important materials are CGO (conventional grain-oriented) and HGO (high permeability grain-oriented) steels. The average grain sizes are 4 mm and 9 mm for CGO and HGO, respectively [42].

To get accurate and statistical stable values an averaging over several grains is necessary. On the other hand, for a good spartial resolution the sensor should be as small as possible. Therefore, as a compromise the length of the sensor, was chosen with $a=20$ mm.

4.2.2. Calibration of the Sensor

It is relatively easy to calculate the cross-sectional area A of the sensor. Nevertheless, some errors are present. The width w and the thickness h of the traces are neglected for example. Also the length a and the pitch-width s of the sensor cannot be exactly determined. For that reason, it is necessary to calibrate the manufactured sensors to get well accurate measuring results of the off-plane flux density B_z .

Fig.4.4 shows the calibration setup. The self-manufactured magnetic thin-film sensor is placed between a high resolution 15“ iron magnet system (B-E38, Bruker). The sensor must be aligned tangentially to the coils. The magnetic flux Φ through the sensor is measured (EF5, Magnet-Physik). Also the magnetic flux density B between the two coils is measured (Teslameter 7030, Sypris) with a Hall sensor probe. With a magnet power supply (647, Lake Shore) B can be controlled. To prevent an overheating of the magnet a heat exchanger (B-MT 15/40, Bruker) is installed.

With the information about the magnetic flux density B and the magnetic flux Φ through the sensor, the cross-sectional area A of the sensor can be calculated, according to

$$\Phi = \int_A B \cdot dA \quad . \quad (4.6)$$

Since the cross-sectional area A is constant and the flux distribution is homogeneous, the effective sensor area is

$$A_{eff} = \frac{\Phi}{B} \quad . \quad (4.7)$$

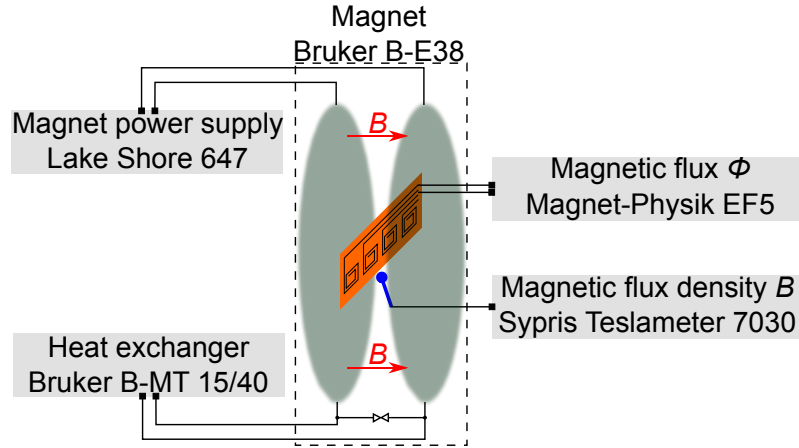


Figure 4.4.: Schematic diagram of the calibration setup.

For a better accuracy of the calibration, the measurement is carried out for four different values of B . For an easier control the current I of the magnet power supply is adjusted. Tab.4.1 lists the relation between the current I and the magnetic flux density B . The arithmetic average of these four measurements is the calibrated cross-sectional area A_{eff} of the sensor.

current I [A]	magnetic flux density $ B $ [mT]
-20	180
-10	81
10	82
20	180

Table 4.1.: Relation between current I and the magnetic flux density B for the calibration.

4.2.3. Sensor Version 1

This section describes the first attempt to manufacture a thin-film magnetic sensor to measure the magnetic flux density B_z in a transformer core. The sensor consists of one rectangular search coil which is printed on a PET substrate. The sensor has a length of $a=20$ mm and it has $N=8$ turns with a pitch of $s=1$ mm. With these parameters and Eq.4.4 a theoretical cross-section area can be calculated to $A_{rect}=15.8$ cm². In Fig.4.5, the manufacturing process is pictured. First, the rectangular square coil is printed on the PET substrate with the standard printing parameters (volume flow $\dot{V}=200$ nl/s, printing speed $v=5$ mm/s), and the standard silver ink CW2200.

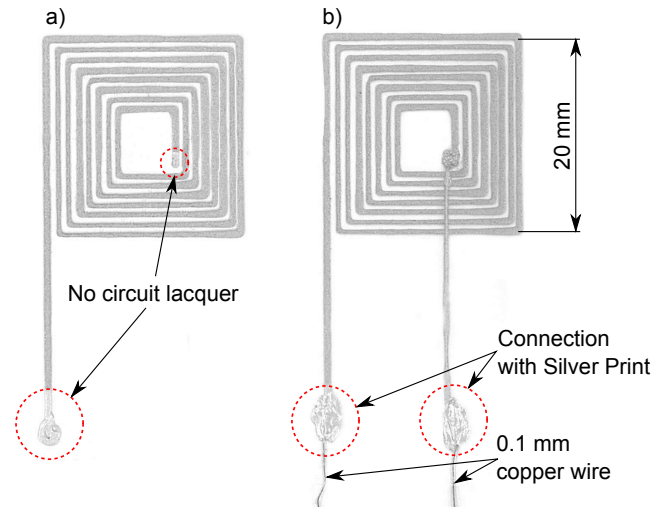


Figure 4.5.: Manufacturing process of the first version of the rectangular square coil sensor. a) First step of the manufacturing process. b) Finished sensor.

After the first step, the junction points are shielded, and the rest of the sensor painted with a circuit lacquer (RS569-290, RS Components). This lacquer is dialectic, and it has a dielectric strength of 400 KV/mm. At the second step the inner junction of the search coil is led out. These outer junction points are connected with a 0.1 mm copper wire. For the connection also a silver ink is used. For the protection of the sensor a second layer of dialectic lacquer is printed.

The sensor has a theoretical cross section of $A_{eff}=19.8\pm0.2\text{ cm}^2$ according to the calibration (compare section 4.2.2). The calibration of the sensor shows a big difference between the theoretical cross-sectional area A_{rect} and the measured area A_{eff} . This discrepancy can be explained by the gap between the two printed supply traces of the coil. The area $A_{gap}=4.8\text{ cm}^2$ between these lines is also a part of the cross-sectional area of the sensor. This is a bad design of the sensor, and this failure will be eradicated for the next sensor version. Nevertheless, the calibration shows a good coincidence between the theoretical value $A_{rect}=15.8\text{ cm}^2$ and the measured value subtracted by the area between the supply traces $A_{eff} - A_{gap}=15.0\pm0.2\text{ cm}^2$.

To control the functionality of the sensor, the value of the resistance R can be used. If some traces are broken, (if the sensor was bent too much, for example) the resistance R of the printed sensor will increase immediately. The resistance of the sensor is measured with a multimeter (187, Fluke), and is about $R=24\Omega$ for correct functionality of the sensor.

The overall thickness h is one of the most important parameters of the sensor. It is measured with a reflected-light microscope (Zeiss-Axioplan, 6.25x magnification). The thickness results from the PET substrate, the silver ink traces, and the dialectic protection layer. The measurement shows a value of $h=186\text{ }\mu\text{m}$. It must be also mentioned that the inner supply trace led out, and that increases the thickness, furthermore. This thickness is for the measure-

ment of the off-plane flux density B_z inside a transformer core objectionable. However, the sensor is not really sensible for damages and other environmental influences. In the next version these bugs can be eliminated. Tab.4.2 shows the most important values of the manufactured sensor.

sensor No.:	length a [mm]	thickness h [μm]	area A_{eff} [cm^2]	rel. error f [%]	resistance R [Ω]
1	20	186	19.8 ± 0.2	25.3	24

Table 4.2.: Summary of the characteristics of the sensor version 1.

4.2.4. Sensor Version 2

In order to eliminate the errors of the sensor version 1, a new design was developed. The new sensor is printed on Kapton which is much thinner than PET. Therefore, the overall thickness h of the sensor is smaller. The new sensor consists of an array of four search coils. With these four search coils it is possible to measure the off-plane flux density B_z inside a transformer core on four position at the same time. This will reduce the measurement time dramatically. Another big disadvantage of the old design is, that also the area between the supply traces contributes to the cross-sectional area. This area distorts the measurement. The new version of the sensor eradicates this error. For that reason, the sensor is double-sided printed. The search coil and one supply trace are printed on the top of the substrate, and the second supply trace is printed on the bottom side. These two traces are connected with a trough hole in the substrate. The hole is made after the print of the top side with a tapered punch. For an exact alignment of these two sides, reference marks are necessary. After the print of the top layer the sensor must be arranged on these reference marks to achieve an overlap at the through hole. Fig.4.6 shows the dimensions of the new sensor version. A picture of the finished sensor is shown in Fig.4.7.

The junctions at the end of the supply traces are connected with a 0.1 mm copper wire, too. The sensor is also protected with the dialectic circuit lacquer on both sides. However, this makes the sensor resistant for the particular requirements inside a transformer core. As a disadvantageous effect, the lacquer layer increases the overall thickness of the sensor.

The calibration of the sensors shows a good agreement between the measured cross-sectional area A_{eff} and the theoretical area A_{rect} . In Tab.4.3, the most important values of the new manufactured sensor are listed. The resistance R of the sensor is much higher than that in version 1. This can be explained by the high resistance of the trough hole. Also the thickness of the printed traces are smaller, resulting in a higher resistance R . The thickness of the sensor is with $h=54 \mu\text{m}$ much smaller than that in version 1.

The main error of this sensor design is the trough hole which represents an error source of the sensor. With the resistivity R the conductivity between the two sides can be inspected. Abrupt rise of the resistance R , means a connection

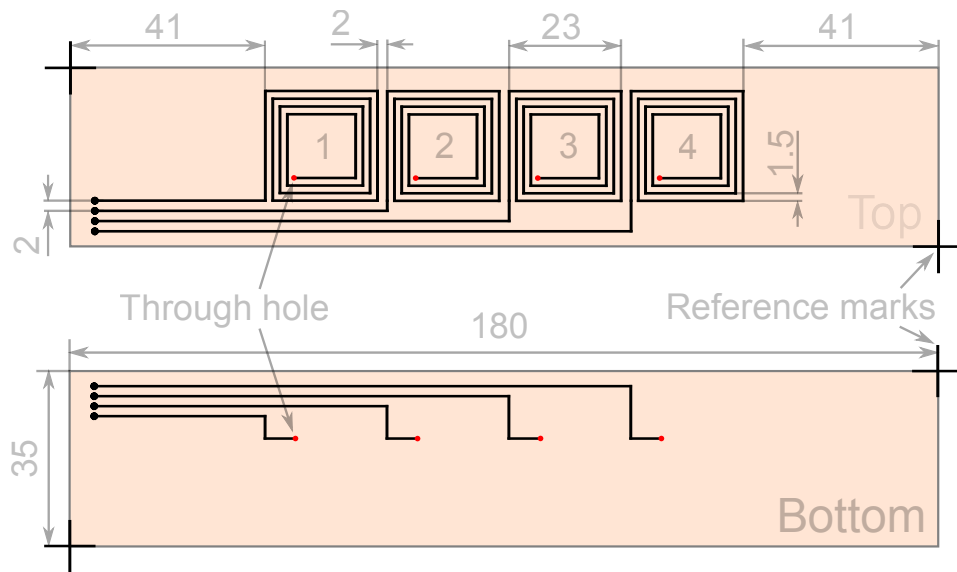


Figure 4.6.: Dimensions of version 2 of the magnetic sensor.

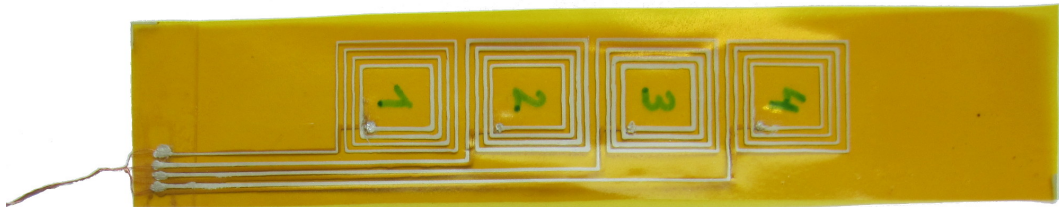


Figure 4.7.: Picture of the manufactured sensor.

sensor No.:	length a [mm]	thickness h [μm]	area A_{eff} [cm^2]	rel. error f [%]	resistance R [Ω]
1	23	54	13.9 ± 0.5	-1.2	118
2			13.5 ± 0.5	-4.2	124
3			13.9 ± 0.4	-1.7	198
4			14.0 ± 0.3	-0.5	197

Table 4.3.: Summary of the characteristics of the sensor version 2.

problem. In future, the thickness h of the sensor can be even more reduced. For example, with the self-made reactive silver ink the thickness of the traces is much smaller. Also the protection layer is not necessary in some cases. In a new generation of the sensor, it should be possible to reduce the thickness of the sensor under $h=30\text{ }\mu\text{m}$.

However, we should say that this sensor is one of the thinnest sensor, and one of the simplest in manufacture. With the sensor more than 200 measurements in a transformer core interior were carried out, and it had not been damaged.

5. Applications of the Manufactured Sensors

The last sections described the manufacturing of the search coil sensor to measure the off-plane flux density B_z . This chapter describes the applications of the manufactured sensor. The measurements are carried out on a three-phase model transformer core which is available at our institute. At first, the transformer core and the measurement setup will be discussed in general. The next section tests the repeatability of the four search coils of the sensor version 2. The latest and thinnest version of the sensor is compared with version 1, and a conventional search coil sensor. The last section describes the influence of the sensor thickness h and inter-laminar air-gap g , respectively. A empirical model will be presented which describes the performed measurements.

5.1. Transformer Core

To study practical relevant transformer cores in laboratory conditions, model cores are necessary. In our laboratory a model transformer core was manufactured as a part of a FFG-project (BRIDGE Project 3-D Core Loss, No.:834159) [43]. This core consists of 188 layered iron sheets. These sheets are made of CGO-material (C130-30, Thyssen Krupp), and each sheet is 300 μm thick and has a 2 μm to 5 μm thick dialectic phosphate coating.

In comparison to rotational machines where the construction needs isotropic, NO (non-oriented) materials [44], in transformer cores CGO or HGO-materials are used. These materials have a high magnetic anisotropy. The grain orientation is determined by the RD (rolling direction) of the sheet. The anisotropy influences the magnetizability and the remagnetizing losses of the core [45]. In RD the relative permeability μ_r shows the highest values. In comparison to the RD, the TD (transverse direction) is orthogonal to the RD, it shows the lowest values of the relative permeability μ_r .

The main characteristics of the core material for a nominal magnetization $\hat{B}=1.7$ T and frequency $f=50$ Hz are: specific total loss $P_S=1.2$ W/kg and a relative permeability $\mu_r=12620$. Fig.5.1 shows the three-phase model transformer core at our institute. The cross-section of the core shows the package design. Also the self-made off-plane flux density sensor is visible in the lower, left corner of the core. The sensor is placed in the middle of peripheral package P_3 , of the corner section. The core consist of three packages [46]:

1. P_1 : main package of 100 mm width and 30 mm height, 25x4 sheets,
2. P_2 : outer package of 70 mm width and 17 mm height, 15x4 sheets,
3. P_3 : peripheral package of 50 mm width and 8 mm height, 7x4 sheets.

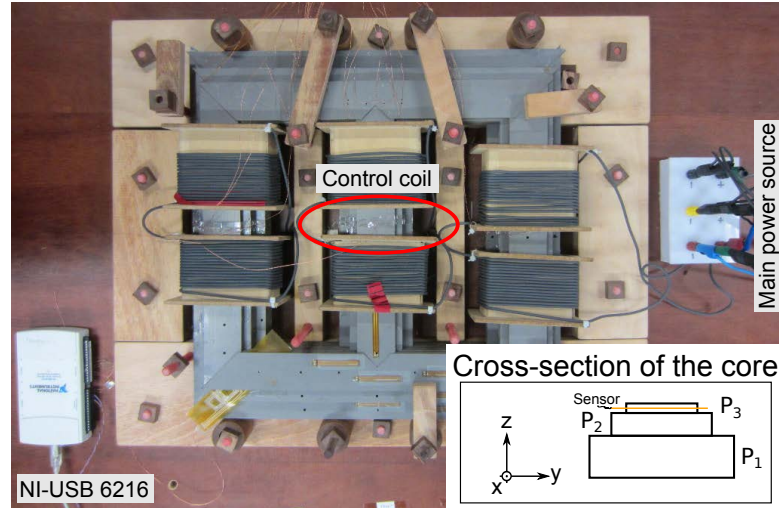


Figure 5.1.: Picture of the three-phase transformer core. The sensor is in the middle of package P_3 . The cross-section shows the package design of the core.

The primary magnetizing coil has $N=33$ turns, and it is mounted in the center of each leg. These coils cover the legs partially in contrast to magnetizing coils in the praxis. This makes measurements at the corner section accessible. Also the magnetic stray flux Φ_S from the ends of the magnetizing coils is reduced in this assembly. Therefore, the sensitivity for small values of B_z inside the core is higher. The used model core has no secondary coils, because only the magnetic properties of the core are interesting.

The model transformer was driven by an adjustable transformer (TIDMT/AGG, Ruhstrat) as a main power unit with a nominal capacity of 25 KVA. The power of the adjustable transformer was controlled by a wattmeter (NORMA 4000). The input current measuring range of 10 A is enhanced up to 300 A through external shunts. To avoid inrush current, which occur at each switch-on cycle of inductive loads, an easy and cost-effective solution is realized. For that reason, at the switch-on cycle, the transformer coils are switched in series with a NTC (negative temperature coefficient) thermistor (B57237, Epcos). These thermistors serve as inrush current limiter, after a delay time of 300 ms the thermistors are shorted-out by a relay contact. The model transformer was driven by the adjustable transformer with a frequency of $f=50$ Hz and different nominal magnetization of $\hat{B}=1.5$ T, $\hat{B}=1.7$ T, and $\hat{B}=1.8$ T. For the adjustment of the required nominal magnetization \hat{B} , a control coil with $N=1$ turn, is wound on the middle limb of the core. The control coil detect the voltage $u(t)$ which is correlated to the nominal magnetization \hat{B} . The

5.2. Results

As described in section 4.2.4, sensor version 2 consists of an array of four search coils. With these four search coils, it was possible to measure the off-plane flux density B_z inside a transformer core at four position simultaneously. Fig.5.3 and 5.1 shows the measuring position P inside the core. The sensor is placed in the middle of peripheral package P_3 , of the lower, left, corner section.

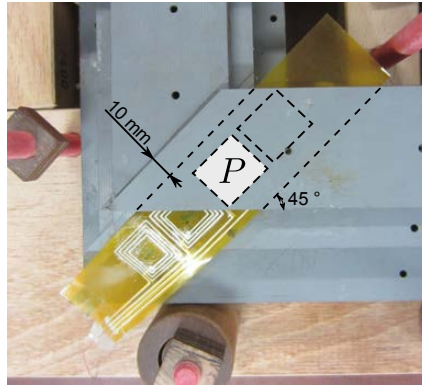


Figure 5.3.: Sensor position P for the measurements of B_z inside the transformer core.

5.2.1. Repeatability of the Sensor Search Coils

This section describes the repeatability of the measurement of the four search coils. The measurements are carried out with a nominal magnetization of $\hat{B}=1.5$ T, $\hat{B}=1.7$ T, and $\hat{B}=1.8$ T. Fig.5.4 shows typical results for the measuring point P . The regional off-plane induction B_z is given as a function of time t (left), and the higher harmonics of the measurement (right), for the four sensors #1...#4. The higher harmonics represents a Fourier analysis of the measurement. The analysis is implemented in the self-programmed LabView application.

At a relative high nominal magnetization of $\hat{B}=1.8$ T, the magnetic off-plane flux density B_z is almost sinusoidal. It is visible that the signal waveforms of all four search coils are similar. Also the higher harmonics from the Fourier analysis are in the same range. With decreasing of \hat{B} , the sinusoidal waveform disappears.

The higher harmonics can be interpreted as a strong distortion of the flux. As described in section 5.2.3, the distortion in the corner section comes from the stacked laminations of the core. Also the inter-laminar air-gap g affect the distortion of the flux. The magnetic stray flux density B_S has also an essential impact of the generation of the higher harmonics. B_S affects the measurements for lower \hat{B} more, as for higher \hat{B} . Also the nonlinear characteristics of the ferromagnetic material affects the sinusoidal waveform. However, the signal waveforms of all four search coils are similar, and this ensures the effectiveness of the self-printed magnetic sensors.

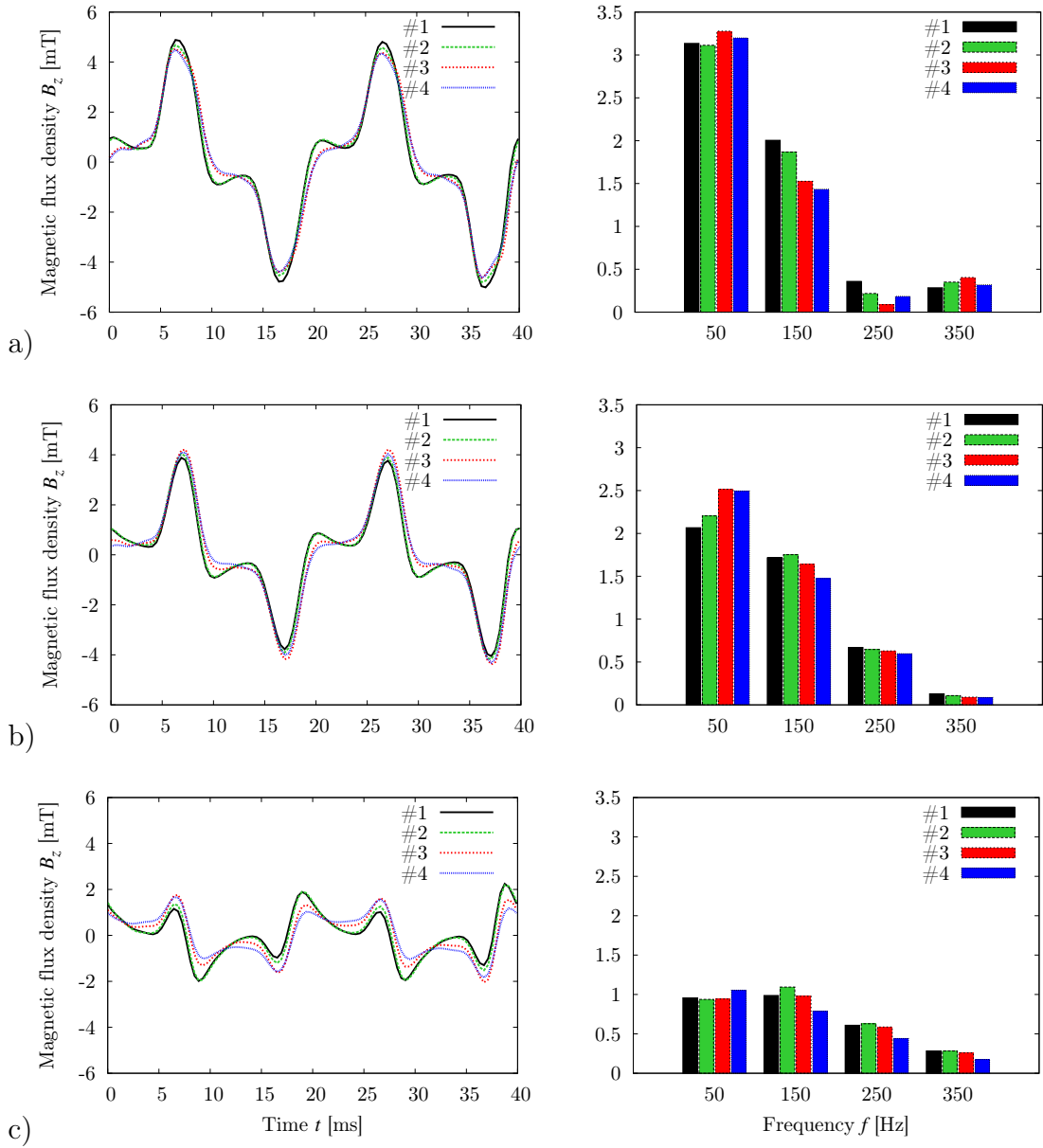


Figure 5.4.: Typical results for the measuring point P . The regional off-plane induction B_z is given as a function of time t (left), and higher harmonics of the measurement (right), for the four sensors #1...#4. a) Nominal magnetization $\hat{B} = 1.8$ T. b) $\hat{B} = 1.7$ T. c) $\hat{B} = 1.5$ T.

5.2.2. Comparison of Different Sensors

The last section showed the effectiveness, and the repeatability of the search coils from the sensor. In this section, a comparison of the latest sensor version 2 (sensor thickness $h=54\text{ }\mu\text{m}$), version 1 ($h=187\text{ }\mu\text{m}$), and a copper wire search coil ($h=250\text{ }\mu\text{m}$) from a former work [10] is shown. For that reason, each sensor was placed in the same position P as before and the measurements with a nominal magnetization of the core of $\hat{B}=1.5\text{ T}$, $\hat{B}=1.7\text{ T}$, and $\hat{B}=1.8\text{ T}$ were carried out. The sensitivity of the copper wire search coil was much lower than the sensitivity of the printed search coils, due to the much lower cross-sectional area. Fig.5.5 shows the maximum amplitude of B_z measured with the different sensors, for different nominal magnetizations of the core.

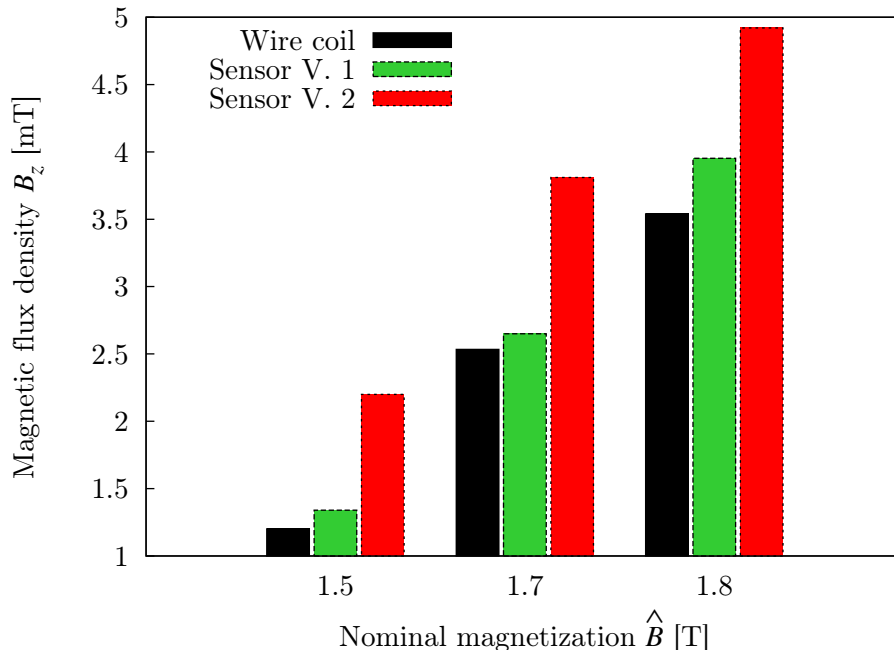


Figure 5.5.: Amplitude of the magnetic flux density B_z , measured with different sensors. The thickness h of the sensor influenced the measurement. Thickness of the sensors: wire coil $h=250\text{ }\mu\text{m}$, V. 1 $h=186\text{ }\mu\text{m}$, V. 2 $h=54\text{ }\mu\text{m}$

It is visible that the thinnest sensor measures the highest B_z . This means that a correlation between the maximum amplitude of the off-plane flux density B_z and the sensor thickness h , regarding the inter-laminar air-gap g , exist. This result was the motivation for further investigations of the inter-laminar air-gap g , and how the gap affects B_z .

5.2.3. Influence of the Sensor Thickness

The last sections described a difference in the measurements of the off-plane flux density B_z with sensors of different thicknesses h . Already in section 1.1, the influence of the inter-laminar air-gap g on B_z was discussed. This discussion was the main motivation to manufacture thin-film magnetic sensors. This section should determine the influence of the inter-laminar air-gap g on B_z . For that reason, the thinnest sensor (Version 2) is placed in the same position P as in the sections above. An increasing of the inter-laminar air-gap g is accomplished with different 25 μm thin Kapton foils, placed underneath the sensor. Fig.5.6 illustrate the amplitude of B_z as a function of the inter-laminar air-gap g and different nominal magnetizations \hat{B} .

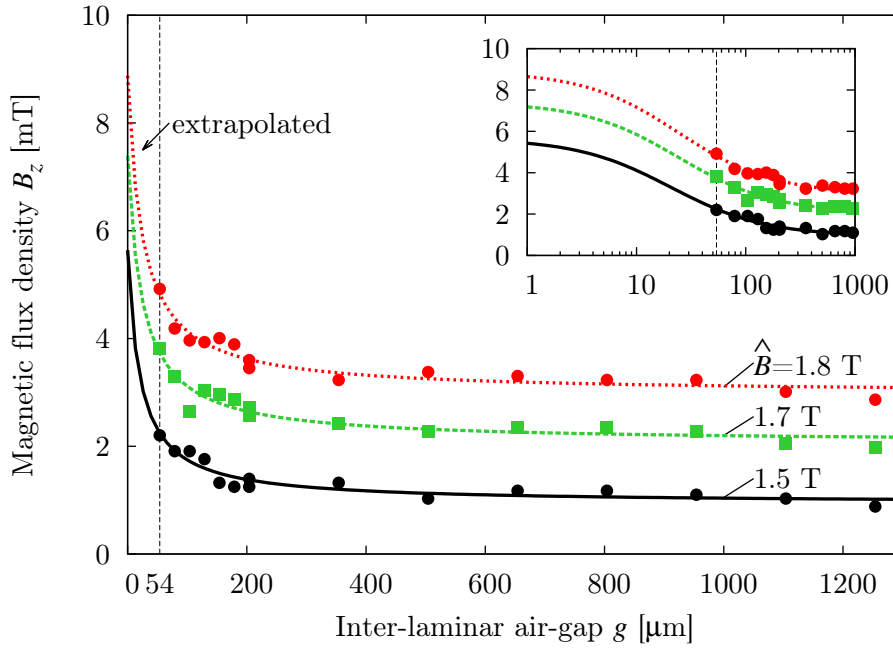


Figure 5.6.: Amplitude of the magnetic flux density B_z at different inter-laminar air-gaps g . The continuous lines shows the fit of the model, according to Eq.5.3. Nominal magnetization of the core of $\hat{B}=1.5$ T, $\hat{B}=1.7$ T, and $\hat{B}=1.8$ T, measured in the middle limb.

The results show that B_z distinctly increases for air gaps g below 150 μm . For gaps bigger than 150 μm , B_z sinks very slightly in a almost linear way. It means that with our new sensor of 54 μm thickness, we can measure much accurately the z-induction than the conventional wire sensor of 250 μm thickness [10]. According to Fig.5.6, they detect lower amplitudes than the real values.

Based on the measurement results, we obtain a empirically-derive equation

$$B_z(\hat{B}, g) = \frac{C_1(\hat{B})}{g + C_2(\hat{B})} + C_3(\hat{B}) \quad . \quad (5.3)$$

The coefficients C_1 , C_2 , and C_3 are constants for a particular nominal magnetization \hat{B} . The coefficients C_1 and C_2 are proportional to the excitation of the

transformer core. On the other side, the coefficient C_3 represents the density of the existing stray flux. C_1 , C_2 , and C_3 increase with raising of \hat{B} (compare Fig.5.6).

As a major conclusion, the sensor is still too thick to avoid influences of the inter-laminar air-gap g . Fig.5.6 indicates that the results for B_z in the core, as reported in literature are not relevant for practice due to high sensor thicknesses of $250\text{ }\mu\text{m}$ [10]. Even in the here given case, the result is about 60 % below the intensity of B_z for $\hat{B}=1.5\text{ T}$, as indicated from extrapolation. Fig.5.7 shows the relative deviation f of the extrapolated value $B_z(\hat{B}, 0)$ and the measured value $B_z(\hat{B}, 54)$ as a function of \hat{B} , according to

$$f(\hat{B}) = \left(\frac{B_z(\hat{B}, 54)}{B_z(\hat{B}, 0)} - 1 \right) \cdot 100 \% \quad . \quad (5.4)$$

The relative deviation f decrease with a higher nominal magnetization \hat{B} . With this relation, the real values of B_z can be estimated.

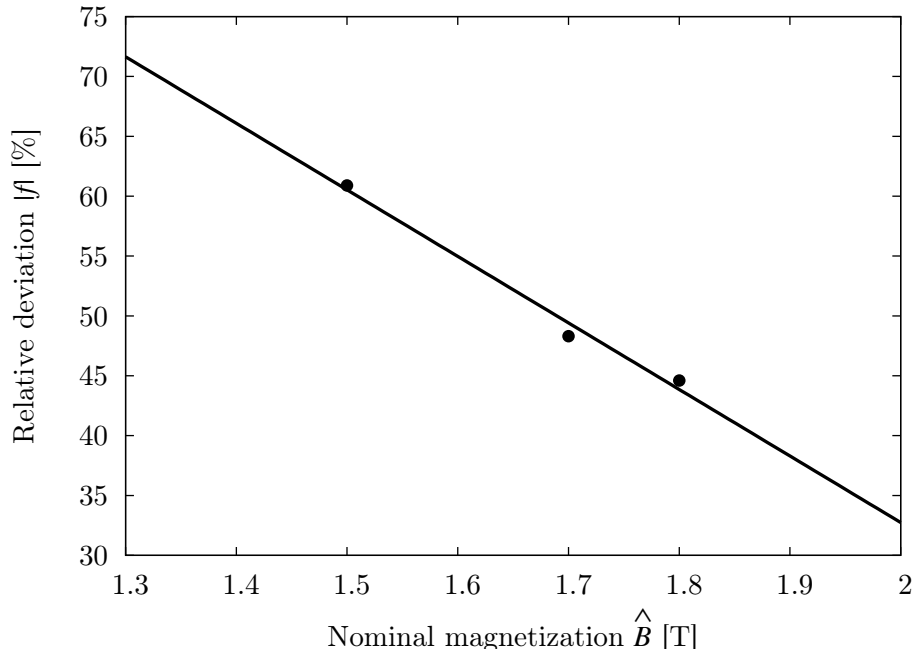


Figure 5.7.: Relative deviation f as a function of the nominal magnetization \hat{B} .

6. Summary & Outlook

This thesis presents a pilot study for the manufacturing of thin-film sensors for magnetic induction measurements. In particular, the aim of the study was to print an ultra-thin sensor for detection of the off-plane flux density B_z inside a transformer core. An accurate measurement of B_z is of a great interest since it has a big impact on losses, magnetostriction, and audible noise, respectively. Since more than 40 years, measurements have been described. However, all these measurements are time-consuming and expensive. Another problem is the influence of the sensor thickness of typically at least 200 μm on the resulted measurement.

The resulting inter-laminar air-gap between the laminations tends to yield significant decreases of B_z . For that reason, the basic idea of the project was to develop completely new magnetic thin-film sensors for the measurement of B_z . They had to be cheap, easy in manufacturing, resistant for the hard conditions between the laminations inside the core, and last but not least thin enough to yield results that can be corrected by extrapolation.

The initial plan of the project was to use a 3D print procedure for both:

- non-conducting sensor component that are needed e.g. for insulation or for mechanical mounting of components, and
- electrically conducting components e.g. for sensors of wiring purposes.

However, intensive attempts indicated that it is extremely difficult to develop conductive 3D print materials, as also indicated by the fact that commercial materials have very weak conductivity, so far. Another issue is the difficulty to produce thin-film layers by 3D print. The mechanical properties, such as bending stiffness, of the used ABS material were insufficient, as well. This experience, gained from pre-tests, was the reason to change the procedure. As a next step, we combined a commercial 3D printer with a 2D dispensing system for conductive ink materials which tend to be less problematically, apart from the advantage that ensure very thin print layers.

On the extruder unit of the 3D printer, a 2D printer setup was mounted. This system is pressure driven by a high precision linear stepper motor. Own hardware and software were developed to control the dispensing system. This was a difficult part of the work, since the available 3D printer is a proprietary system. Therefore, reverse engineering was necessary to control the 2D printer setup with the 3D printer software. With calibration procedures and parameter studies the optimum printing parameters were found. Furthermore, by means of FEM simulations some error sources were found. In our future work, these error sources can be taken into account by manufacturing of combined 3D/2D printed sensors.

As substrate materials for the 2D print, PET and Kapton were investigated. Kapton was with a thickness of 25 μm , and the excellent mechanical properties the first choice for the sensor manufacturing. Several silver inks were tested to find the best ratio between: price, availability, electrical/mechanical properties, and printing results.

With the gained experience from all these building alterations, investigations of printing substrates and inks, the sensor manufacturing was started. A final sensor with an overall thickness of just 50 μm was manufactured. With a calibration procedure, the effective cross-sectional area of the search coil was measured. The sensor consists of an array of four search coils enabling B_z measurement on four position at the same time.

The sensor was tested in the interior of a three-phase model transformer core. The core consists of three different packages, and the sheets were made of conventional grain oriented electrical steel. With an adjustable transformer, different nominal magnetizations \hat{B} of the model core were possible. To test the repeatability of the search coils, all search coils were arranged in the same position, and the measurements were carried out at the same \hat{B} . All four search coils showed similar waveforms. For higher \hat{B} the waveform proved to be almost sinusoidal. However, higher harmonics were registered as well. At next, three different sensors for B_z measurements were compared. These three sensors have different thicknesses h . As expected, the thicker sensors showed lower maximum amplitudes of B_z . At last, the sensor thickness h and the inter-laminar air-gap g , respectively, were investigated. For that reason, an empirical model, based on the measurements of B_z as a function of g was developed.

Extrapolation of the sensor thickness shows that the 50 μm sensor is still too thick to avoid decreases of local B_z . For $\hat{B}=1.5$ T, a relative deviation between the extrapolated value and the measured value is more than 60 %. However, attempts indicate that extrapolation is possible for approximate correction of the deviation. The results indicate that the reported values of B_z in the literature are not relevant for practice due the high sensor thickness of at least 200 μm .

As a conclusion, this work yielded the basic methodologies for the establishment of sensors through combined 3D/2D printing procedure. For better results, the following proposals are found:

- Instead of a proprietary low-budget 3D printer, the whole setup should be installed in the XYZ scanning chamber of the institute. This enables full control over the system.
- The piston dispensing system is error-prone. An air-pressure based dispensing system would show better dispensing capabilities, as well as easier possibilities of control.
- With additional investigations, the self-made reactive silver ink could be improved even further. In our future work, attempts should be made to decrease the surface tension of the substrate.

-
- Investigations of thinner substrate materials could yield decreased overall sensor thickness.

A. Appendix

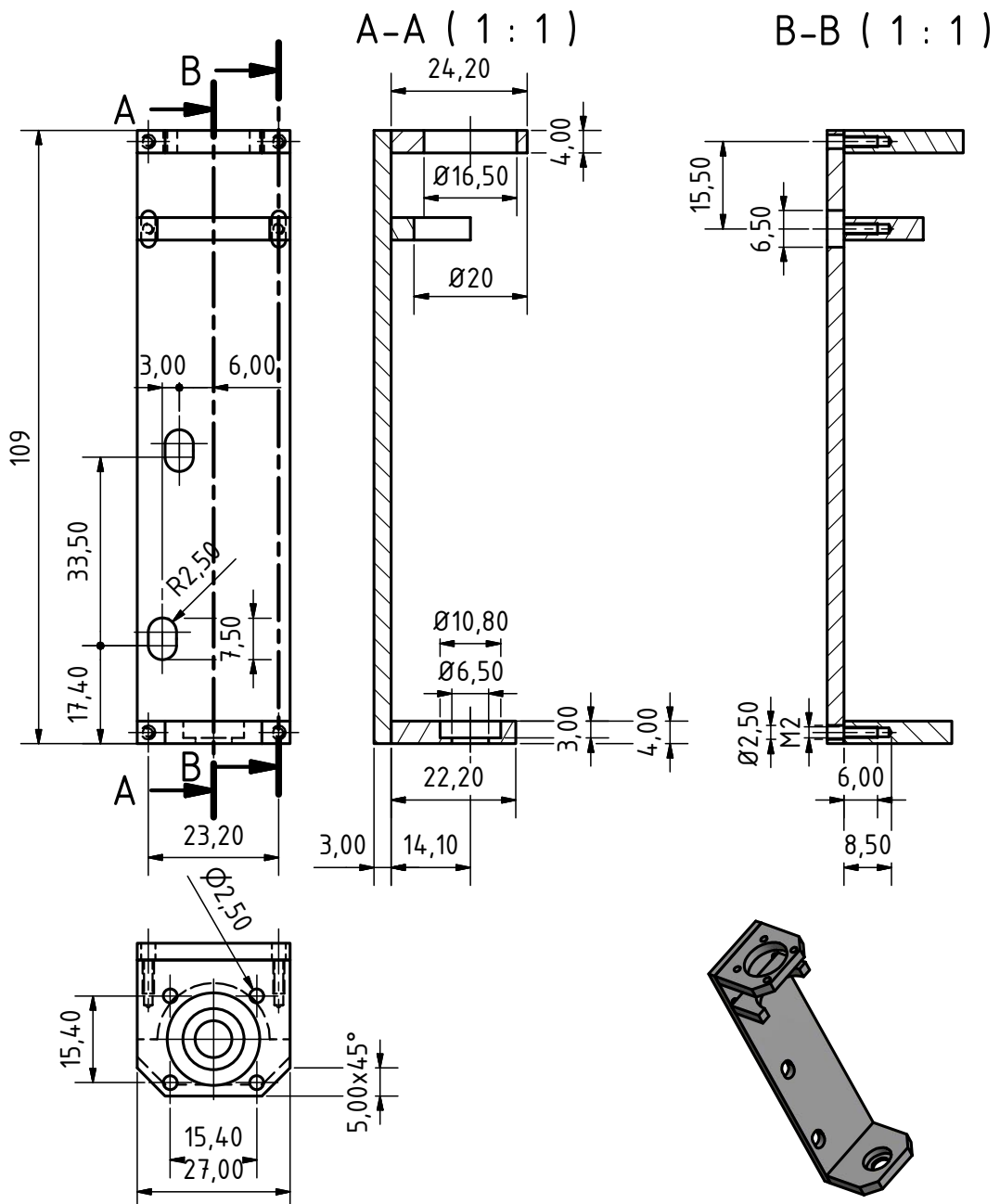


Figure A.1.: Drawing of the holder for the cartridge and linear stepper motor.

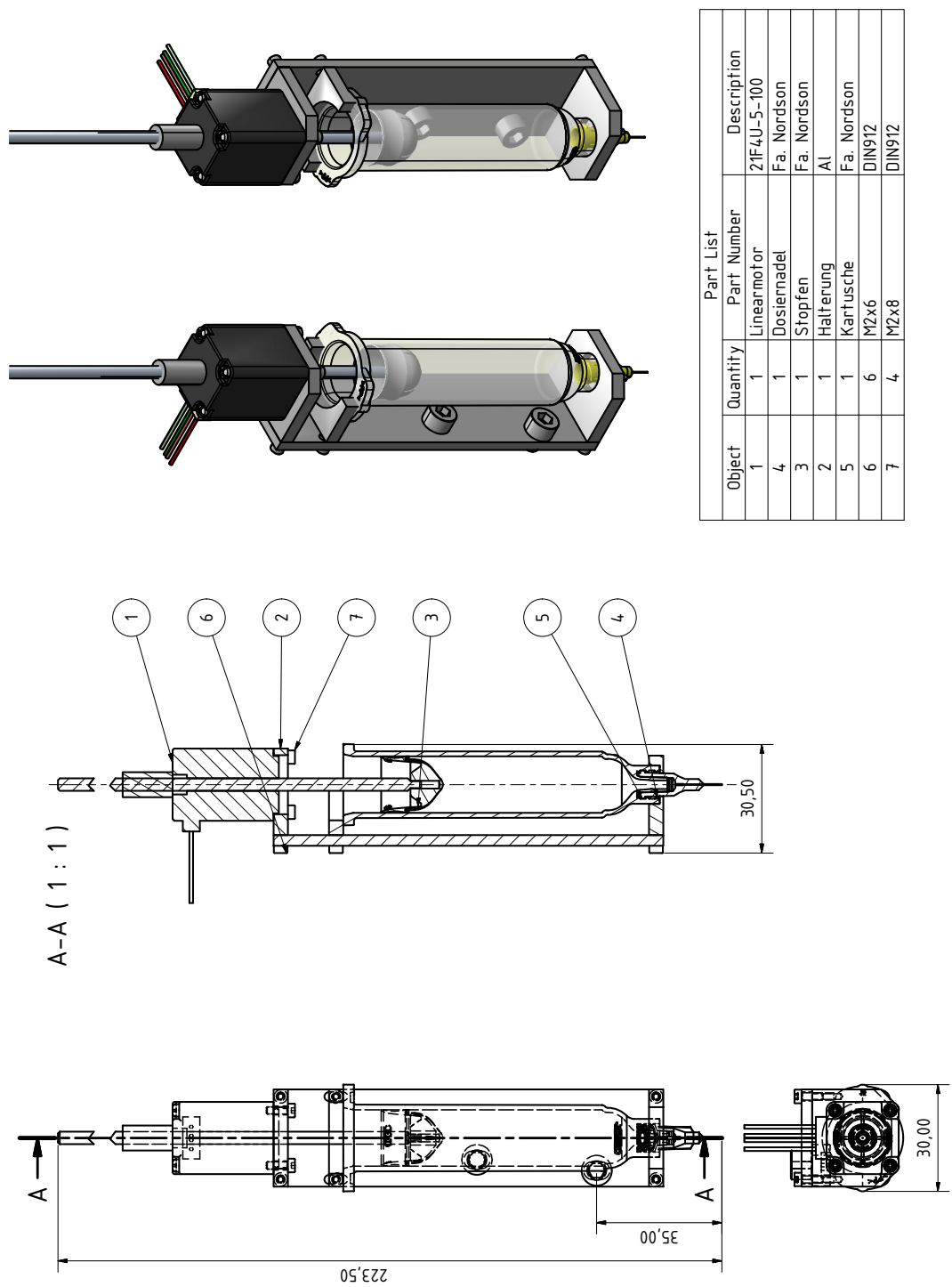


Figure A.2.: Assembly drawing of the piston dosing system.

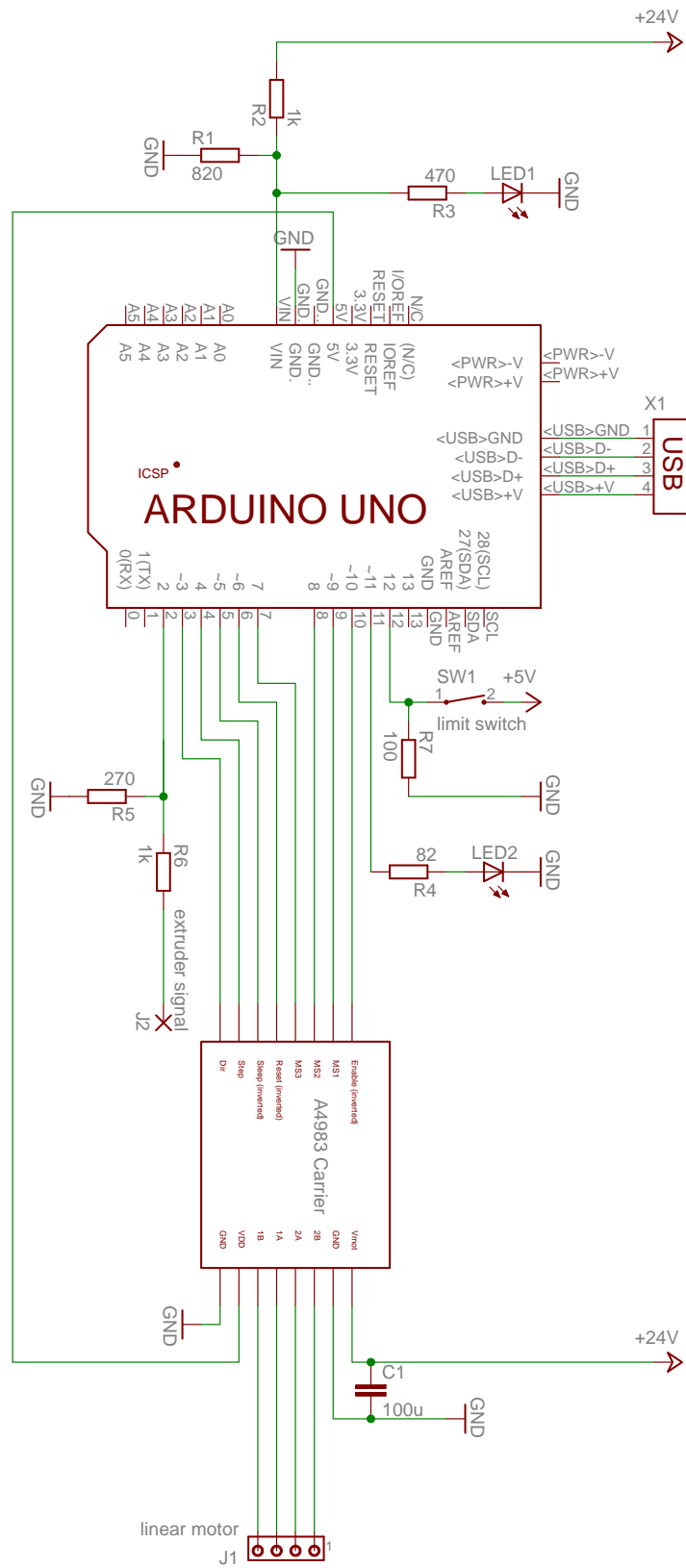


Figure A.3.: Wiring diagram of the control board for the 2D print setup.

Listing A.1: Arduino UNU program to controll the linear stepper motor.

```

1  /*
2  ARDUINO UNO program to control the 2D-printing setup fn the
3  FabbsterG 3D-printer.
4
5  -Control a DMOS A4988 microstepping driver for the linear stepper motor.
6  -Trigger signal comes from the extruder motor.
7  -End switch to protect the cartridge and the setup.
8  -Change the speed of the linear stepper motor with the serial interface.
9
10 Version: 1; 29.04.2014
11
12 Program developed by:
13 Christian Huber
14 E-Mail: christian.huber@tuwien.ac.at
15 Technical University of Vienna
16 Institute of Electrodynamics, Microwave and Circuit Engineering
17 */
18
19 // Motor control
20 #define dirPin 3
21 #define stepPin 4
22 #define sleep 5
23 #define reset 6
24 #define MicroStep3Pin 7
25 #define MicroStep2Pin 8
26 #define MicroStep1Pin 9
27 #define enablePin 10
28
29 // Trigger
30 #define trigger 2
31 #define led 11
32
33 // End position
34 #define button 12
35
36 #define stepPulseWidthInMicroSec 2
37 #define setupTimeInMicroSec 1
38
39 // Time between two steps (controlled by serial interface)
40 int timeBetweenStepsInMilliSec = 880;
41 // Int-string consist of 5 digits, end of the string is a 0
42 const int MaxChars = 5;
43 // Have to be big enough for the number + 0
44 char strValue[MaxChars+1];
45 // Array-Index to save the incomming value
46 int index = 0;
47
48 long startTime;
49 // Real time between two steps
50 long duration;
51
52 // Find the last step
53 boolean ifOn = false;
54 boolean currentDirection = false;
55 int buttonEvent = 0;
56 int triggerEvent = 0;
57 long k = 0;
58 long kMax = 0;
59 // Count the steps
60 int vol = 0;
61
62 // Read the int-value from the serial interface
63 int readSerial() {
64     if( Serial.available() ) {
65         char ch = Serial.read();
66         if( index < MaxChars && isDigit(ch) ) {
67             // ASCII-character insert to string
68             strValue[index++] = ch;
69         }

```

```

70     else {
71         // Buffer full or first not digit
72         // Close the string with a 0
73         strValue[index] = 0;
74         // convert the string with atoi in a int-value
75         timeBetweenStepsInMilliSec = atoi(strValue);
76         index = 0;
77     }
78 }
79 return timeBetweenStepsInMilliSec;
80 }
81
82 void setCurrentDirection(boolean dir) {
83     if(dir == false) {
84         digitalWrite(dirPin, LOW);
85     } else {
86         digitalWrite(dirPin, HIGH);
87     }
88     currentDirection = dir;
89     delayMicroseconds(setupTimeInMicroSec);
90 }
91
92 void changeDirection() {
93     setCurrentDirection(!currentDirection);
94 }
95
96 void enableStepper(int isEnabled) {
97     if(isEnabled) {
98         // enable LOW = stepper driver ON
99         digitalWrite(enablePin, LOW);
100     } else {
101         // enable HIGH = stepper driver OFF
102         digitalWrite(enablePin, HIGH);
103     }
104     delayMicroseconds(setupTimeInMicroSec);
105 }
106
107 void takeSingleStep() {
108     digitalWrite(stepPin, LOW);
109     delayMicroseconds(stepPulseWidthInMicroSec);
110     digitalWrite(stepPin, HIGH);
111     delayMicroseconds(stepPulseWidthInMicroSec);
112     digitalWrite(stepPin, LOW);
113 }
114
115 // 1.8 degrees per full step or 200 full steps per revolution
116 void setFullStep() {
117     digitalWrite(MicroStep1Pin, LOW);
118     digitalWrite(MicroStep2Pin, LOW);
119     digitalWrite(MicroStep3Pin, LOW);
120     delayMicroseconds(setupTimeInMicroSec);
121 }
122
123 void setHalfStep() {
124     digitalWrite(MicroStep1Pin, HIGH);
125     digitalWrite(MicroStep2Pin, LOW);
126     digitalWrite(MicroStep3Pin, LOW);
127     delayMicroseconds(setupTimeInMicroSec);
128 }
129
130 void setQuarterStep() {
131     digitalWrite(MicroStep1Pin, LOW);
132     digitalWrite(MicroStep2Pin, HIGH);
133     digitalWrite(MicroStep3Pin, LOW);
134     delayMicroseconds(setupTimeInMicroSec);
135 }
136
137 void setEighthStep() {
138     digitalWrite(MicroStep1Pin, HIGH);
139     digitalWrite(MicroStep2Pin, HIGH);

```

```

140     digitalWrite(MicroStep3Pin, LOW);
141     delayMicroseconds(setupTimeInMicroSec);
142 }
143
144 void setSixteenthStep() {
145     digitalWrite(MicroStep1Pin, HIGH);
146     digitalWrite(MicroStep2Pin, HIGH);
147     digitalWrite(MicroStep3Pin, HIGH);
148     delayMicroseconds(setupTimeInMicroSec);
149 }
150
151 void setup() {
152     // Baudrate
153     Serial.begin(9600);
154
155     // Set the enable pin to be an output
156     pinMode(enablePin, OUTPUT);
157     pinMode(stepPin, OUTPUT);
158     pinMode(dirPin, OUTPUT);
159     pinMode(sleep, OUTPUT);
160     pinMode(reset, OUTPUT);
161
162     pinMode(MicroStep1Pin, OUTPUT);
163     pinMode(MicroStep2Pin, OUTPUT);
164     pinMode(MicroStep3Pin, OUTPUT);
165
166     pinMode(led, OUTPUT);
167
168     pinMode(trigger, INPUT);
169     digitalWrite(trigger, HIGH);
170
171     pinMode(button, INPUT);
172     digitalWrite(button, HIGH);
173
174     // Inverted pins
175     digitalWrite(sleep, HIGH);
176     digitalWrite(reset, HIGH);
177
178     // Microstepping mode
179     setFullStep();
180     // Enable motor
181     enableStepper(true);
182     // In a clockwise direction
183     setCurrentDirection(true);
184 }
185
186 void loop() {
187     // Read the value from the serial interface
188     timeBetweenStepsInMilliSec = readSerial();
189
190     // Limit switch
191     buttonEvent = digitalRead(button);
192
193     // Read i-times the trigger event and summate it j-times and return
194     // the highest value kMax
195     kMax = 0;
196     for (int j = 0; j <= 70; j++) {
197         k = 0;
198         for (int i = 0; i <= 200; i++) {
199             triggerEvent = digitalRead(trigger);
200             if (triggerEvent == HIGH) {
201                 k++;
202             }
203         }
204         if (kMax < k) {
205             kMax = k;
206         }
207     }
208
209     if (kMax > 53 && buttonEvent == LOW) {

```

```
210     digitalWrite(led, HIGH);
211     enableStepper(true);
212     if (vol == 0) {
213         for (int j = 0; j <= 10; j++) {
214             takeSingleStep();
215             delay(1);
216         }
217     }
218     takeSingleStep();
219     delay(timeBetweenStepsInMilliSec);
220     ifOn = true;
221     vol++;
222 }
223
224 else {
225     // After the last step change direction and take 10 steps
226     if (ifOn == true) {
227         changeDirection();
228         for (int j = 0; j <= 10; j++) {
229             takeSingleStep();
230             delay(1);
231         }
232         changeDirection();
233         Serial.println("Volume_flow_["nl/s]:");
234         // Volume flow [nl/s]
235         Serial.println(387.8/(timeBetweenStepsInMilliSec + 68)/0.001);
236         Serial.println("Volume_["nl]:");
237         // Volume for the print nl]
238         Serial.println(vol*387.8);
239         Serial.println("-----");
240     }
241     enableStepper(false);
242     digitalWrite(led, LOW);
243     ifOn = false;
244     vol = 0;
245 }
246 }
```

Listing A.2: Python script to create G-code commands for the FabbsterG 3D printer

```

1  # -*- coding: utf-8 -*-
2  """
3  G-Code Generator for FabbsterG 3D-Printer
4
5  Version: 1; 24.06.2014
6
7  Program developed by:
8  Christian Huber
9  E-Mail: christian.huber@tuwien.ac.at
10 Technical University of Vienna
11 Institute of Electrodynamics, Microwave and Circuit Engineering
12 """
13 import sys
14 import numpy as np
15 import matplotlib.pyplot as plt
16 from matplotlib.path import Path
17 import matplotlib.patches as patches
18
19 ##### INPUT #####
20 file_out = "line_4cm.gcd" # Filename
21 plot = True # Plot the patterns
22 #####
23
24 # Functions
25 #####
26 # SquareSensor (offset x, offset y, offset z, length, Number of turns,
27 # Pitch)
28 def Square(x, y, z, a, n, s):
29     for j in range(2*n):
30         if j == 0:
31             x,y,z = Line(x, y, z, x-a+s, y)
32             x,y,z = Line(x, y, z, x, y+a)
33         elif j % 2 == 0:
34             x,y,z = Line(x, y, z, x-a+j*s, y)
35             x,y,z = Line(x, y, z, x, y+a-j*s)
36         else:
37             x,y,z = Line(x, y, z, x+a-j*s, y)
38             x,y,z = Line(x, y, z, x, y-a+j*s)
39     data.write('G1X' + str(x) + 'Y' + str(y) + 'Z' + str(20) +
40               'F100\n')
41     return x, y, z
42
43 # ArchimedeanSpiral(offset x, offset y, offset z, start angle,
44 # end angle, a=r/phi)
45 def ArchSpiral(x, y, z, start, length, a):
46     x_offset = np.array([x,y,z]) # Offset
47     step = 0.001
48     step_back = 0.0002
49
50     x = np.array([0.,0.,0.])
51     x += x_offset
52     data.write('G1X' + str(x[0]) + 'Y' + str(x[1]) +
53               'Z' + str(x[2]) + 'F1\n')
54     data.write('M108S500\n') # Extruder speed [RPM]
55     for i in np.arange(start, length, step):
56         for k in range(0, 1):
57             x[0] = a*i*np.cos(i)
58             x[1] = a*i*np.sin(i)
59             x[2] = 0
60             x += x_offset
61             data.write('G1X' + str(x[0]) + 'Y' + str(x[1]) +
62                       'Z' + str(x[2]) + 'F1\n')
63
64             i_back = i - step_back
65             x[0] = a*i_back*np.cos(i_back)
66             x[1] = a*i_back*np.sin(i_back)
67             x[2] = 0

```



```

68         x += x_offset
69         data.write('G1_X' + str(x[0]) + 'Y' + str(x[1]) +
70                 'Z' + str(x[2]) + 'F1\n')
71         plot_x.append([x[0], x[1]])
72         plot_x.append('--')
73         data.write('M108_S0\n') # Extruder speed [RPM]
74         return x[0], x[1], x[2]
75
76 # Circle(offset x, offset y, offset z, radius)
77 def Circle(x, y, z, r):
78     xx=x
79     x_offset = np.array([x,y,z]) # Offset
80     step = 0.001
81     step_back = 0.0005
82
83     x = np.array([0.,0.,0.])
84     x += x_offset
85     data.write('G1_X' + str(x[0]) + 'Y' + str(x[1]) +
86             'Z' + str(x[2]) + 'F1\n')
87     data.write('M108_S500\n') # Extruder speed [RPM]
88     for i in np.arange(0, 4*np.pi, step):
89         for k in range(0, 1):
90             x[0] = r*np.cos(i)
91             x[1] = r*np.sin(i)
92             x[2] = 0
93             x += x_offset
94             data.write('G1_X' + str(x[0]) + 'Y' + str(x[1]) +
95                     'Z' + str(x[2]) + 'F1\n')
96
97             i_back = i - step_back
98             x[0] = r*np.cos(i_back)
99             x[1] = r*np.sin(i_back)
100            x[2] = 0
101            x += x_offset
102            data.write('G1_X' + str(x[0]) + 'Y' + str(x[1]) +
103                    'Z' + str(x[2]) + 'F1\n')
104            plot_x.append([x[0], x[1]])
105            plot_x.append('--')
106            data.write('M108_S0\n') # Extruder speed [RPM]
107            return xx, y, z
108
109 # Line(offset x, offset y, offset z, end position x, end position y)
110 def Line(x, y, z, end_x, end_y):
111     #####INPUT#####
112     x_offset = np.array([x,y,z]) # Offset
113     length_x = x - end_x
114     length_y = y - end_y
115     step = 0.1
116     #step_back = 0.025
117     step_back = 0.06
118     x = np.array([0.,0.,0.])
119     x += x_offset
120
121     data.write('G1_X' + str(x[0]) + 'Y' + str(x[1]) +
122             'Z' + str(x[2]) + 'F1\n')
123     data.write('M108_S500\n') # Extruder speed [RPM]
124
125     if length_x != 0:
126         factor = abs(length_y/length_x)
127         length_x /= (step - step_back)
128         for i in range(0, int(abs(length_x))):
129             for k in range(0, 1):
130                 if length_x <= 0 and length_y <= 0:
131                     x[0] += step
132                     x[1] += step*factor
133                     data.write('G1_X' + str(x[0]) + 'Y' + str(x[1]) +
134                             'Z' + str(x[2]) + 'F1\n')
135                     x[0] -= step_back
136                     x[1] -= step_back*factor

```

```

138         data.write('G1_X' + str(x[0]) + 'Y' + str(x[1]) +
139                    'Z' + str(x[2]) + 'F1\n')
140     elif length_x >= 0 and length_y >= 0:
141         x[0] -= step
142         x[1] -= step*factor
143         data.write('G1_X' + str(x[0]) + 'Y' + str(x[1]) +
144                    'Z' + str(x[2]) + 'F1\n')
145         x[0] += step_back
146         x[1] += step_back*factor
147         data.write('G1_X' + str(x[0]) + 'Y' + str(x[1]) +
148                    'Z' + str(x[2]) + 'F1\n')
149     elif length_x <= 0 and length_y >= 0:
150         x[0] += step
151         x[1] -= step*factor
152         data.write('G1_X' + str(x[0]) + 'Y' + str(x[1]) +
153                    'Z' + str(x[2]) + 'F1\n')
154         x[0] -= step_back
155         x[1] += step_back*factor
156         data.write('G1_X' + str(x[0]) + 'Y' + str(x[1]) +
157                    'Z' + str(x[2]) + 'F1\n')
158     elif length_x >= 0 and length_y <= 0:
159         x[0] -= step
160         x[1] += step*factor
161         data.write('G1_X' + str(x[0]) + 'Y' + str(x[1]) +
162                    'Z' + str(x[2]) + 'F1\n')
163         x[0] += step_back
164         x[1] -= step_back*factor
165         data.write('G1_X' + str(x[0]) + 'Y' + str(x[1]) +
166                    'Z' + str(x[2]) + 'F1\n')
167     plot_x.append([x[0], x[1]])
168 else:
169     factor = 0
170     length_y /= (step - step_back)
171     for i in range(0, int(abs(length_y))):
172         for k in range(0, 1):
173             if length_x <= 0 and length_y <= 0:
174                 x[0] += step*factor
175                 x[1] += step
176                 data.write('G1_X' + str(x[0]) + 'Y' + str(x[1]) +
177                            'Z' + str(x[2]) + 'F1\n')
178                 x[0] -= step_back*factor
179                 x[1] -= step_back
180                 data.write('G1_X' + str(x[0]) + 'Y' + str(x[1]) +
181                            'Z' + str(x[2]) + 'F1\n')
182             elif length_x >= 0 and length_y >= 0:
183                 x[0] -= step*factor
184                 x[1] -= step
185                 data.write('G1_X' + str(x[0]) + 'Y' + str(x[1]) +
186                            'Z' + str(x[2]) + 'F1\n')
187                 x[0] += step_back*factor
188                 x[1] += step_back
189                 data.write('G1_X' + str(x[0]) + 'Y' + str(x[1]) +
190                            'Z' + str(x[2]) + 'F1\n')
191             elif length_x <= 0 and length_y >= 0:
192                 x[0] += step*factor
193                 x[1] -= step_back
194                 data.write('G1_X' + str(x[0]) + 'Y' + str(x[1]) +
195                            'Z' + str(x[2]) + 'F1\n')
196                 x[0] -= step_back*factor
197                 x[1] += step_back
198                 data.write('G1_X' + str(x[0]) + 'Y' + str(x[1]) +
199                            'Z' + str(x[2]) + 'F1\n')
200             elif length_x >= 0 and length_y <= 0:
201                 x[0] -= step*factor
202                 x[1] += step
203                 data.write('G1_X' + str(x[0]) + 'Y' + str(x[1]) +
204                            'Z' + str(x[2]) + 'F1\n')
205                 x[0] += step_back*factor
206                 x[1] -= step_back
207                 data.write('G1_X' + str(x[0]) + 'Y' + str(x[1]) +

```

```

208         '\uZ' + str(x[2]) + '\uF1\n')
209     plot_x.append([x[0], x[1]])
210     plot_x.append('--')
211     data.write('M108\uS0\n') # Extruder speed [RPM]
212     return x[0], x[1], x[2]
213     #####
214
215 plot_x = []
216 # Open File for write
217 try:
218     data = open(file_out, 'w')
219 except IOError:
220     print file_out, "is\unot\uwritable!"
221     sys.exit(1)
222
223
224 data.write('G90\n') # Absolute Positioning
225 data.write('G21\n') # Set units to mm
226
227 data.write('M104\uS0\n') # Extruder Temperature
228 data.write('G1\uX' + str(0) + '\uY' + str(0) + '\uZ' + str(20) + '\uF100\n')
229
230 # Reference
231 #####
232 x,y,z = 5, 5, 0.4 # Start point
233 data.write('G1\uX' + str(x) + '\uY' + str(y) + '\uZ' + str(20) + '\uF100\n')
234 x,y,z = Line(x, y, z, 15, y)
235 x,y,z = 10, 0, 0.4
236 x,y,z = Line(x, y, z, x, 10)
237
238 x,y,z = 40, 173, 0.4
239 x,y,z = Line(x, y, z, 50, y)
240 x,y,z = 45, 168, 0.4
241 x,y,z = Line(x, y, z, x, 178)
242 data.write('G1\uX' + str(x) + '\uY' + str(y) + '\uZ' + str(20) + '\uF100\n')
243
244 # Print a rectangular coil
245 #####
246 front = False
247
248 if front:
249     x,y,z = 36, 10, 0.4 # Start point
250     x,y,z = Circle(x, y, z, 0.3)
251     x,y,z = Line(x, y, z, x, 45)
252     x,y,z = Square(x, y, z, 23, 4, 1)
253
254
255 else:
256     x,y,z = 33, 49, 0.4 # Start point
257     x,y,z = Line(x, y, z, x, 45)
258     x,y,z = Line(x, y, z, 36, y)
259     x,y,z = Line(x, y, z, x, 10)
260     x,y,z = Circle(x, y, z, 0.3)
261
262 #####
263 data.write('G1\uX' + str(x) + '\uY' + str(y) +
264           '\uZ' + str(20) + '\uF100\n')
265 data.write('G1\uX' + str(150) + '\uY' + str(150) +
266           '\uZ' + str(50) + '\uF1000\n')
267 data.write('M18\n') # Disable all stepper motors
268 data.write('M107\n') # Turns fan off
269 data.close()
270
271 # Plot the pattern
272 if plot:
273     fig = plt.figure()
274     ax = fig.add_subplot(111)
275     k = 0
276     for j in range(plot_x.count('--')):
277         plot_xx = []

```

```
278     plot_yy = []
279     for i in range(k, len(plot_x)):
280         if plot_x[i] != '--':
281             plot_xx.append(plot_x[i][0]+58)
282             plot_yy.append(plot_x[i][1])
283         else:
284             k = i+1
285             break
286     ax.plot(plot_xx, plot_yy, label=str(j+1), color='black')
287
288     plt.title('Printing Model on the Fabbster 3D-Printer')
289     plt.xlabel('X-Axis [mm]')
290     plt.ylabel('Y-Axis [mm]')
291     plt.xlim(0, 230)
292     plt.ylim(0, 210)
293     plt.show()
```

List of Figures

1.1. Former concept of thin film sensors for analysis of three-phase transformer cores.	1
1.2. Normal flux density B_z as detected by a flat frame coil and a 50 μm thick wire coil.	3
1.3. Principle of the Hall sensor.	4
1.4. Principle of the search coil.	5
1.5. Principle of a modern low-cost personal 3D printer.	7
1.6. Toolchain of a 3D printer.	7
1.7. Diagram of the piezo drop-on-demand ink-jet printing system.	9
1.8. Schematic of a piston dispensing system.	10
2.1. Principle of the print efficiency.	14
2.2. Four-point probe measurement on a printed silver trace.	15
2.3. Components of carbomorph.	16
2.4. Resistivity measurements with carbomorph at different wt% of Black Pearls 2000.	17
2.5. Microscope image of the conductive silver ink Silver Print.	18
2.6. Test pattern to calculate the resistivity ρ of the conductive silver ink.	18
2.7. Resistivity ρ of the Circuit Work CW2200 ink as a function of the curing temperature T	20
2.8. Key constituents in the initial solution, ink, and printed futures.	20
2.9. Resistivity ρ of the self-made reactive silver ink as a function of the curing temperature T	21
2.10. Property of the Kapton foil under plasma treatment at different resisting times.	22
2.11. Resistivity ρ of the DuPont 5028 ink as a function of the curing temperature T	23
2.12. Comparison of the resistivity ρ of all tested conductive materials.	24
3.1. FabbsterG 3D printer.	26
3.2. Example of a printed vase, printed with the FabbsterG 3D printer and ABS filaments.	26
3.3. Modifications of FabbsterG 3D printer to manufacture thin-film magnetic sensors.	27
3.4. Measurement of the extruder motor signal.	29
3.5. Self-made hardware board for the 2D print setup.	30
3.6. Principle of the speed control for the 2D print setup.	32

3.7. Example of the Python script to create G-code commands for FabbsterG 3D printer.	33
3.8. Extruder velocity v as a function of the step size Δs	34
3.9. Volume flow \dot{V} as a function of the time t between two steps.	35
3.10. Parameter study of the printer speed v	36
3.11. Thickness h of the printed pattern as a function of the printer speed v	36
3.12. Comparison of the thickness h at different inks and substrates.	37
3.13. FEM simulation of the pressure drop Δp	39
3.14. Volume flow \dot{V} as a function of the dispensing height Δz	40
3.15. Mechanical structure simulations of the self-made aluminum bracket.	41
4.1. Test of a combined 3D/2D printer printed structure.	43
4.2. Schematic diagram of the laser measurement setup to measure the layer thickness h	44
4.3. Topographical map of the printed structure.	45
4.4. Schematic diagram of the calibration setup.	48
4.5. Manufacturing process of the first version of the rectangular square coil sensor. a) First step of the manufacturing process. b) Finished sensor.	49
4.6. Dimensions of version 2 of the magnetic sensor.	51
4.7. Picture of the manufactured sensor.	51
5.1. Picture of the three-phase transformer core.	54
5.2. Detailed wiring diagram of the experimental setup for B_z measurement.	55
5.3. Sensor position P for the measurements of B_z inside the transformer core.	56
5.4. Typical results for the measuring point P	57
5.5. Amplitude of the magnetic flux density B_z , measured with different sensors.	58
5.6. Amplitude of the magnetic flux density B_z at different inter-laminar air-gap g	59
5.7. Relative deviation f as a function of the nominal magnetization \hat{B}	60
A.1. Drawing of the holder for the cartridge and linear stepper motor.	64
A.2. Assembly drawing of the piston dosing system.	65
A.3. Wiring diagram of the controll board for the 2D print setup.	66

List of Tables

1.1. Comparison of 2D dispensing techniques.	8
2.1. Comparison of the different measurements methods of resistivity ϱ	19
3.1. Investigated G-code commands for the FabbsterG 3D printer. .	32
4.1. Relation between current I and the magnetic flux density B for the calibration.	48
4.2. Summary of the characteristics of the sensor version 1.	50
4.3. Summary of the characteristics of the sensor version 2.	51

List of Listings

A.1. Arduino UNU program to controll the linear stepper motor. . .	67
A.2. Python script to create G-code commands for the FabbsterG 3D printer	71

Bibliography

- [1] H. Pfützner. Magnetic foil sensor for interior transformer core analysis. *FFG Application*, 2014.
- [2] H. Pfützner and E. Mulasalihovic. Thin-film technique for interior magnetic analysis of laminated machine cores. *Prez.Elektrot.*, 85:39–42, 2009.
- [3] W. T. Hicks, T. R. Allington, and V. Johnson. Membrane touch switches: Thick-film materials systems and processing options. *IEEE Comp.Pack.Manufac.Tech.*, 3(4):518–524, 1980.
- [4] B.S. Cook. Inkjet printing of novel wideband and high gain antennas on low-cost paper substrate. *IEEE Trans.Anten.Prop.*, 60(9):4148 – 4156, 2012.
- [5] F.C. Krebs, S.A. Gevorgyan, and J. Alstrup. A roll-to-roll process to flexible polymer solar cells: model studies, manufacture and operational stability studies. *J. Mater. Chem.*, 19(30):5442–5451, 2009.
- [6] H. Sirringhaus, T. Kawase, R. H. Friend, T. Shimoda, M. Inbasekaran, W. Wu, and E. P. Woo. High-resolution inkjet printing of all-polymer transistor circuits. *Science*, 15(290):2123–2126, 2000.
- [7] K. Sun, T.S. Wei, B.Y. Ahn, J.Y. Seo, S.J. Dillon, and J.A. Lewis. 3d printing of interdigitated li-ion microbattery architectures. *Adv.Mat.*, 25(33):4539–4543, 2013.
- [8] B. Li, S. Santhanam, L. Schultz, M. Jeffries-EL, M.C. Iovu, G. Sauvé, J. Cooper, R. Zhang, J.C. Revelli, A.G. Kusne, J.L. Snyder, T. Kowalewski, L.E. Weiss, R.D. McCullough, G.K. Fedder, and D.N. Lambeth. Inkjet printed chemical sensor array based on polythiophene conductive polymers. *Sens.Act.B*, 123(2):651 – 660, 2007.
- [9] M.J. McDermott. Transformer can contribute to global warming goals. *Copper & Global Warming*, 2002.
- [10] G. Shilyashki, H. Pfützner, P. Hamberger, M. Aigner, F. Hofbauer, I. Matkovic, and A. Kenov. The impact of off-plane flux on losses and magnetostriction of transformer core steel. *IEEE Trans.Magn.*, accepted, 2014.
- [11] H. Yamaguchi, M. Ishida, and H. Pfützner. 3d magnetic flux measurement in joint region of a model core stacked with grain-oriented electrical steel. *IEEJ Trans.Ind.Appl.*, 130(9):1087–1093, 2010.

- [12] R. Boll and K.J. Overshott. *Sensors, A Comprehensive Survey, Magnetic Sensors*. John Wiley & Sons, Weinheim, 2008.
- [13] X.G. Yao, A.J. Moses, and F. Anayi. Normal flux distribution in a tree-phase transformer core unter sinusoidal an pwm excitation. *IEEE Trans.Magn.*, 43(6):2660–2662, 2007.
- [14] H. Pfützner, C. Bengtsson, T. Booth, F. Löffler, and K. Gramm. Three-dimensional flux distribution in transformer cors as a function of package design. *IEEE Trans.Magn.*, 30(5):2713–2727, 1994.
- [15] A. Basak and D. M. Rowe. Magnetic flux and loss measurements using thin film sensors. *IEEE Trans.Magn.*, 31(6):3170–3172, 1995.
- [16] A. Ilo, H. Pfützner, and Ch. Eisenmenger-Sittner. Sputtered search coils for flux distribution analysis in laminated magnetic cores. *J Phys IV France*, 8:72–75, 1998.
- [17] P. Fastermann. *3D-Druck/Rapid Prototyping: Eine Zukunftstechnologie - kompakt erklärt*. Springer, Berlin Heidelberg, 2012.
- [18] E. Brian. *Practical 3D Printers - The Science and Art of 3D Printing*. Apress, New York, 2012.
- [19] K.K.B. Hon, L. Li, and I.M. Hutchings. Direct writing technology—advances and developments. *{CIRP} Annals - Man.Tech.*, 57(2): 601 – 620, 2008.
- [20] S. Fuller, E. Wilhelm, and J. Jacobson. Ink-jet printed nanoparticle microelectromechanical system. *J.Microelectrom.S.*, 11(1):54–60, 2002.
- [21] C. Ibeh. *Thermoplastic Materials - Properties, Manufacturing Methods, and Applications*. Taylor & Francis, Justus-Liebig-Universität Gießen, 2011.
- [22] J. Perelarer, U.S. Schubert, and F. Jena. *Radio Frequency Identification Fundamentals and Applications, Design Methods and Solutions*. InTech, Rijeka, 2010.
- [23] A. Breyfogle and K. Varanian. Capability assessment of combining 3d printing (fdm) and printed electronics (aerosol jet) to produce fully printed functionalized devices. *Rap.Prot.*, 2013.
- [24] D. Espalin, D. Muse, E. MacDonald, and R. Wicker. 3d printing multifunctionality: structures with electronics. *J.Adv.Manu.Tech.*, 72(5-8): 963–978, 2014.
- [25] *Fabbster G Manual*. Sintermask GmbH.
- [26] G. Cummins and M. Desmulliez. Inkjet printing of conductive materials: a review. *Circuit World*, 38(4):193–213, 2012.

- [27] D.R. Lide et al., editors. *CRC Handbook of Chemistry and Physics*. CRC Press, Boca Raton, 2007.
- [28] S.J. Leigh, R.J. Bradley, C.P. Purcell, D.R. Billson, and D.A. Hutchins. A simple, low-cost conductive composite material for 3d printing of electronic sensors. *PLoS ONE*, 7(11):e49365, 2012.
- [29] J.P. Reboul and G. Moussalli. About some d-c conduction processes in carbon black filled polymers. *J.Poly.Mat.*, 5(1-2):133–146, 1976.
- [30] S.B. Walker and J.A. Lewis. Reactive silver inks for patterning high-conductivity features at mild temperatures. *J.Chem.Soc.*, 134(3):1419–1421, 2012.
- [31] D. Hegemann, H. Brunner, and C. Oehr. Plasma treatment of polymers for surface and adhesion improvement. *Nucl.Instrum.Meth.*, 208(0):281 – 286, 2003.
- [32] S. Luo and C.P.Wong. Effect of uv/ozone treatment on surface tension and adhesion in electronic packaging. *IEEE Trans.Comp.Pack.Tech.*, 24(1):43–49, 2001.
- [33] *Arduino UNO Manual*. Arduino, 3 edition.
- [34] *A4988 Microstepping Driver Manual*. Allegro MicroSystems Inc., 1 edition.
- [35] T. R. Kramer, F. M. Proctor, and E. R. Messina. The nist rs274ngc interpreter - version 3. *The National Institute of Standards and Technology*, 2000.
- [36] R. Hackenschmidt and B.A.F. Rieg. *Finite Elemente Analyse für Ingenieure*. Hanser Fachbuchverlag, München, 2012.
- [37] R. Schwarze. *CFD-Modellierung: Grundlagen und Anwendungen bei Strömungsprozessen*. Springer, Berlin Heidelberg, 2012.
- [38] *Introduction to Comsol Multiphysics*, 4.4 edition, 2013.
- [39] W. Demtröder. *Experimentalphysik 1: Mechanik und Wärme*. Springer, Berlin Heidelberg, 2012.
- [40] G. Krismanic, E. Leiss, S. Barsoum, and H. Pfützner. Automatic scanning system for the determination of local loss distributions in magnetic cores. *J.Mag.Mag.Mat.*, 254–255(0):60 – 63, 2003.
- [41] D. Gross, W. Hauger, J. Schröder, and W. Wall. *Technische Mechanik: Band 1: Statik*. Springer, Berlin Heidelberg, 2008.
- [42] N. Chukwuchekwa, A. Moses, and P. Anderson. Investigation of the effect of strip thickness and grain size on ac magnetic barkhausen noise of grain-oriented electrical steel. *Prez.Elektrot.*, 88(5a):18–21, 2012.

- [43] H. Pfützner. 3-dimensional loss distribution in transformer cores. *BRIDGE, FFG-Siemens Application*, 2012.
- [44] A.J. Moses. *Handbook of Magnetism and Advanced Magnetic Materials*. John Wiley & Sons, Weinheim, 2008.
- [45] G.E. Fish. Soft magnetic materials. *IEEE Proc.*, 78(6):947–972, 1990.
- [46] H. Pfützner, G. Shilyashki, P. Hamberger, M. Aigner, F. Hofbauer, M. Palkovits, G. Trenner, E. Gerstbauer, I. Matkovic, and V. Galabov. Automatic 3-d building factor analyses of a grain-oriented model transformer core. *IEEE Trans.Magn.*, 50(4):1–4, 2014.
- [47] Din 541: Bestimmung der magnetischen eigenschaften von elektroblech im 50 cm epsteinrahmen. *DIN - German institute for standardization*, 1960.
- [48] E. Mulasalihovic. *Simulation von Effekten geomagnetisch induzierter Ströme (GICs) auf Transformatorkerne*. PhD thesis, Technische Universität Wien, 2011.